A CHEMOPOROELASTIC MODEL

FOR SHALE GAS FORMATION WITH MULTI-SCALE PORE STRUCTURE: QUANTIFICATION OF PERMEABILITY ALTERATION DUE TO CLAY SWELLING AND TENSILE STRESSES

A Dissertation

by

VENA FLORENTINA EVELINE

Submitted to the Office of Graduate and Professional Studies of
Texas A&M University
in partial fulfillment of the requirements for the degree of

DOCTOR OF PHILOSOPHY

Chair of Committee,	I. Yucel Akkutlu
Co-Chair of Committee,	George J. Moridis
Committee Members,	Walter B. Ayers
	Yalchin Efendiev
Head of Department,	A. Daniel Hill

August 2017

Major Subject: Petroleum Engineering

ABSTRACT

The main focus of this work was to study formation damage during shut-in time and production following hydraulic fracturing a gas shale formation. More specifically, this work investigated numerically the intricate effects of water imbibition, osmosis and clay swelling on shale permeability under stress. For this purpose a new conceptual petrophysical model was proposed for the shale matrix containing slit pores (microcracks), clay pores and organic pores, and a new geo-mechanically coupled reservoir flow simulator was developed, which dynamically accounts for the impact of these mechanisms on the permeability.

Simulation case studies were conducted to investigate the nature of the formation damage. It is observed that an altered permeability zone, rather a 'fracture skin', is developed during the shut-in following the fracturing. The permeability changes due to osmosis-related clay swelling and stress. The magnitude of permeability alterations is controlled mainly by the salt concentration difference between the injected fracturing fluid and the clay-bound water, the clay-membrane efficiency, the cation exchange capacity (CEC), the salt type, the clay porosity, the overburden stress and the duration of the shut-in time.

Clay pore pressure buildup due to osmosis increases the local stresses in the altered zone during the shut-in time and the production. However, it is predicted that the increased stress is insufficient to induce new microcracks and that significantly higher pore pressure is required to reach the tensile failure limit of the formation. The overpressure required for the tensile failure is dependent on the depth and the tensile strength of the formation, and on the geometry of the pores.

DEDICATION

I dedicate this book to my beloved Family.

ACKNOWLEDGEMENTS

I would like to thank my committee chair, Dr. I. Yucel Akkutlu, my committee co-chair, Dr. George J. Moridis, and my committee members, Dr. Walter B. Ayers, and Dr. Yalchin Efendiev for their guidance, support and help throughout the course of this research.

Thanks also go to my friends and colleagues in Texas A&M University for their help, support and friendships.

Gratitude also goes to PERTAMINA, the Indonesia National Oil Company, which sponsored me throughout my study at Texas A&M University.

Finally, I owe the greatest gratitude to my father and my mother for everything. To my sisters and brothers-in-law, I appreciate and cannot thank enough for their love and support.

CONTRIBUTORS AND FUNDING SOURCES

Contributors

This work was supervised by a dissertation committee consisting of Professor I. Yucel Akkutlu [advisor], Professor George J. Moridis [co-advisor], Professor Walter Ayers of the Department of Petroleum Engineering and Professor Yalchin Efendiev of the Department of Mathematics.

All work for the dissertation was completed independently by the student.

Funding Sources

Graduate study was supported by scholarship from PERTAMINA, Indonesia National Oil Company.

NOMENCLATURE

A_{nm}	Surface are between element n and m [m^2]
C_{μ}	Sorbed-gas concentration in kerogen grain volume [mol/m^3]
$C_{\mu s}$	Maximum sorbed-gas concentration in kerogen grain volume [mol/m^3]
CEC	Cation exchange capacity [meq/100g]
$D_{o,A}^{H_2O}$; $D_{o,A}^{CH_4}$; $D_{o,A}^{Salt}$	Free-diffusion coefficient of H_2O, CH_4 and salt in the aqueous-phase [m^2/s]
$D_{o,G}^{H_2O}$; $D_{o,G}^{CH_4}$	Free-diffusion coefficient of H_2O and CH_4 in the gas-phase [m^2/s]
$\mathbf{F}_A^{H_2O}$; $\mathbf{F}_{\mathrm{A}}^{\mathrm{Salt}}$; $\mathbf{F}_{\mathrm{A}}^{CH_4}$	Total mass flux of H_2O, salt and CH_4 in aqueous-phase flow [$kg/s.m^2$]
$\mathbf{F}_A^{H_2O}\big\vert_{\mathrm{adv}}$; $\mathbf{F}_G^{H_2O}\big\vert_{\mathrm{adv}}$	Advective mass flux of H_2O in aqueous- and gas-phase flow [$kg/s.m^2$]
$\mathbf{F}_A^{CH_4}\big\vert_{\mathrm{adv}}$; $\mathbf{F}_G^{CH_4}\big\vert_{\mathrm{adv}}$	Advective mass flux of CH_4 in aqueous- and gas-phase flow [$kg/s.m^2$]
$\mathbf{F}_A^{Salt}\big\vert_{\mathrm{adv}}$	Advective mass flux of salt in aqueous-phase flow [$kg/s.m^2$]
$\mathbf{F}_A^{H_2O}\big\vert_{\mathrm{dif}}$; $\mathbf{F}_G^{H_2O}\big\vert_{\mathrm{dif}}$	Diffusion mass flux of H_2O in aqueous- and gas-phase flow [$kg/s.m^2$]
$\mathbf{F}_A^{CH_4}\big\vert_{\mathrm{dif}}$; $\mathbf{F}_G^{CH_4}\big\vert_{\mathrm{dif}}$	Diffusion mass flux of CH_4 in aqueous- and gas-phase flow [$kg/s.m^2$]
$\mathbf{F}_A^{Salt}\big\vert_{\mathrm{dif}}$	Diffusion mass flux of salt in aqueous-phase flow [$kg/s.m^2$]
g	Gravitational acceleration vector [m/s^2]
k	Permeability of slit-shaped pore [m^2]
k_I	Slit-shaped pore permeability [m^2]

k_m	Permeability of porous medium acting as semi-permeable membrane [m^2]
k_0	Slit-shaped pore permeability at zero effective stress [m^2]
$k_{rA};\ k_{rG}$	Relative permeability of aqueous- and gas-phase [-]
ℓ_{IC}	Shape factor [$1/m^2$]
m	Coefficient in Gangi's permeability model [-]
M^{κ}	Mass accumulation of component κ
M_s	Salt molar mass [kg/mol]
M_{CH_4}	Molecular weight of CH_4 [kg/mol]
P	Slit-shaped pore pressure [Psi; Pa]
$P_A;\ P_G$	Aqueous- and gas phase pressure [Psi; Pa]
$P_{A,I}$	Inorganic slit-shaped pore pressure [Psi; Pa]
$P_{A,C}$	Clay pore pressure [Psi; Pa]
P_{conf}	Confining pressure [Psi; Pa]
P_1	Effective stress when the slit-shaped pores are close completely [Psi; Pa]
P_L	Langmuir pressure [Psi; Pa]
q^K	Source/sink of component K [$kg/s.m^3$]
$q^{H_2O}; q^{Salt};\ q^{CH_4}$	Source/sink of component H_2O, salt and CH_4 [$kg/s.m^3$]
$\mathbf{q}_A$	Aqueous-phase velocity [m/s]
R	Gas constant, equal to 8.3145 [J/mol.K]
$R_n^{\kappa,\mathrm{k+1}}$	Residuals of component K at time k+1, in element n
$S_A; S_G$	Aqueous- and gas-phase saturation
t	Time
T	Temperature [^oC; K]
$\bar{V}$	Partial molar volume of solvent [liters per mol]
x^s	Salt mass fraction

$x_A^{H_2O}; x_A^{Salt};\ x_A^{CH_4}$	Mass fraction of component H_2O, salt and CH_4 in aqueous-phase flow
$x_G^{H_2O}; x_G^{Salt};\ x_G^{CH_4}$	Mass fraction of component H_2O, salt and CH_4 in gas-phase flow
$x_{A,I}^{Salt}; x_{A,I}^{H_2O}$	Salt and H_2O mass fraction in inorganic pore
$x_{A,C}^{Salt}; x_{A,C}^{H_2O}$	Salt and H_2O mass fraction in clay pore
V_n	Volume of element n [m^2]
V_{sL}	Langmuir volume, sorbed-gas volume per total grain mass [m^3/kg]
$w_{A,IC}^{H_2O};\ w_{A,IC}^{CH_4};\ w_{A,IC}^{Salt}$	Mass exchange of H_2O, CH_4 and salt between slit-shaped and clay pore mass [$kg.m^{-3}.s^{-1}$]

Symbols

α	Biot coefficient
β	Phase
β_t	Linear thermal expansion
E	Young's modulus [Pa]
ε_{ks}	Total organic content, organic grain volume per total grain volume [-]
κ	Component
μ_A and μ_G	Viscosity of aqueous- and gas-phase [Pa.s]
π	Osmotic pressure [Pa]
$\rho_A;\ \rho_G$	Aqueous- and gas-phase density [kg/m^3]
ρ_f	Fluid density [kg/m^3]
ρ_{grain}	Grain density [kg/m^3]
$\rho_{sc,gas}$	Gas density in standard condition [kg/m^3]
$\mathcal{R}$	Clay-membrane efficiency [-]
$\bar{\sigma}$	Mean stress [Pa; psi]

σ_H	Horizontal stress [Pa; psi]
σ_{OB}	Overburden stress [Pa; psi]
$\tau_A;\ \tau_G$	Tortuosity of the aqueous- and gas-phase [-]
v	Poisson ratio
θ	Dissociation coefficient [-]
ϕ	Porosity of porous medium [fraction]
ϕ_C	Clay porosity [fraction]
ϕ_I	Inorganic slit-shaped pore porosity [fraction]
ϕ_k	Organic (kerogen) porosity [fraction]
χ	Effective stress coefficient [-]

TABLE OF CONTENTS

Page

LIST OF FIGURES

Page

LIST OF TABLES

Page

1. INTRODUCTION

1.1. Background

It is widely known that hydraulic fracturing is key in unlocking the potential of shale oil/gas formations (Curtis, 2002; Warpinski et al., 2009; Mayerhofer et al., 2010). The shale formations have inherently low matrix permeability that require the hydraulic fracturing stimulation to access the natural fracture system and to create new fractures (Curtis, 2002).

Hydraulic fractures can be classified as simple fracture, complex fracture, complex fracture with fissure opening or complex fracture network (Fig. 1) (Fisher et al., 2005; Warpinski et al., 2009). The simple hydraulic fracture is a single bi-wing planar crack with wellbore at the center of the two wings (Fisher et al., 2005). During hydraulic fracturing stimulation, the simple fracture geometry, planar fracture, can be created when there is high contrast between minimum and maximum horizontal stresses in the formation; on the other hand, the complex fracture geometry can be generated when the stress contrast is relatively low (Fig. 2) (Fan et al., 2010).

Hydraulic fracturing in shale formations may include the full spectrum from the simple fracture to the complex fracture network (Warpinski et al., 2009). In some Barnett shale (Fisher et al., 2005; Warpinski et al., 2009) and Haynesville shale (Fan et al., 2010) locations, for instance, the hydraulic fracturing stimulation had resulted in the complex fracture network type. This fracture type is due to several reasons including the presence of natural fractures that may be activated (i.e., re-opened) during the fracturing in some Barnett shale wells (Fisher et al., 2005; Warpinski et al., 2009). Other factors such as rock fabric, preexisting factures, and layering may also cause more complex fracture geometry during the stimulation (Fan et al., 2010).

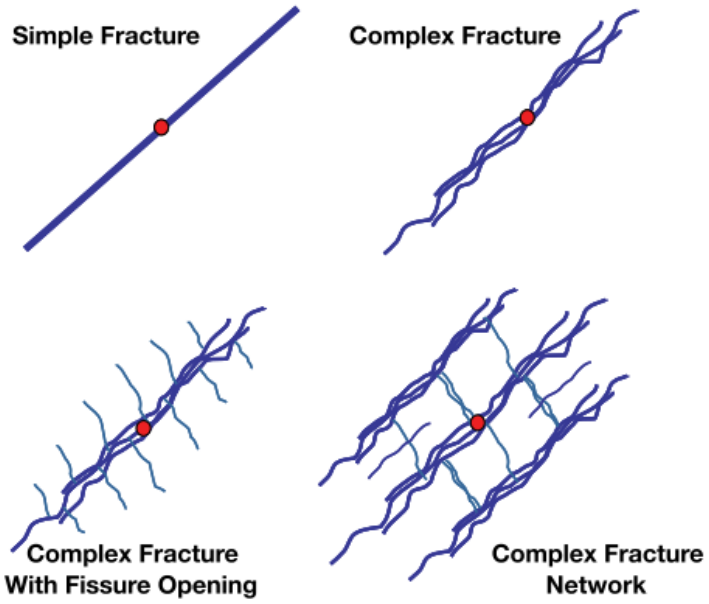

Fig. 1 - Schematic showing levels of fracture complexity. Reprinted from Warpinski et al. (2009).

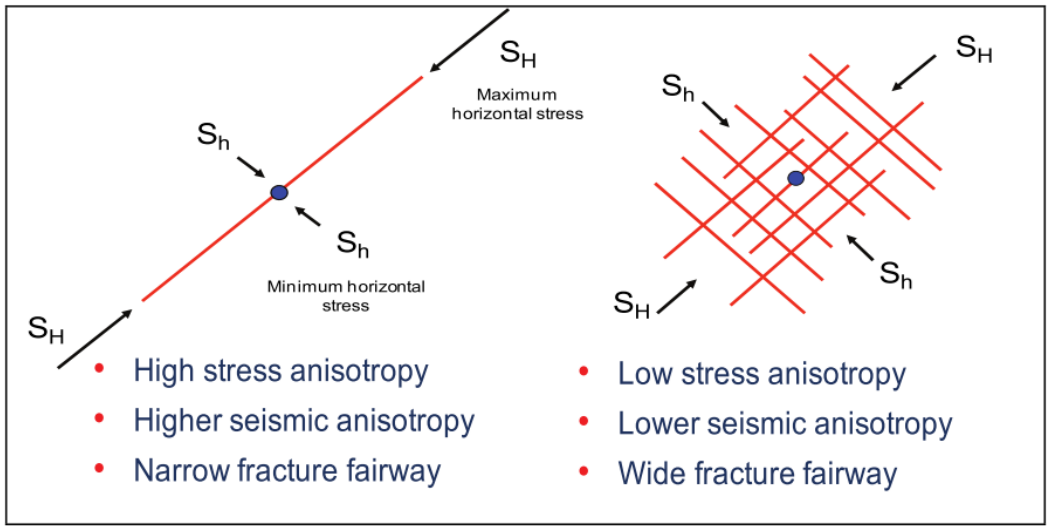

Fig. 2 - Planar and complex fracture geometry from stress contrast. Reprinted from Fan et al. (2010).

Combination of hydraulic fractures and natural fractures could control recoveries from certain formations (Fisher et al., 2005). The common hydraulic fracturing strategy practiced in shale reservoirs is to create a fracture network with maximum possible fracture density and sufficient fracture conductivity. This ensures maximum well production performance (Warpinski et al., 2009; Fan et al., 2010; Mayerhofer et al., 2010; Palisch et al., 2010). Slickwater fracturing is the most utilized technique to stimulate tight gas and shale reservoirs because it may provide a more complex fracture geometry (Palisch et al., 2010). Although the injection includes chemical additives, such as salt, gel, scale inhibitor, friction reducer, breaker, pH adjuster, cross-linker, corrosion inhibitor, surfactant, biocide, etc., the injected volume contains mainly (99%) water (Arthur et al., 2008). A large volume of slickwater is pumped into the well at high rates for fracture initiation and propagation (Palisch et al., 2010). After multi-stage hydraulic fracturing operations, fractured zones may be shut-in for several days.

Field experience has shown that not all of the injected water flows back, when the production begins. For example, recovery of the water for the Haynesville shale wells varies from 10-30% of the injected volume during the first few months of production (Fan et al., 2010). In general, less than half of the treatment water is recovered, and in many cases the recovery of the injected fluid is less than 30% (Pagels et al., 2012; Engelder et al., 2014). On average, when the recovery of the treatment water is 20%; about 4 million gallons of water are left in the formation (Pagels et al., 2012).

The fate of the fracturing water and the fluid loss mechanisms have previously been studied by several authors (Fan et al., 2010; Ehlig-Economides and Economides, 2011; Pagels et al., 2012; Bertoncello et al., 2014; Engelder et al., 2014; Wang and Leung, 2016). There are three possible mechanisms that can cause the trapping of the injected water: the first mechanism is due to the loss of connectivity of some fracture network, as fractures perpendicular to the maximum stress are closed when the fluid pressure in the fracture is lowered at the end of the fracturing operation; the second is the trapping of water under

the influence of capillary forces in fractures; and the third is that water is imbibed into and retained within shale matrix, due to large capillary pressure in this tight lithology (Pagels et al., 2012). Fan et al. (2010) suggested that the fracture complexity around each perforation cluster may affect recovery of the fracturing water. In low-stress contrast settings (Fig. 2), the complex fracture geometry is commonly created around each perforation cluster which include a region of primary fractures filled with both proppant and the stimulation water, and a region of secondary fractures filled with the stimulation water only (Fan et al., 2010). During flow back and production periods, mainly the water within the region of primary fractures is recovered and the water in the secondary fractures region may never be returned (Fan et al., 2010). In this complex fracture geometry, the more fractures are created, the more water may be trapped in the subsurface. In high-stress contrast setting (Fig. 2), the planar fracture may consist only of the primary fracture region where fractures filled with both proppant and water are long, narrow and high-conductivity (Fan et al., 2010). In this planar fracture type, most water can be recovered (Fan et al., 2010).

Shale-water interactions may occur due to extended shut-in (or soaking) times. These interactions may lead to significant formation damage. Permeability reduction in shale samples in contact with water has previously been shown through laboratory experiments (Yan et al., 2015; Chakraborty et al., 2017). Clay swelling effect, in particular, reduced and permanently damaged the absolute permeability of the shale samples, even after water evaporation. Clay swelling may dominate the reduction of permeability over the water-blocking effect (Yan et al., 2015; Chakraborty et al., 2017). Previous experiments involving shale-water interactions showed permeability impairment when shale is brought in contact with water (Chenevert, 1970; Bostrom et al., 2014). On the other hand, shale-water interactions may increase internal hydration-related stress in the formation (Chenevert, 1970), and may cause compressive strength reduction or water weakening of the shale formation (Chenevert, 1970) and spalling or vertical fracturing (Chenevert, 1970; Chenevert and Sharma, 1993). Strong water absorption by the shale samples could also

induce micro-fractures that may improve the formation permeability (Dehghanpour et al., 2013). Further research is needed to understand permeability alteration that may occur during shale-water interactions, including permeability damage or enhancement related to clay swelling and stress change effects.

1.1.1. Clays

To clay mineralogists, clay is a layered silicate mineral, called phyllosilicate (Asef and Farrokhrouz, 2013). Most clays have a mica-type structure, with their flakes composed of stacked crystal platelets (Darley and Gray, 1988). A single platelet is called a unit layer. The basic silicate structure unit consists of silica tetrahedrons and alumina octahedrons. A tetrahedron is a silica cation that is surrounded by four oxygen anions. A combination of the tetrahedrons with covalent bonding of oxygen atoms makes a tetrahedral sheet (Fig. 3). An octahedron is an aluminum or magnesium ion surrounded by six oxygen ions, and a combination of octahedrons will form octahedral sheet (Fig. 4). Tetrahedrons and octahedrons are combined in different proportions (1:1 or 2:1) to form sheet structures.

Clay mineral crystals carry a charge arising from substitutions of certain atoms in their structure for other atoms of a different valence. This generates a negative potential at the

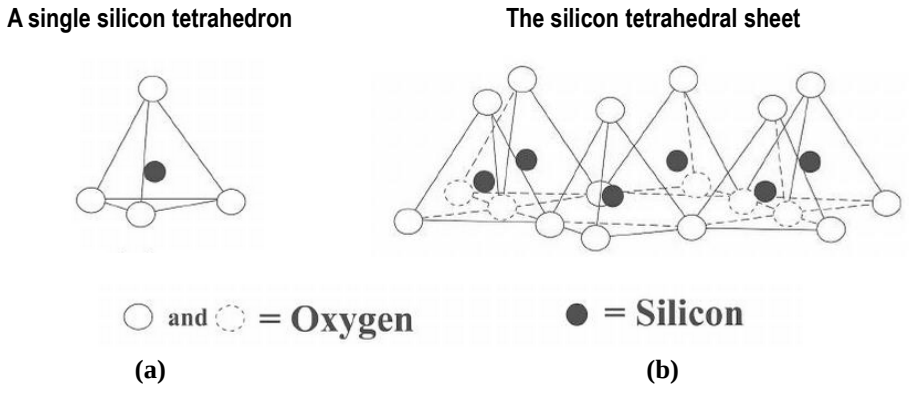

Fig. 3 - (a) A silicon tetrahedron is a silica ion surrounded by four oxygen ions; (b) The tetrahedrons are combined to form a silicon tetrahedral sheet. Reprinted from Asef and Farrokhrouz, (2013).

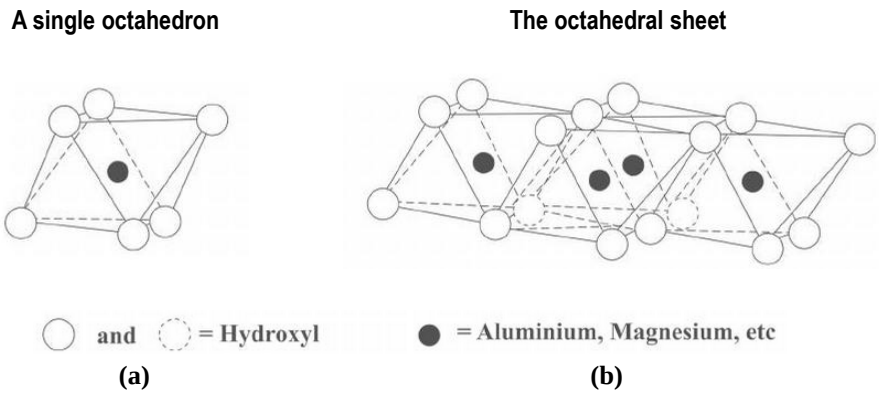

Fig. 4 - (a) An octahedron is an aluminum or magnesium ion surrounded by six oxygen ions; (b) The octahedrons are combined to form an octahedral sheet. Reprinted from Asef and Farrokhrouz, (2013).

crystal surface which is compensated by the adsorption of cation on the crystal surface. When water is present, the adsorbed cations can exchange with cations in the water. The grouping and subgroupings of clay minerals are due to the substitutions that may occur in either the tetrahedral or the octahedral sheets, and diverse species of the exchangeable cations.

Kaolinite consist of 1:1 ratio of tetrahedron and octahedron (Fig. 5). The kaolinite layers are combined by hydrogen bonding, which makes a strong, rigid lattice structure. Illite is composed of two tetrahedrons attached to one octahedron, 2:1 ratio (Fig. 6). Illite has a non-expanding lattice and has some substitution of Al for Si in the tetrahedral layer, which leads to permanent net negative charge of the illite layer. The interlayer space is filled with poorly hydrated potassium (K^+) cations. Smectites, on the other hand, have expanding lattice due to weak bonding between layers and high repulsive potentials on the surface of the layers arising from the substitutions. Montmorillonite, the best known member of the smectite group, is made of two tetrahedrons attached to one octahedron, 2:1 ratio (Fig. 7), which is similar to illite, but there is a permanent net negative charge because of substitution of Mg for Al in the octahedral layer. Higher valance cations like Ca^{2+} or Mg^{2+} are attracted into the interlayer space. Water can also exchange between the interlayers.

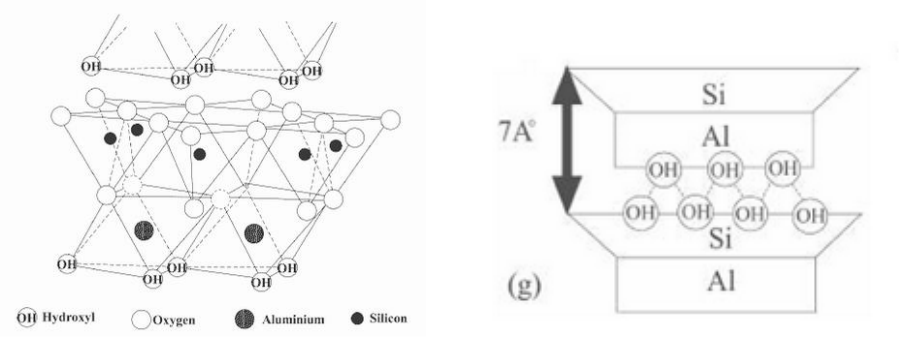

(a) **(b)**

Fig. 5 - Illustration of kaolinite: (a) molecular and crystallographic description, (b) its layer consist of 1:1 ratio of tetrahedron and octahedron and combined by hydrogen bonding. Reprinted from Asef and Farrokhrouz, (2013).

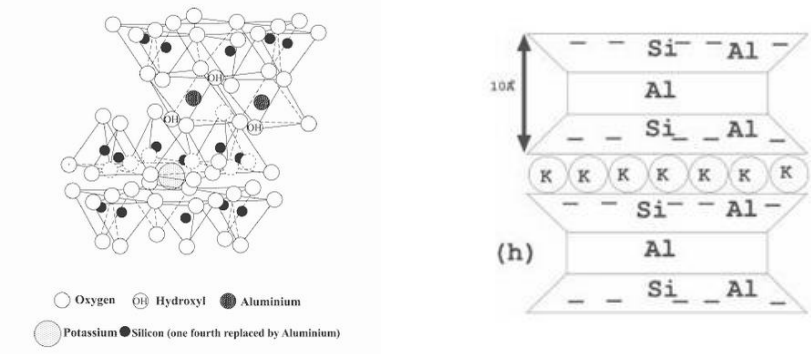

(a) **(b)**

Fig. 6 - Illustration of illite: (a) molecular and crystallographic description, (b) its layer consist of two tetrahedrons attached to one octahedron (2:1 ratio), the interlayer space is filled with poorly hydrated potassium (K^+) cations. Reprinted from Asef and Farrokhrouz, (2013).

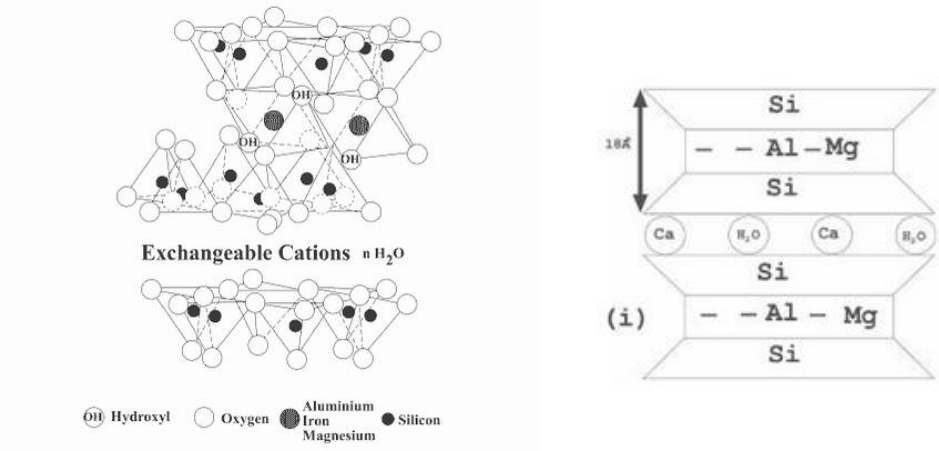

(a) **(b)**

Fig. 7 - Illustration of montmorillonite: (a) molecular and crystallographic description, (b) its layer consist of two tetrahedrons attached to one octahedron (2:1 ratio) with Ca^{2+} or Mg^{2+} or water attracts into the interlayer space. Reprinted from Asef and Farrokhrouz, (2013).

These cations and water make montmorillonite a sensitive (reactive) clay with large shrinking and swelling capacity.

Montmorillonite that has a high cation exchange capacity (CEC) swells greatly and forms viscous suspensions at low concentrations of clay, particularly when sodium is in the exchange position. On the other hand, kaolinite is relatively inert, regardless of the species of exchange cations (Darley and Gray, 1988). All classes of clay minerals absorb water, but the smectite group takes up much larger volumes than other clays do, because of their expanding lattice (Darley and Gray, 1988).

1.1.2. The Swelling of Clays

The swelling behavior of the clays is a result of the layer structure of the clay minerals and the adsorbed cations. It depends mostly on the type, quantity and surface charge of the clay minerals and the valence of the cations in the interlayer space (Madsen and Müller-Vonmoos, 1989). There are two phases of clay swelling: inner-crystalline and

osmotic swelling (Madsen and Müller-Vonmoos, 1989). Inner-crystalline swelling is caused by hydration of the exchangeable cations in the interlayer space in the presence of water (Fig. 8). This leads to a widening of the spacing between the clay layers. Osmotic swelling is driven by the difference in concentration between the ions in the clay interlayer space and the ions in the water surrounding the clay (Fig. 9).

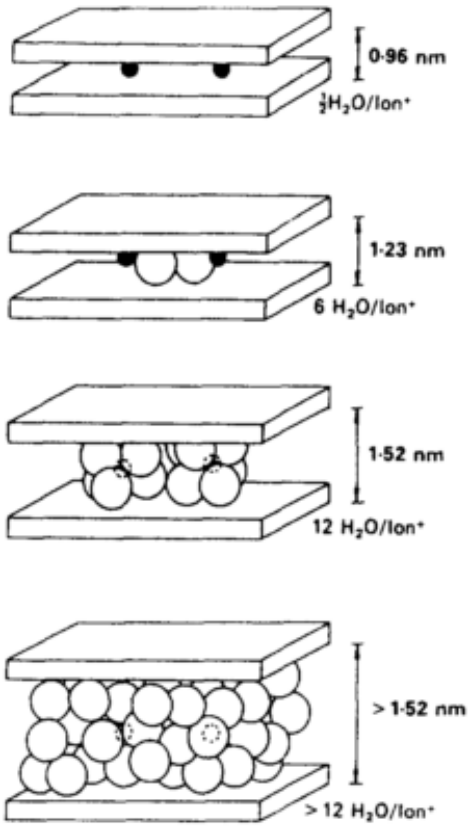

Fig. 8 - Illustration of inner-crystalline swelling of sodium montmorillonite: the interlayer space is expanding due to hydration of the exchangeable cations in the presence of water. Reprinted from Madsen and Müller-Vonmoos (1989).

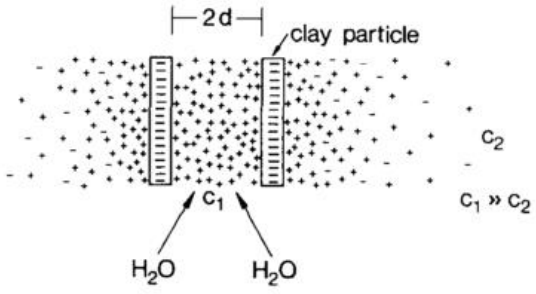

Fig. 9 - Two negatively charged clay layers with the ion concentration C_1 between the layers much higher than the ion concentration C_2 in the water surrounding the clay particle. An equilibration can only be reached by water penetrate into the clay interlayer space, since the interlayer cations are fixed electrostatically by the negative charge of the layers (osmotic swelling). Reprinted from Madsen and Müller-Vonmoos (1989).

1.2. Statement of the Problem

During extended shut-in time, after hydraulic fracturing and flow back operations, water may be left in the hydraulic fractures. The water left behind then imbibes spontaneously into the shale matrix due to very small water-wet capillaries of the shale matrix. Several mechanisms may occur during the shut-in period and cause permeability alteration.

Understanding the nature of shale permeability alteration and the mechanisms affecting them is important because one may take a measure of these mechanisms to avoid or minimize the field operations that may evoke them. In this research, I am interested in studying three formation damage mechanisms due to water-shale interactions. The first mechanism is spontaneous imbibition, which is controlled by the capillarity, causing relative permeability reduction to gas flow as water from fractures invades the shale matrix. The second mechanism is osmosis due to clay minerals in shale acting as semi-permeable membrane. Osmosis under the influence of salt concentration difference between the hydraulic-fracturing water and the clay-bound water, cause clay swelling, stress buildup and permeability reduction. The third mechanism is geomechanical and results from local stress changes that alter permeability. In this study we do not consider

other potential mechanisms that may alter the permeability, such as formation dissolution, clay dispersion, solids precipitation, chemical adsorption and adverse wettability alteration.

The main focus of this study is clay swelling and stress effects on a stress-dependent shale permeability. However, imbibition and water blocking effects cannot be avoided, because water is sucked into the shale matrix due to spontaneous imbibition during the shut-in. Hence, both the formation pressure and the osmosis-driven clay-pore pressure (also known as osmosis pressure) are affected by the capillarity. Some believe that, not only certain clays but the shale matrix may act as semi-permeable membrane as well, due to the very small pore throats and sieving effect that prevents some ions to flow into shale matrix (Rahman et al., 2005; Fakcharoenphol et al., 2014). However, in this study, we consider only clays that act as semi-permeable membrane.

Water imbibition and clay-swelling effects on permeability have been studied by previous researchers (Aksu et al., 2015; Yan et al., 2015; Chakraborty et al., 2017). However, the intricate combined effects of imbibition, osmosis and clay swelling and stress changes make it difficult to determine the impact of each on the shale permeability. Looking closely at osmotic mechanisms and clay swelling, I identify several variables that may cause permeability alteration. Geomechanics play a role in shale permeability alteration not only by the stress-dependent permeability relationships, but also, by controlling clay-membrane efficiency. In the subsurface, as stress increases with depth, the clay swelling effect on shale permeability may be quite complex.

In addition to clay-swelling effects on permeability, the phenomenon of microfracture development due to clay osmosis and high tensile stress was studied qualitatively. In laboratory experiments (Dehghanpour et al., 2013), microfracturing in shale samples was observed during shale-water interactions that caused the shale to disperse. One possible reason for this peculiar phenomenon is high tensile stress that develops due to water

imbibition into shale matrix. In this study, we want to observe whether high clay swelling pressure during shut-in period may cause tensile fracturing under stress.

1.3. Scope of the Work and Limitations

I used mathematical modeling and numerical simulation to study shale permeability alteration. I started by building a conceptual petrophysical model for gas shale systems that inherently contain multi-scale pore network, and then proceeded with the development of a system of coupled governing equations that correspond to that petrophysical model. I set up proper initial and boundary conditions the most representative of extended shut-in and production periods, and solved the equations using a numerical simulation approach. I validated the numerical model with experiments or previously published work, when possible. I ran simulation cases that may occur in the field after the hydraulic fracturing operations.

This study specifically was conducted to understand stress field, reservoir pressure propagation and permeability alteration that occur from a fracture face to deep into the shale matrix during extended shut-in time. In addition, I wanted to understand the effect of stress to the osmotic pressure in the clay pores in relation to the possibility of inducing micro-fractures due to an increase of the tensile stress with clay-pore pressure increase.

I considered the petrophysical model of shale such that the matrix contains three pore types: the organic pores; slit-shaped pores (or microcracks); and clay pores. These pores represent the major pore network of gas shale formations, as will be described in detail in Chapter 2. In this petrophysical model, I considered that the clay pores are directly connected to the slit-shaped pores only such that, although the clay pores may connect directly to the fractures, their contribution in terms of mass flux of fluid transferred to the fracture was considered negligible.

2. PETROPHYSICAL MODEL OF SHALE FORMATION WITH CLAY SWELLING EFFECT*

In this work, the effect of clays in shale, specifically clay swelling and its effect on the permeability damage was investigated using theoretical description and numerical modeling. This chapter discusses the conceptual petrophysical model of shale formations that were applied in the modeling.

2.1. Conceptual Shale Gas Petrophysical Model

Shale is the generally accepted class name for all fine-grained argillaceous rocks and sediments, including mud, clay and mudstone, that contain 50% or more of terrigenous, and generally argillaceous, clastic components less than 0.062 mm, and containing significant amounts of clay minerals and clay-size carbonate, kerogen and silica (Potter et al., 1980). Clay minerals are formed from the weathering of primary minerals such as feldspar, muscovite, and biotite.

Multi-scale, multi-porosity nature of shale matrix that was adopted in this work is an extension of another petrophysical model that was recently described by Wasaki and Akkutlu (2015). Accordingly, resource shale contains organic round pores and inorganic, slit-shaped pores, or microcracks. Round organic pores are generated by thermal maturation, during conversion of kerogen to hydrocarbon fluids, whereas slit-shaped pores are a result of cracking caused by fluid pressures in excess of hydrostatic pressure.

In this work, in addition to the organic and inorganic pores, we consider that the shale matrix holds so-called clay pores (Fig. 10). Organic-pores are pores inside kerogen. These

* Part of this chapter is reprinted with permission: "Numerical Simulation of Hydraulic Fracturing Water Effects on Shale Gas Permeability Alteration" by Eveline, V. F., Akkutlu, I Y. and Moridis, G. J. 2017. *Transport in Porous Media*, Vol. 116, 727 – 752, Copyright 2016 Springer.

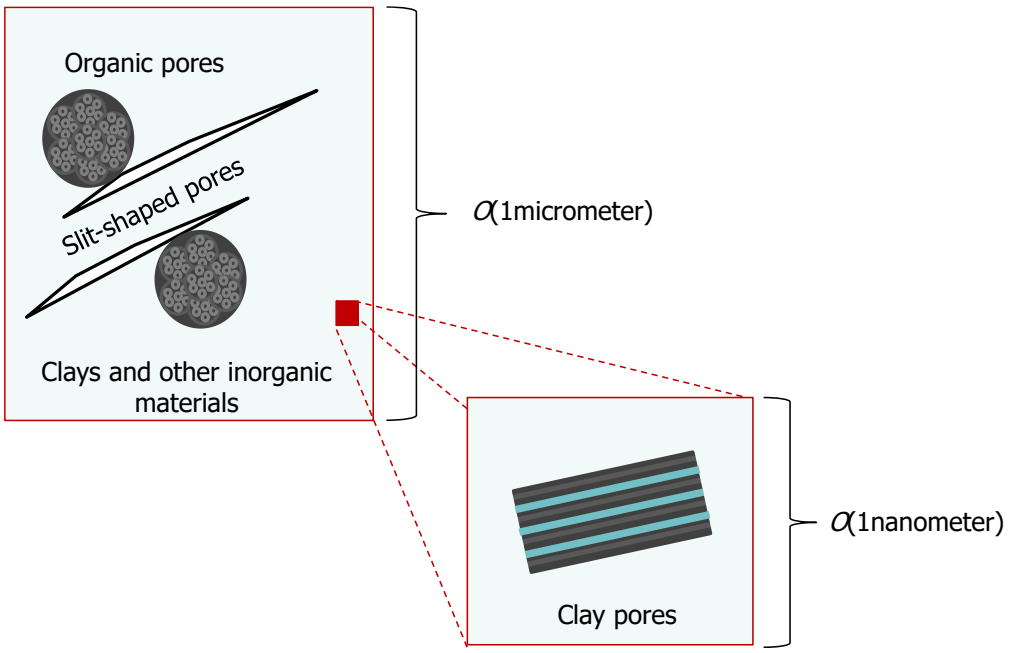

Fig. 10 - The proposed conceptual model of a shale formation containing multiscale pores: organic and, inorganic slit-shaped and clay pores.

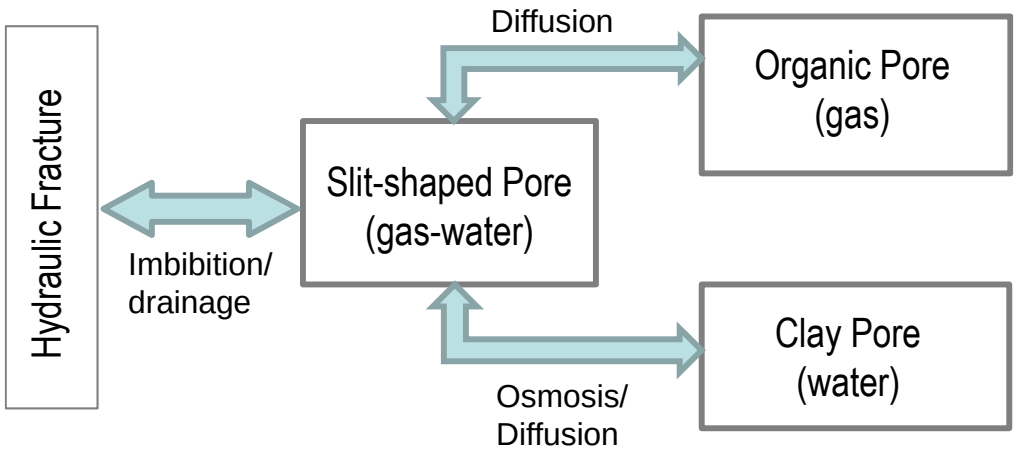

Fig. 11 - Flow paths among hydraulic fractures and slit-shaped, organic, and clay pores, and the dominant flow/transport mechanisms and fluids.

pores contain natural gas in adsorbed- and free-states. A large portion of these pores are nano-scale. Slit-shaped pores, or slit pores, on the other hand, are pores or microcracks developed in the inorganic part of the shale matrix.

The slit pores have a geometry of a narrow channel or a micro-crack. They have hydraulic connection to or transects the organic pores and the clay pores. The length of the slit-shaped pores are varied and may range from one to tens of micrometers. These pores may also be considered as part of the micro- and nano-scale cracks developed parallel to bedding planes. Slit-shaped pores have walls mostly with water-wet wettability and may contain water and natural gas. Clay-pores, on the other hand, are the voids between interlayer clay sheets that contain the formation water. Fig. 11 shows connectivity or flow paths between the hydraulic fracture, slit-shaped pores, organic pores and clay pores and the dominant transport mechanisms.

The presented petrophysical model for shale is a simplification to a much more complicated shale formation. However, this model can serve the purpose of this research, which is to understand the effects of shale-water interactions after hydraulic fracturing that lead to clay swelling and permeability alteration.

Clays are layered silicate minerals (Grim, 1968). They have a basic silicate structure unit that consists of silica tetrahedron and alumina octahedron that are combined in different proportions (typically, 1:1 or 2:1) to form sheet structures that have large amounts of unbalanced electric charges. The varieties of clay minerals are made by different combinations of basic sheet structures with different forms of bonding between the combined sheets, the cation substitutions that may occur in either the tetrahedral or the octahedral sheets, and diverse species of the exchangeable cations in the clay interlayer space.

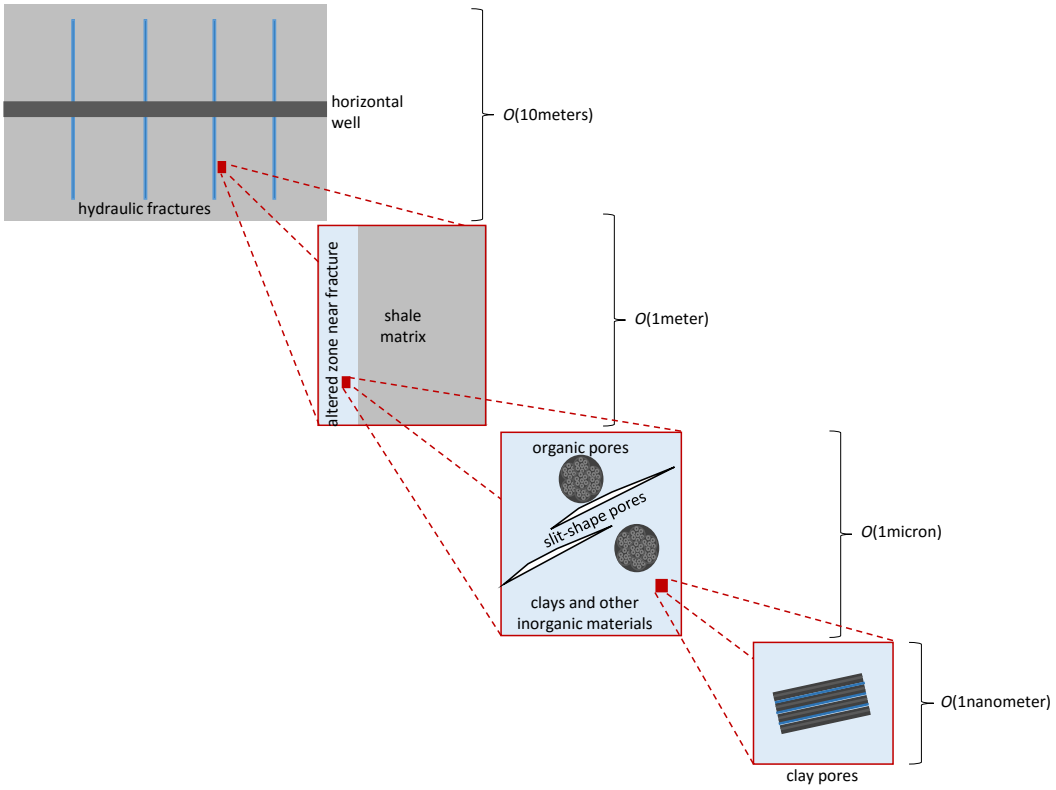

Fig. 12 - Shale-water interactions due to hydraulic fracturing water. After hydraulic fracturing and flowback operations in a shale gas well, water may be left inside fractures and imbibe into shale matrix and then move into clay-pores by osmosis.

Four types of water occur in shale associated with the clays: intercrystalline water, osmotic water, bound water and free water. Porosity is defined as sum of free water, osmotic water, and to a lesser extent intercrystalline, water (Lal, 1999; Asef and Farrokhrouz, 2013). Intercrystalline water is present in association with cations to neutralize negative charges in clay particles, osmotic water is an adsorbed surface layer associated with negative clay charges, bound water is structurally hydrogen and hydroxyl groups within clay molecules, and free water is in the pore space among clay grains. Here, our focus is mostly on the osmotic water or interlayer water present between clay sheets, which may cause swelling pressure.

Fig. 12 illustrates shale-water interactions due to hydraulic fracturing water through flow paths demonstrated in Fig. 11. After a hydraulic fracturing operation is completed, some slickwater remains in the created hydraulic-fractures. This water will interact with shale matrix and create an altered zone where permeability impairment may occur. This permeability impairment, known also as formation damage, can be caused by several mechanisms; one mechanism is build-up of pressure inside clay-pores which dynamically changes with time. This osmotic pressure build-up inside clay pores can give additional stress that may reduce stress-dependent, slit-pore permeability.

2.2. Clay Swelling and Osmosis

Clay minerals can act as semi-permeable membrane because of the negative charges on clay particle surfaces (Marine and Fritz, 1981). The negative charges attract cations in solution to adsorb onto clay surface and form a diffuse layer adjacent to the adsorb layer to create double layer. This double layer tends to prevent passage of charged ions through the semi-permeable membrane and only allow uncharged molecules such as water to pass.

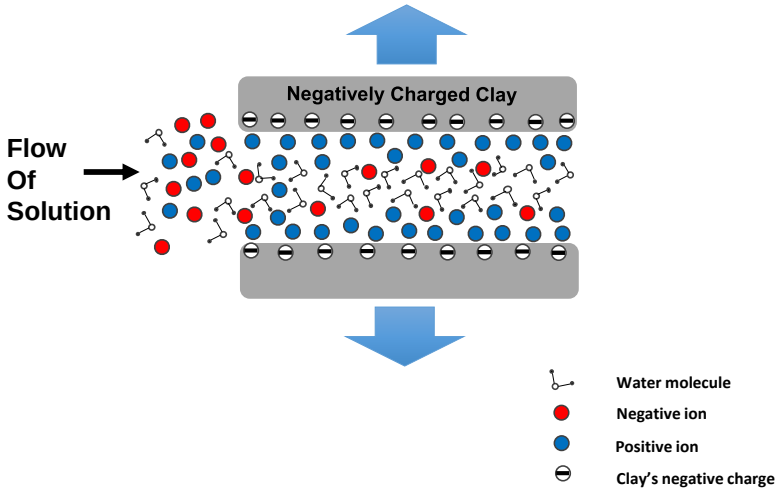

Fig. 13 - Clay acts as a semipermeable membrane due to its negatively charged surface, allowing or reflecting cations and anions according to its membrane efficiency.

When the clay membrane is facing aqueous solution having different salt concentration from solution inside the clay, osmosis will occur such that uncharged water molecules flow from the lower salinity solution into the clay. If the more saline solution is contained within a confined clay membrane such as the clays in the subsurface formations, the water being transported into the confined clay will further increase the hydrostatic pressure inside the clay. The osmotic transport will continue until water activity in both solutions eventually becomes equal. Fig. 13 illustrate clay act as a semipermeable membrane and cause clay swelling.

Clays swelling of is a result of the layered structure of the clay minerals and of the cations adsorbed for the charge equilibrium (Madsen and Müller-Vonmoos, 1989). Two phases of this swelling can may be observed:

- inner-crystalline swelling, which is caused by the hydration of the exchangeable cations of the dry clay; and
- osmotic swelling, which results from the large difference in the ionic concentration, principally the cation concentration, at the surface of the clay layers and in the pore water.

Osmosis can be defined as a transport of water molecules across a selectively permeable material (semipermeable membrane) that allows the flow of water and restricts the passage of ions or salts, which occur when such material separates a solution with different salt concentrations (Fig. 14) (Marine and Fritz, 1981; Medved and Černý, 2013). The fluid flows from the region with a low salt concentration to the region with high salt concentrations and the flow increases the fluid pressure in the high salt concentration region and decreases it in the low salt concentration region. Subsequently, these pressure changes lead to a countering hydraulic flow, until the two opposing fluxes cancel each other and equilibrium is reached.

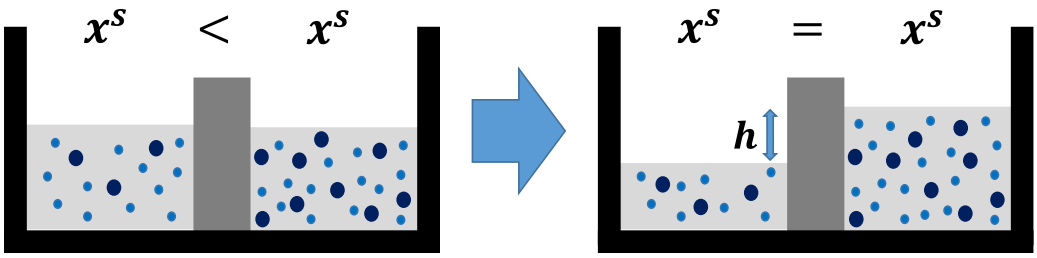

Fig. 14 - Illustration of chemical osmosis adapted from Medved and Černý (2013). A porous material (in the center) that act as a semipermeable membrane permits the passage of the water (the small disks) but not of the solute (the large disks). The hydrostatic pressure increases in the compartment of higher solute concentration until the osmotic pressure ($\nabla\pi = \rho g h$) is reached and the solute concentrations in both compartments equalize.

Osmosis, in general, results not only by a concentration gradient (chemical osmosis) but also by gradients in the electric potential (electro-osmosis) or temperature (thermo-osmosis) (Medved and Černý, 2013). In this study, theoretical description of osmosis follows the chemical osmosis model developed by Bader and Kooi (2005) which assumes the driving forces of mass flux are the hydraulic pressure and the chemical potential gradient. The model has been derived for a solute transport problem involving an aqueous phase with single solute species. The gradient of osmotic pressure is approximated as follows (Bader and Kooi, 2005):

$$\nabla\pi = \theta RT \frac{\rho_f}{M_s} \nabla x^s \qquad (1)$$

where, x^s is the salt mass fraction; M_s is the salt molar mass [kg/mol] and θ is dissociation coefficient for the salt dissociating into θ ions, which, for example, θ = 2 for $MgSO_4$, NaCl and KCl. Salt concentration is the main factor affecting osmotic pressure. However, for different salt type, equal salt concentration may not result in equal osmotic pressure because different salt types have varying molar mass and dissociation coefficient. For salts with equal dissociation coefficient, here θ = 2 for example, the salt with higher molar mass, such as $MgSO_4$ with respect to NaCl and KCl, yield lower osmotic pressure.

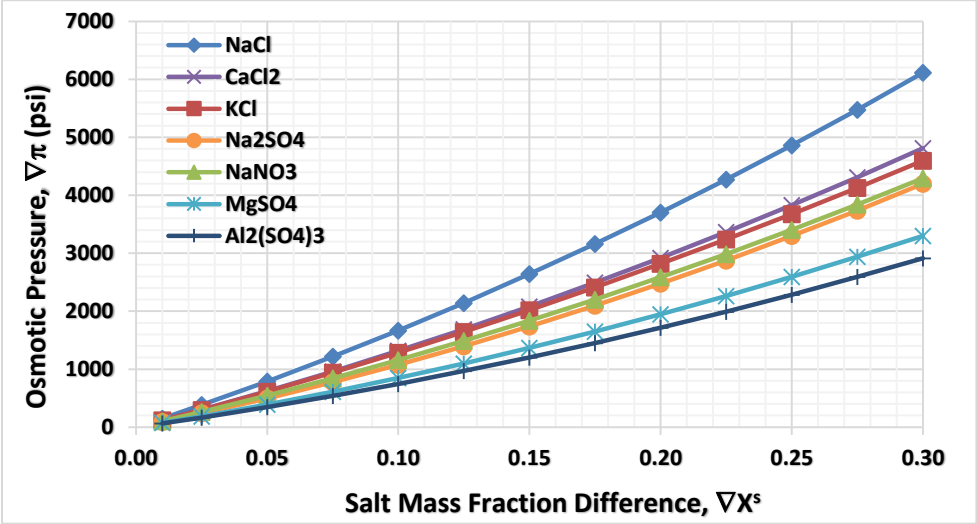

Fig. 15 - Osmotic pressure for different salts and varying salt concentration difference are given at an initial pressure of 1,450 psi and temperature of 100°C, calculated using Eq. 1.

Consider a container holding two aqueous solutions with different salt concentration separated by a semi-permeable membrane initially has pressure of 1,450 psi and temperature of 100°C. The associated pressure increase (i.e., the osmotic pressure) in the side of the semi-permeable membrane containing higher salt concentration can be predicted using Eq. 1. Then the estimated changes in pressure due to osmosis are shown in Fig. 15 for different types of salts and different salt concentration values.

2.3. Gangi's Stress-dependent Permeability with Clay Swelling Effect

As described in the previous section, osmosis is the possible mechanism to generate swelling pressure inside clay pores. Here, we discuss mechanism of formation damage in the altered zone, due to reduction in slit-shaped pore or microcrack permeability caused by the building-up clay swelling pressure. The altered zone is the shale matrix zone adjacent to the hydraulic fracture, which experience changes in reservoir properties due to imbibition of hydraulic-fracturing water into shale matrix.

Experiments on clay samples demonstrate that clay swells when it contacts water, especially the fresh water. Clays may take up water, which, in turn, increase the pressure within the clays and result in clay swelling. Swelling pressure is a combined effect of several physico-chemical forces acting primarily on the clay fabric. These forces are van der Waals attraction, electrostatic Born repulsion, and short-range repulsive-attractive forces generated from hydration/solvation of clay surfaces and the ions inside the interlayer clay pores (van Oort, 2003). I consider clay swelling pressure as stress in addition to other mechanical forces that act on the shale system, including in-situ vertical and horizontal stresses, pore pressure, and stress acting at inter-granular contact points. Here, I propose to use Gangi's stress-dependent permeability equation to account the effect of clay swelling to permeability changes.

Permeability of slit-shaped pores or microcracks is stress-dependent and may be described by Gangi's permeability model (Gangi, 1978; Wasaki and Akkutlu, 2015) as follows:

$$k_I = k_0 \left\{ 1 - \left(\frac{P_{conf} - \chi P}{P_1} \right)^m \right\}^3 \qquad (2)$$

Here, k_I is the slit-pore permeability [m^2]; k_0 is the permeability at zero effective stress [m^2]; P_{conf} is the confining pressure [Pa]; P is the slit-pore pressure; χ is the effective stress coefficient; P_1 is the effective stress when the slit-pores are closed completely (i.e., when $k_I = 0$); m is a coefficient related to the surface roughness of the slit-pores.

In Eq. 2 permeability is a function of effective stress ($P_{conf} - \chi P$). The increase in the effective stress will cause a reduction in permeability because the swelling pressure inside the clay pores gives additional stress to the slit-shaped pores, which account for increasing confining pressure, thus reducing the permeability of the slit-shaped pores (Fig. 16).

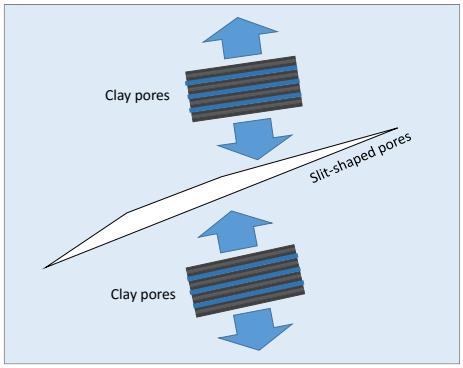

Fig. 16 - Clay swelling effect on permeability reduction: the increase of clay pore pressure gives additional stress to the confining pressure around the slit-pore, reducing slit aperture and permeability.

3. MODELING AQUEOUS-PHASE TRANSPORT IN CLAYS*

In this chapter I discuss the mathematical model and numerical solution of aqueous phase transport through clays. The objective of this modeling was to validate transport of water and salt through clay pores. Subsequently, this model was used in the modeling of two-phase flow, aqueous- and gaseous-phase, through the triple-porosity shale matrix.

The model and simulator are expansions of TAMU-FTSIM, which is a variant of the TOUGH+ simulator (Moridis, 2014; Moridis and Freeman, 2014). The current simulator considers non-isothermal flow of two-phase (aqueous and gaseous phases) with one component, H_2O. The new simulator in this chapter extends to non-isothermal flow of two-phases with two components, H_2O and salt.

3.1. Mathematical Model

3.1.1. Bader and Kooi's Water and Salt Transport in Clay Model

The mathematical model of aqueous-phase transport in clays in this work follows the mathematical model of solute and water transport in semi-permeable clay membranes developed by Bader and Kooi (2005). Flows can be described as direct and coupled flow phenomena induced by gradients in pressure, chemical potential, electrical potential, and temperature (Bader and Kooi, 2005) (Table 1). In their model, the flow and transport of water and solute through clay membrane is driven by hydraulic and chemical osmosis gradients. The model is based on non-equilibrium thermodynamics, assuming local equilibrium is established, the fluxes are related linearly to the driving forces and validity of Onsager's reciprocal law (Bader and Kooi, 2005).

---

* Part of this chapter is reprinted with permission: "Numerical Simulation of Hydraulic Fracturing Water Effects on Shale Gas Permeability Alteration" by Eveline, V. F., Akkutlu, I Y. and Moridis, G. J. 2017. *Transport in Porous Media*, Vol. 116, 727 – 752, Copyright 2016 Springer.

Table 1 - Direct and coupled flow phenomena. On the diagonal are the well-known relations between fluxes and driving forces. The non-diagonal elements correspond to the coupled processes that may be significant under special circumstances, i.e. in the presence of a semi-permeable membrane. Reprinted from Bader and Kooi (2005).

Gradient **X** →				
Flow **J** ↓	**Hydraulic**	**Chemical**	**Electrical**	**Temperature**
Fluid	Hydraulic flow (Darcy's Law)	Chemical osmosis	Electro-osmosis	Thermo-osmosis
Solute	Ultrafiltration	Diffusion (Fick's Law)	Electrophoresis	Soret effect
Charge	Rouss effect	Diffusion potential	Electrical conduction (Ohm's Law)	Seebeck effect
Heat	Isothermal heat transfer	DuFour effect	Peltier effect	Thermal conduction (Fourier's Law)

Their derivation started with the linear phenomenological equations, which relate the driving forces X_j to the mass fluxes J_i:

$$J_i = \sum_{j=1}^{N} L_{ij} X_j \qquad (3)$$

Here, L_{ij} is the phenomenological coefficient. A system with *N* fluxes and driving forces generally has N^2 phenomenological coefficients to be evaluated. However, assuming Onsager's reciprocal law, this matrix of coefficients can be considered symmetric as follows:

$$L_{ij} = L_{ji} \qquad (4)$$

The basic flux equations in terms of pressure (P) and chemical potential of the solute (μ_s) are:

$$q = L_{11}\nabla(-P) + L_{12}\nabla(-\mu^s) \qquad (5)$$

$$J_n^d = L_{21}\nabla(-P) + L_{22}\nabla(-\mu^s) \quad (6)$$

where,

q is solution flux or the specific discharge, [m/s]

J_n^d is the diffusive molar flux of solute relative to the solution, [mol/m^2.s]

μ^s is chemical potential of the solute; [kg/ m^2.s]

The solute concentration is defined as:

$$c_s = \frac{\rho_f x^s}{M_s} \quad (7)$$

where,

c_s is solute concentration [mol/m3]

x^s is the salt mass fraction, [-]

ρ_f is the fluid density, [kg/m^3]

M_s is the molar mass of the solute, [kg/mol]

The chemical potential of the solute (μ^s) is defined as:

$$\mu^s = \mu_0^s + \theta RT \ln(a^s) \quad (8)$$

where,

μ_0^s is the constant chemical potential for the pure solvent, [kg/m.s^2]

θ is the dissociation coefficient for the salt dissociating into θ ions, which equals 2 for NaCl

a^s is the solute activity, [-]

R is the gas constant, [J/mol.K]

T is the temperature, [K]

Taking the gradient of the chemical potential of the solute yield:

$$\nabla\mu^s = \theta RT\frac{1}{a^s}\nabla a^s \qquad (\ 9\ )$$

The solute activity (a^s) can be defined as:

$$a^s = \gamma x^s\frac{M_f}{M_s} \qquad (\ 10\ )$$

And, the salt mass fraction (x^s) can be defined as:

$$x^s = \frac{\rho_s}{\rho_f} \qquad (\ 11\ )$$

where,

γ	is the activity coefficient, [-]
M_s and M_f	is the molar mass of the solute and the fluid, [kg/mol]
$\rho_s\ and\ \rho_f$	is the density of the solute and the fluid, [kg/m^3]

Substituting Eq. 10 and Eq. 11 into Eq. 9 resulting the gradient of solute chemical potential ($\nabla\mu^s$) as function of the gradient of salt mass fraction (∇x^s):

$$\nabla\mu^s = \theta RT\frac{\rho_f}{\rho_s}\nabla x^s \qquad (\ 12\ )$$

The gradient of osmotic pressure ($\nabla\pi$) is defined as:

$$\nabla\pi = c_s\nabla\mu^s \qquad (\ 13\ )$$

Substituting the solute concentration (Eq. 7) and the gradient of solute chemical potential (Eq. 12), we get the gradient of osmotic pressure ($\nabla\pi$) as function of salt mass fraction gradient (∇x^s) as follows:

$$\nabla\pi = \theta RT \frac{\rho_f}{M_s} \nabla x^s \qquad (\ 14\ )$$

The reflection coefficient or the membrane efficiency ($\mathcal{R}$) is defined as the ratio of the hydraulic gradient (∇P) and the gradient of osmotic pressure ($\nabla\pi$) for zero solution flow, i.e. $q = 0$:

$$\mathcal{R} = \left.\frac{\nabla p}{\nabla\pi}\right|_{q=0} = \left.\frac{\nabla p}{c_s \nabla \mu_s}\right|_{q=0} \qquad (\ 15\ )$$

Therefore:

$$q = 0 = L_{11}\nabla(-P) + L_{12}\nabla(-\mu^s) \qquad (\ 16\ )$$

After substituting and rearranging Eq. 16 we get the membrane efficiency ($\mathcal{R}$) as:

$$\mathcal{R} = -\frac{L_{12}}{c_s L_{11}} \qquad (\ 17\ )$$

where, the coefficient L_{11} is a transport coefficient, defined as the permeability of the membrane (k) over the fluid viscosity (μ):

$$L_{11} = \frac{k}{\mu} \qquad (\ 18\ )$$

After substituting and rearranging Eq. 17 we get the coefficient L_{12}:

$$L_{12} = -\mathcal{R} c_s L_{11} = -\mathcal{R} \frac{\rho_s}{M_s} \frac{k}{\mu} \qquad (\ 19\ )$$

The second term in R.H.S in the solution flux equation (Eq. 5) can be written as:

$$L_{12}\nabla(-\mu^s) = \mathcal{R}\frac{k}{\mu}\frac{\rho_f}{M_s}\theta RT\nabla x^s = \lambda_t\rho_f\nabla x^s \quad (20)$$

Here, λ_t is a transport coefficient, defined as follows:

$$\lambda_t = \mathcal{R}\frac{k_m}{\mu_A M_s}\theta RT \quad (21)$$

Finally, the first flux equation, the solution flux (Eq. 5) can be rewritten as:

$$q = -\frac{k}{\mu}\nabla P + \lambda_t\rho_f\nabla x^s \quad (22)$$

Rearranging Eq. 5, the hydraulic gradient is defined as:

$$\nabla(-P) = \frac{1}{L_{11}}(q + L_{12}\nabla\mu^s) \quad (23)$$

Substituting into the second flux equation, the diffusive molar flux of solute relative to the solution (Eq. 6), yields:

$$J_n^d = L_{21}\left(\frac{q}{L_{11}} + \frac{L_{12}\nabla\mu^s}{L_{11}}\right) - L_{22}\nabla\mu^s \quad (24)$$

Using the Onsager's reciprocal law that $L_{12} = L_{21}$, substituting Eq. 19, the solute concentration (c_s), and λ into the previous equation, and rearranging, yielding:

$$J_n^d = -\mathcal{R}\frac{\rho_f x^s}{M_s}q + \left(\mathcal{R}\lambda_t\frac{\rho_f x^s}{M_s} - L_{22}\frac{\theta RT}{\rho_s}\right)\rho_f\nabla x^s \quad (25)$$

The solute permeability coefficient (η) is defined as:

$$\eta = \frac{L_{22}\frac{\theta RT}{\rho_s} - \mathcal{R}\lambda_t \frac{\rho_f x^s}{M_s}}{\frac{\theta RT}{M_s}} \qquad (\ 26\ )$$

and, the effective diffusion coefficient (D) can be defined as:

$$D = \eta\theta RT \qquad (\ 27\ )$$

Substituting the definition of solute permeability coefficient (η), resulting:

$$J_n^d = -\mathcal{R}\frac{\rho_f x^s}{M_s} q + \left(-\eta \frac{\theta RT}{M_s}\right)\rho_f \nabla x^s \qquad (\ 28\ )$$

Finally, after substituting the effective diffusion coefficient (D), the diffusive molar flux of solute relative to the solution (J_n^d) can be written as:

$$J_n^d = -\mathcal{R}\frac{\rho_f x^s}{M_s} q - \frac{\rho_f}{M_s} D\nabla x^s \qquad (\ 29\ )$$

The solute mass flux (J_s^d) can be defined as:

$$J_s^d = J_n^d M_s = -\mathcal{R}\rho_f x^s q - \rho_f D\nabla x^s \qquad (\ 30\ )$$

The solute mass flux relative to porous medium (J_s) is defined as:

$$J_s = J_s^d + x^s \rho_f q \qquad (\ 31\ )$$

Finally, after substituting the solute mass flux (J_s^d) and the solution flux (q), the solute mass flux relative to porous medium (J_s) is written as:

$$J_s = (1 - \mathcal{R})x^s \rho_f \left(-\frac{k}{\mu}\nabla P + \lambda_t \rho_f \nabla x^s\right) - \rho_f D \nabla x^s \qquad (\ 32\ )$$

3.1.2. General Mass and Energy Balance Equation

The mass and energy balance equations can be written as follows (Pruess et al., 1999; Moridis, 2014):

$$\frac{d}{dt}\int_{V_n} M^\kappa dV_n = \int_{\Gamma_n} \mathbf{F}^\kappa \bullet \mathbf{n} d\Gamma_n + \int_{V_n} q^\kappa dV_n \qquad (\ 33\ )$$

where, V_n is a volume element n; M^κ is mass or energy accumulation of component κ; $\mathbf{F}^\kappa$ is mass or heat flux of component κ; **n** is a normal vector on surface element $d\Gamma_n$, pointing inward into V_n; and q^κ is the source/sink of component κ. The integration is over an arbitrary subdomain V_n of the flow system under study, bounded by the closed surface Γ_n.

By applying Gauss' divergence theorem, Eq. 33 can be converted into the following partial differential equation (Pruess et al., 1999):

$$\frac{dM^\kappa}{dt} = -div\mathbf{F}^\kappa + q^\kappa \qquad (\ 34\ )$$

The mass accumulation of component κ (M^κ) is:

$$M^\kappa = \sum_{\beta=A,G} \phi S_\beta \rho_\beta x_\beta^\kappa \qquad (\ 35\ )$$

where, ϕ is the porosity of the porous medium, S_β is the saturation of phase β, S_β is the density of phase β, and x_β^κ is the mass fraction of component κ in phase β.

The flux of component κ ($\mathbf{F}^\kappa$) is the summation of component κ in all phases:

$$\mathbf{F}^\kappa = \sum_{\beta=A,G} \mathbf{F}_\beta^\kappa \qquad (\ 36\ )$$

The heat accumulation (M^Θ) is calculated as:

$$M^\Theta = (1-\phi)\rho_R C_R T + \sum_{\beta=A,G} \phi S_\beta \rho_\beta U_\beta \qquad (\ 37\ )$$

where, ρ_R is the rock density [kg/m^3], C_R is heat capacity of dry rock [J kg^{-1} K^{-1}], and U_β is the specific internal energy of phase β [J kg-1].

The heat flux ($\mathbf{F}^\Theta$):

$$\mathbf{F}^\Theta = -K_T \nabla T + \sum_{\beta=A,G} h_\beta \mathbf{F}_\beta^\Theta \qquad (\ 38\ )$$

where, K_T is the composite thermal conductivity of the rock and fluid [W m^{-1} K^{-1}], and h_β is the specific enthalpy of phase β [J kg^{-1}].

3.1.3. Mass and Energy Balance Equation for Water and Salt Transport in Clays

The H_2O mass balance equation for single aqueous-phase flow:

$$\frac{\partial}{\partial t}\left(x_A^{H_2O}\rho_A\phi\right) + \nabla.\,\mathbf{F}_A^{H_2O} = q^{H_2O} \qquad (\ 39\ )$$

The salt mass balance equation for single aqueous-phase flow

$$\frac{\partial}{\partial t}\left(x_A^{Salt}\rho_A\phi\right) + \nabla.\mathbf{F}_{\mathrm{A}}^{\mathrm{Salt}} = q^{Salt} \qquad (\ 40\ )$$

The aqueous-phase velocity ($\mathbf{q}_A$) is driven by hydraulic pressure gradient (∇P_A) and salt concentration gradient (∇x_A^{Salt}), expressed as follows:

$$\mathbf{q}_A = -\frac{k_m}{\mu_A}\nabla P_A + \lambda_t \rho_A \nabla x_A^{Salt} \qquad (\ 41\ )$$

The coefficient, λ_t, is a coefficient which include two transport coefficients, the permeability of the clay-membrane (k_m) and the salt reflection coefficient ($\mathcal{R}$). The salt reflection coefficient which from here forward will be called as the clay-membrane efficiency has a value between 0 and 1, where $\mathcal{R}$ =1 for ideal membrane, $\mathcal{R}$ =0 for non-reflective membrane and 0< $\mathcal{R}$<1 for leaky/non-ideal. The transport coefficient λ_t is expressed as in Eq. 21 as follows:

$$\lambda_t = \frac{\mathcal{R}k_m}{\mu_A M_s}\theta RT \qquad (\ 42\ )$$

where, M_s is the salt molar mass [kg/mol] and θ is dissociation coefficient for the salt dissociating into θ ions, which, for example, θ = 2 for $MgSO_4$, NaCl and KCl.

The total mass flux of H_2O for single aqueous-phase flow through clay membrane is written as follows:

$$\mathbf{F}_A^{H_2O} = x_A^{H_2O}\rho_A\mathbf{q}_A = x_A^{H_2O}\rho_A\left\{-\frac{k_m}{\mu_A}\nabla(P_A) + \lambda_t\rho_A\nabla\left(x_A^{Salt}\right)\right\} \qquad (\ 43\ )$$

The first term in R.H.S. is Darcy's flow driven by pressure gradient, and the second term is osmotic flow driven by salt concentration gradient. Here, I introduced the following:

$x_A^{H_2O}$ is the H_2O mass fraction in aqueous phase, [-]

x_A^{Salt} is the salt mass fraction in aqueous phase, [-]

The total salt-mass flux ($\mathbf{F}_A^{Salt}$) is defined as follows (Bader and Kooi, 2005):

$$\mathbf{F}_A^{Salt} = (1-\mathcal{R})\rho_A x_A^{Salt}\mathbf{q}_A - \rho_A D_A^{Salt}\nabla\left(x_A^{Salt}\right) \quad (44)$$

where, the effective salt diffusion coefficient (D_A^{Salt}) is defined as:

$$D_A^{Salt} = (1-\mathcal{R})\phi\tau_A D_{o,A}^{Salt} \quad (45)$$

Here, $D_{o,A}^{Salt}$ is the free-molecular diffusion coefficient of dissolved salt in the aqueous-phase [m^2/s]; ϕ is the clay porosity; and τ_A is the tortuosity coefficient [-].

Substituting $\mathbf{q}_A$, the total salt mass flux:

$$\begin{aligned}\mathbf{F}_A^{Salt} = (1-\mathcal{R})\rho_A x_A^{Salt}\left\{-\frac{k_m}{\mu_A}\nabla(P_A) + \lambda_t\rho_A\nabla\left(x_A^{Salt}\right)\right\} \\ -(1-\mathcal{R})\rho_A\phi\tau_A D_{o,A}^{Salt}\nabla\left(x_A^{Salt}\right)\end{aligned} \quad (46)$$

The total salt mass flux ($\mathbf{F}_A^{Salt}$) through clay membrane has two terms. The first term is salt flux associated with Darcy's flux and osmosis flux that salt may filtrate or reflect through clay membrane depending on the efficiency of the clay membrane. The second term is diffusive salt flux that also may filtrate or reflect through clay as controlled by the clay membrane efficiency.

3.1.4. Constitutive, Equilibrium Restriction and Constraint Equations

The thermophysical properties of water including density, viscosity, specific enthalpy, and thermal conductivity are calculated using the IAWPS formulation, 1997 (Wagner et al., 2000).

The mass fraction of component κ in phase β:

$$x_\beta^\kappa = \frac{y_\beta^\kappa {M_w}^\kappa}{\sum_\kappa \left(y_\beta^\kappa {M_w}^\kappa\right)} \quad (47)$$

where,

y_β^κ is the molar fraction of component κ in phase β

${M_w}^\kappa$ is the molecular weight component κ in phase β, [kg/mole]

The constraints are applied as follows:

$$x_A^{H_2O} + x_A^{Salt} = 1 \quad (48)$$

where,

$x_A^{H_2O}$ and x_A^{Salt} is the H_2O and salt mass fraction in aqueous phase, [-]

The density of aqueous phase with the dissolved salt (ρ_A) is then calculated as follows:

$$\rho_A = x_A^{H_2O} \rho_A^{H_2O} + x_A^{Salt} \rho^{salt} \quad (49)$$

where,

$\rho_A^{H_2O}$ is the density of water in aqueous phase, [kg/m^3]

ρ^{salt} is the density of salt, [kg/m^3]

The porosity of porous medium is calculated as function of pressure and temperature, as follows:

$$\phi = \phi_{init} \mathrm{e}^{\left(C_{\phi}(P-P_{init})+\beta_t(T-T_{init})\right)} \quad (50)$$

where,

C_{ϕ} is pore compressibility, [Pa^{-1}]

β_t is pore thermal expansion, [K^{-1}]

The permeability of porous medium is calculated as function of porosity (Rutqvist and Tsang, 2002), as follows:

$$k = k_{init} \mathrm{e}^{\left[22.2\left(\frac{\phi}{\phi_{init}}-1\right)\right]} \quad (51)$$

3.2. Numerical Solution using Integral Finite Difference Method

3.2.1. Discretization of Mass and Energy Balance Equations

The mass and energy balance equations were discretized in space using the integral finite difference method (Narasimhan and Witherspoon, 1976), as follows:

$$\int_{V_n} M dV = V_n M_n \quad (52)$$

where,

M is a volume-normalized extensive quantity

M_n is the average value of M over V_n

Surface integrals are approximated as a discrete sum of averages over surface segments A_{nm}:

$$\int_{\Gamma_n} \mathbf{F} \bullet \mathbf{n} d\Gamma_n = \sum_m A_{nm} \mathbf{F}_{nm} \quad (53)$$

where, $\mathbf{F}_{nm}$is the average value of the (inward) normal component of **F** over the surface segments A_{nm} between volume elements V_n and V_m

The discretized flux is expressed in terms of averages over parameters for volume elements V_n and V_m, which can be written as follows for Darcy's flux:

$$\mathbf{F}_{\beta,nm} = -k_{nm}\left[\frac{k_{r\beta}\rho_{\beta}}{\mu_{\beta}}\right]_{nm}\left[\left(\frac{P_{\beta,m} - P_{\beta,n}}{D_{nm}}\right) - \rho_{\beta,nm}\mathbf{g}_{nm}\right] \qquad (\ 54\ )$$

The subscripts *nm* denote a suitable averaging at the interface between elements *n* and *m*, such as interpolation, harmonic weighting and upstream weighting. Further, I introduced the following:

D_{nm} is the distance between the nodal points *n* and *m*

$\mathbf{g}_{nm}$ is the component of gravitational acceleration in the direction from *m* to *n*

Time was discretized using first-order backward finite difference. All the unknown thermodynamic parameters in the flux and source/sink terms were evaluated at the new time level or in fully implicit manner to get the numerical stability for efficient computation in this nonlinear problems.

After time discretization and introducing residuals, $R_n^{\kappa,\mathrm{k+1}}$, the mass and energy balance equations become a set of coupled non-linear algebraic equations as follows:

$$R_n^{\kappa,\mathrm{k+1}} = M_n^{\kappa,\mathrm{k+1}} - M_n^{\kappa,\mathrm{k}} - \frac{\Delta t}{V_n}\left[\sum_m A_{nm}\mathbf{F}_{nm}^{\kappa,\mathrm{k+1}} + V_n q_n^{\kappa,\mathrm{k+1}}\right] = 0 \qquad (\ 55\ )$$

where, k and k+1 are the current time and the new time level, respectively; $R_n^{\kappa,\mathrm{k+1}}$ is the residuals of component κ at time k+1, in element n; Δt is the time step.

In this simulator, we have three residual equations for component H_2O, salt and heat to be solved for each volume element. The unknowns are the $N_E * N_\kappa$ independent primary variables (X_i, for $i = 1, \dots, N_E * N_\kappa$) where N_E is the number of elements and N_κ is the number of equations for each element.

3.2.2. Primary Variables

The new model developed in this work to simulate aqueous phase solution transport in clays is an expansion of an existing simulator for flow of water with single component, H_2O, and includes three thermos-physical state, which are single aqueous phase, single gas phase and two-phases, aqueous and gas phases. However, as we intended to simulate only single aqueous phase through clay, here we discuss only the thermophysical state of single aqueous phase.

Since we had three residual equations to be solved, we need to select three primary variables, as the unknowns. We chose primary variables that can uniquely described the system which involving osmosis. The primary variables are pressure, salt molar fraction and temperature (Table 2).

3.2.3. The Newton/Raphson Iteration

Eq. 55 was solved numerically using the Newton/Raphson iteration method as follows. I introduced an iteration index, *p*, and expanded the residuals in Eq. 55 with respect to the primary variable at iteration step *p* + 1 in a Taylor series as follows:

$$R_n^{\kappa,k+1}{}_{(X_{i,p+1})} = R_n^{\kappa,k+1}{}_{(X_{i,p})} + \sum_i \left.\frac{\partial R_n^{\kappa,k+1}}{\partial X_i}\right|_p (X_{i,p+1} - X_{i,p}) + \cdots = 0 \qquad (56)$$

Table 2 – State and primary variables for the single aqueous phase transport in clays

State	Primary Variables (X_i)
Single phase - aqueous	Pressure (P_A) Salt molar fraction (y_A^{Salt}) Temperature (T)

I obtained Jacobian matrix equations by retaining only the first derivative of Eq. 56 and rearranging terms to yield:

$$-\sum_i \left.\frac{\partial R_n^{\kappa,k+1}}{\partial X_i}\right|_p \left(X_{i,p+1} - X_{i,p}\right) = R_n^{\kappa,k+1}{}_{(X_{i,p})} \qquad (\ 57\ )$$

The Jacobian matrix, $\sum_i \frac{\partial R_n^{\kappa,k+1}}{\partial X_i}$ was constructed by differentiating the set of residual equations in terms of primary variables (X_i). The dimension of the Jacobian matrix is ($N_E * N_\kappa$)*($N_E * N_\kappa$).

Solution for Eq. 57 was proceed in an iterative manner until the residuals ($R_n^{\kappa,k+1}$) were reduced below a preset convergence tolerance.

The relative convergence criterion is defined as:

$$\left|\frac{R_{n,p+1}^{\kappa,k+1}}{M_{n,p+1}^{\kappa,k+1}}\right| \leq \epsilon_1 \qquad (\ 58\ )$$

Here, we used the criteria from 1.0E-5 to 1.0E-6. When the accumulation terms are smaller than ϵ_2, then an absolute convergence criterion is applied:

$$R_{n,p+1}^{\kappa,k+1} \leq \epsilon_1 \epsilon_2 \qquad (\ 59\ )$$

The default value ϵ_2 of is 1.

3.3. Validation of the Numerical Model with Experiment

We validated the mathematical model and numerical solution of aqueous-phase flow through clay involving osmosis by conducting simulation and matching an experiment described in Keijzer (2000) and Bader and Kooi (2005).

3.3.1. Description of Keijzer's Problem

The experiment was conducted using a bentonite clay sample for approximately 23 days. In the experimental apparatus, the clay sample with a thickness of approximately 2 mm was wedged between two porous stones. The initial pressure was 5.0×10^5 Pa and other parameters are described in Table 3. During the experiment, one end of the sample was connected to a closed reservoir containing high salt concentration solution and the other end was connected to a reservoir containing low salt concentration solution (Fig. 17) with no pressure gradient being applied. To simulate the problem, I used 20 elements attributed as the porous stones and the clay sample (Fig. 17).

Table 3 – Parameters used in the simulation of the Keijzer experiment (Keijzer, 2000; Bader and Kooi, 2005)

Parameter	Value	Unit
Rock and Fluid Properties		
Initial Pressure	5.00E+05	Pa
Initial Temperature	25	˚C
Porosity	0.56	
Permeability	1.20E-09	m^2
Salt diffusion coefficient	2.60E-13	m^2/s
Membrane efficiency ($\mathcal{R}$)	0.0165	
Salt concentration in low salt reservoir	0.01	mol/L NaCl
Salt concentration in high salt reservoir	0.1	mol/L NaCl

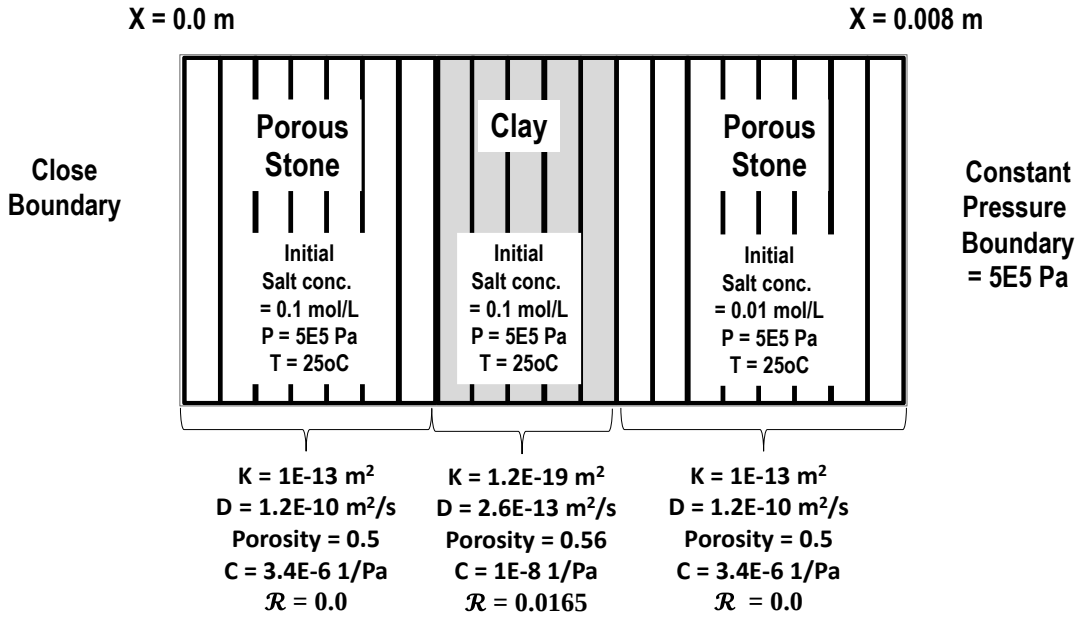

Fig. 17 - Simulation domain of Keijzer experiment, adapted from Bader and Kooi (2005).

3.3.2. Simulation Results and Analysis

We simulated for approximately 29 days of experiment (2.0×10^6 s). The simulation result matched pressure increase due to osmosis using membrane efficiency of 0.0165 (Fig. 18) compared to experimental data. Fig. 18 shows delta pressure (refer to the initial pressure) inside a clay sample whose ends are connected to two separate reservoirs with different salt concentration. The clay sample itself contains high salt concentration, equal to that in one of the reservoirs.

Initially, pressure in the whole arrangement (clay and the two reservoirs) was equal. As the experiment was started, there was water influx from low salt reservoir into clay due to osmosis and pressure inside clay was increasing immediately. However, with time, pressure inside the clay turned to decreasing behavior. This was because of two reasons: first, as pressure in clay increased, there was reverse influx from clay into the low salt reservoir driven by pressure; second, the clay membrane efficiency was not 100%,

therefore the dissolved salt ions in the aqueous phase can flow in and out of the clay sample, which caused the initial high salt concentration in the clay was lower than its initial value; this, in turn, lowered the osmotic water influx. Fig. 19 and Fig. 20 show delta pressure and solute mass fraction profile at different time.

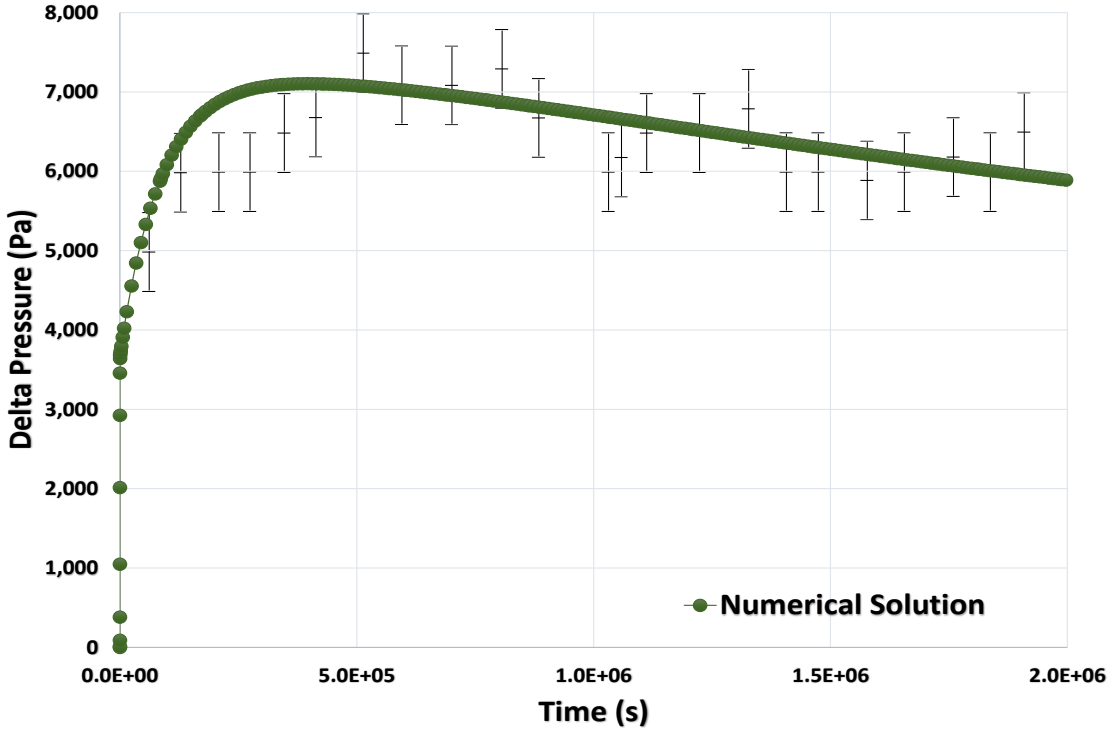

Fig. 18 - Comparison between simulation of osmosis experiment on clay sample results and the experimental data, adapted from Bader and Kooi (2005). The experiment data is the solid vertical black lines and the numerical simulation data resulted from this work is the green curve.

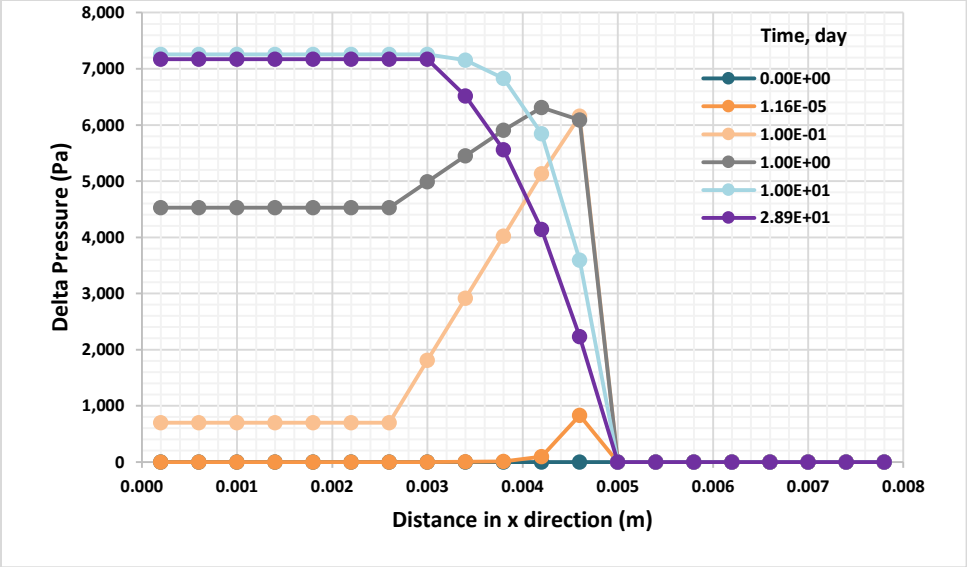

Fig. 19 - Delta pressure profile with time

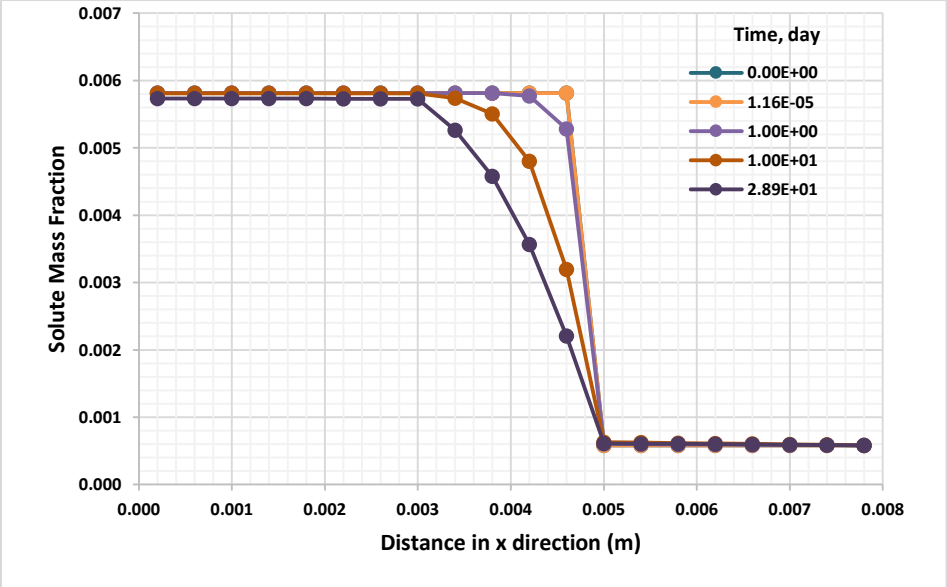

Fig. 20 - Solute mass fraction profile with time

3.4. Description of Geometry and Parameters in Simulation Case Studies

Next, to understand behavior of the osmosis-related pressure increase (i.e., swelling pressure), we used the validated model in a series of forward simulations varying salt concentration differences. In these studies, we estimated the distribution of pressure across the clay. We also conducted simulations using different membrane efficiency. The simulations were one-dimensional (1D) with dimensions of 5x100x10 m, which was divided into 500 equal-size elements in the x-direction. The initial pressure was 2.07E+7 Pa, and the temperature was 50^{o}C. The clay had an initial permeability of 218 nD and porosity of 10%. The first gridblock (corresponding to the fracture element) had a constant pressure of 2.07E+7 Pa, a temperature of 50^{o}C and a NaCl salinity with a mass fraction of 0.01. Initially, the other elements of the system were fully saturated with H_2O with a NaCl mass fraction 0.05. Fig. 21 shows the simulation results after 90 days.

3.5. Simulation Results and Analysis

For a membrane efficiency of 10%, the results show that the salt concentration difference raised the pressure in the clay pores about 4.0E+5 Pa in less than 2 day within a distance of 10 cm from the fracture. At the 55th day, the distance over which the pressure rose by 4.0E+5 Pa extends to 1 m. This pressure increase is due to the large contrast in salt concentration between the two adjacent elements. However, due to limited membrane efficiency, some of the salt ions can freely move across the element boundaries. Consequently, the observed pressure increase cannot reach the ideal osmotic pressure value and stays somewhat low. Initially, it is the chemical potential gradient that drives the water flux from the element with low salt concentration toward the adjacent element with high concentration. As the pressure increases, the hydraulic gradient begins to control the flux and drive water away from the fracture element.

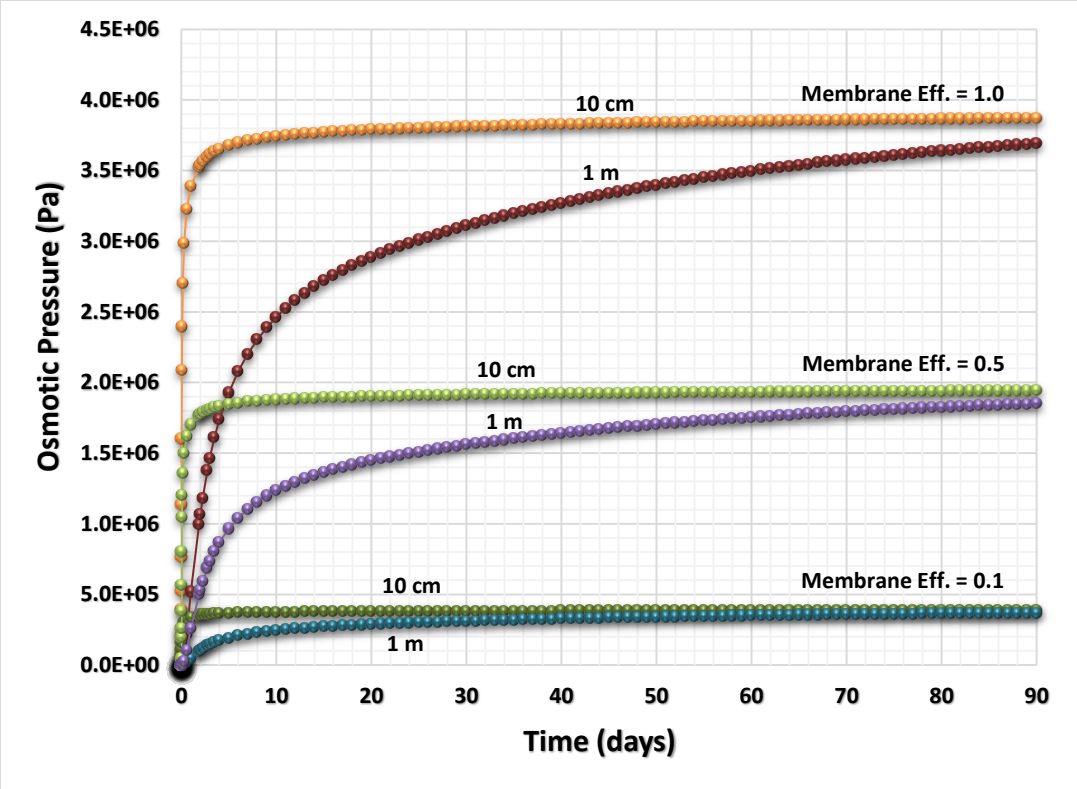

Fig. 21 - Pressure evolution up to 90 days within a distance of 10 and 100 cm from a constant pressure element at the left boundary with varying membrane efficiency: 10%, 50% and 100%

In the case of membrane efficiency of 50%, the pressure increase predicted numerically is much higher. The existing contrast in salt concentration raises the pressure now to about 1.7E+6 Pa in less than 2 day within a distance of 10 cm from the fracture boundary, and to 1 m at about 55 day, respectively. As in to previous case, the limited membrane efficiency can cause some of the salt ions to move freely across the element boundaries, thus preventing the pressure increase to reach the value of the ideal osmotic pressure.

Using a membrane efficiency of 100% (ideal membrane), the pressure increase now reaches the ideal osmotic pressure value of about 3.8E+6 Pa which is comparable to the osmotic pressure calculated using Eq. 1. The salt concentration difference raises the

pressure now to about 3.5E+6 in less than 2 day within a distance of 10 cm from the fracture boundary, and to 1 m at about 55 day, respectively.

The simulation results show the importance of membrane efficiency value on the clay pore pressure. In the subsurface, compacted clays having porosity less than 10% with NaCl concentration about 55,000 ppm can have high membrane efficiency which can be more than 95% for montmorillonite, chlorite, and illite and about 90% membrane efficiency for kaolinite (Marine and Fritz, 1981). Clearly, clay swelling pressure can then be high. Thus, one should be aware of the possibility of significant formation damage due to clay swelling pressure in the formation near the fracture.

4. MODELING OF TWO-PHASE FLOW IN SHALE GAS FORMATION WITH CLAY-SWELLING EFFECT*

This chapter introduces mathematical formulation and a model developed to simulate the two-phase (aqueous and gaseous) flow in shale gas reservoirs with three distinct pore types (organic pores, inorganic slit-shaped pores and clay pores) applying the conceptual petrophysical model described in Chapter 2. The objective of this modeling effort was to clarify how imbibition and osmosis mechanisms affects permeability alteration as result of shale-water interactions during extended shut-in times following hydraulic fracturing. These mechanisms cause clay-pore pressure increase and the associated clay swelling effect on the permeability alteration.

The new simulator is an extension of previous simulator as described in Chapter 3. The new simulator includes two phases, water and gas, with three components, H_2O, CH_4 and salt distributed in three pore types (organic, slit and clay pores). The organic pores contain gas phase, which consists of CH_4 only, as free-gas and adsorbed-gas. The slit pores contain water and gas phases consisting of three components, H_2O, CH_4 and salt. The clay pores on the other hand, contain water phase consisting of three components, H_2O, CH_4 and salt.

4.1. Mathematical Model

4.1.1. Mass and Energy Balance for a Multi-porosity Gas Shale Matrix

Shale gas reservoir is modeled as a rock containing three pore types in its system, and the total porosity is the summation of all porosities:

$$\phi_{tot} = \phi_I + \phi_k + \phi_c \qquad (60)$$

* Part of this chapter is reprinted with permission: "Numerical Simulation of Hydraulic Fracturing Water Effects on Shale Gas Permeability Alteration" by Eveline, V. F., Akkutlu, I Y. and Moridis, G. J. 2017. *Transport in Porous Media*, Vol. 116, 727 – 752, Copyright 2016 Springer.

Here, ϕ_I is the porosity of slit pore, ϕ_k is the porosity of kerogen pore and ϕ_c is the porosity of clay pore.

4.1.1.1. H_2O Mass Balance Equation

H_2O exists in the aqueous and gaseous phases in slit pores (ϕ_I) and in the aqueous-phase in clay pores (ϕ_c). The H_2O mass balance equation for two-phase flow can be written as follows:

$$\frac{\partial}{\partial t}\{\phi_I(x_A^{H_2O}\rho_A S_A + x_G^{H_2O}\rho_G S_G)\} + \nabla.\left\{\mathbf{F}_A^{H_2O}\big|_{\text{adv}} + \mathbf{F}_G^{H_2O}\big|_{\text{adv}} + \mathbf{F}_A^{H_2O}\big|_{\text{dif}} + \mathbf{F}_G^{H_2O}\big|_{\text{dif}}\right\} + w_{A,Ic}^{H_2O} = q^{H_2O} \quad (61)$$

In the above equation, the first term in the left-hand-side (L.H.S) is the H_2O mass accumulation in the element of the flow system, the second term is H_2O mass fluxes into or out of the element, and the third term is H_2O mass exchange between slit pore and clay pore. The H_2O mass fluxes include advective and diffusive fluxes, governed by Darcy's law and Fick's law. We infer no H_2O mass accumulation in organic pores, which have oil-wet pore surfaces. The right-hand-side (R.H.S) is the source/sink term. The subscript *A* stands for aqueous phase and *G* for gaseous phase.

Mass exchange of component κ between the slit pore and the clay pore is described by a coupling term, $w_{A,Ic}^{\kappa}$ which has dimension of (mass/volume)/time that correspond to the resistance time.

H_2O mass exchange between the slit pore and the clay pore is defined as:

$$w_{A,Ic}^{H_2O} = \ell_{Ic}\left\{x_A^{H_2O}\rho_A\frac{k_m}{\mu_A}\left[P_{A,I} - P_{A,c}\right] - x_A^{H_2O}\lambda_t(\rho_A)^2\left[x_{A,I}^{Salt} - x_{A,c}^{Salt}\right] + \rho_A\phi_c\tau_A D_{o,A}^{H_2O}\left[x_{A,I}^{H_2O} - x_{A,c}^{H_2O}\right]\right\} \quad (62)$$

Here, ℓ_{IC} is the shape factor [1/m^2]; $P_{A,I}$ is the pore pressure inside slit pore [Pa]; $P_{A,c}$ is the clay-pore pressure [Pa]; $x_{A,I}^{Salt}$ and $x_{A,I}^{H_2O}$ are the salt and H_2O mass fraction in slit pore; $x_{A,c}^{Salt}$ and $x_{A,c}^{H_2O}$ are the salt and H_2O mass fraction in clay pore. The coefficient λ_t is a coefficient which include two transport coefficients, the permeability of the clay-membrane (k_m) and the clay membrane efficiency ($\mathcal{R}$) and defined as in Eq. 42.

This H_2O mass exchange between the slit pore and the clay pore is formulated similarly the way mass flux through clays in Chapter 3 which include three terms. The first term is H_2O Darcy's-like mass flux, the second is H_2O flux due to osmosis and the third is H_2O molecular diffusion flux due to H_2O concentration gradient.

The H_2O advective mass flux in aqueous and gaseous phase can be written as:

$$\mathbf{F}_A^{H_2O}\big|_{\text{adv}} = -x_A^{H_2O}\rho_A\left\{\frac{\mathbf{k}k_{rA}}{\mu_A}(\nabla P_A - \rho_A\mathbf{g})\right\} \qquad (\ 63\ )$$

$$\mathbf{F}_G^{H_2O}\big|_{\text{adv}} = -x_G^{H_2O}\rho_G\left\{\frac{\mathbf{k}k_{rG}}{\mu_G}(\nabla P_G - \rho_A\mathbf{g})\right\} \qquad (\ 64\ )$$

where, $\mathbf{k}$ is the permeability of the slit-pore [m^2]; k_{rA} and k_{rG} are the relative permeability of aqueous- and gas-phase; and $\mathbf{g}$ is the gravitational acceleration vector [m/s^2].

When the two phases, aqueous and gaseous phase coexist in the slit pore, the following relation applied:

$$P_G = P_{cap} + P_A \qquad (\ 65\ )$$

where,

P_{cap} is the capillary pressure, [Pa]

The H_2O diffusive mass flux in aqueous and gaseous phase can be written as:

$$\mathbf{F}_A^{H_2O}\big|_{\text{dif}} = -\rho_A \phi_I S_A \tau_A D_{o,A}^{H_2O} \nabla x_A^{H_2O} \quad (66)$$

$$\mathbf{F}_G^{H_2O}\big|_{\text{dif}} = -\rho_G \phi_I S_G \tau_G D_{o,G}^{H_2O} \nabla x_G^{H_2O} \quad (67)$$

4.1.1.2. CH_4 Mass Balance Equation

Component CH_4 exists in gaseous phase in the organic pores (ϕ_k), the aqueous and gaseous phase in the slit pores (ϕ_I) and in the aqueous phase in clay pores (ϕ_c). The H_2O mass balance equation for two-phase flow can be written as follows:

$$\begin{aligned}\frac{\partial}{\partial t}\{\phi_I(x_A^{CH_4}\rho_A S_A + x_G^{CH_4}\rho_G S_G) + \rho_G \phi_k + M_{CH_4}\varepsilon_{ks}(1-\phi_{tot})C_\mu\} \\ + \nabla.\left\{\mathbf{F}_A^{CH_4}\big|_{\text{adv}} + \mathbf{F}_G^{CH_4}\big|_{\text{adv}} + \mathbf{F}_A^{CH_4}\big|_{\text{dif}} + \mathbf{F}_G^{CH_4}\big|_{\text{dif}}\right\} + w_{A,Ic}^{CH_4} \\ = q^{CH_4}\end{aligned} \quad (68)$$

In the above equation, the first term in the L.H.S is the CH_4 mass accumulation in the slit pore, in the organic pore as free-gas, and as adsorbed gas in the kerogen. The second term is CH_4 mass fluxes into or out of the element, and the third term is CH_4 mass exchange between slit pore and clay pore. The CH_4 mass fluxes include advective and diffusive fluxes, govern by Darcy's law and Fick's law.

The sorbed-gas concentration in the kerogen grain volume (C_μ) is described as follows (Wasaki and Akkutlu, 2015):

$$C_\mu = C_{\mu s}\frac{P}{P + P_L} \quad (69)$$

$$C_{\mu s} = \frac{V_{sL}\rho_{sc,gas}\rho_{grain}}{\varepsilon_{ks}M_{CH_4}} \quad (70)$$

where, V_{sL} is Langmuir volume, sorbed-gas volume per total grain mass (m^3/kg); M_{CH_4} is the molecular weight of CH_4 [kg/mol]; ε_{ks} is the total organic content in terms of organic grain volume per total grain volume [-]; and C_μ is the sorbed-gas concentration in kerogen grain volume [mol/m^3].

CH_4 mass exchange between the slit pore and the clay pore is defined similarly as for H_2O:

$$w_{A,Ic}^{CH_4} = \ell_{Ic}\left\{x_A^{CH_4}\rho_A\frac{k_m}{\mu_A}\left[P_{A,I}-P_{A,c}\right] - x_A^{CH_4}\lambda_t(\rho_A)^2\left[x_{A,I}^{Salt}-x_{A,c}^{Salt}\right] + \rho_A\phi_C\tau_A D_{o,A}^{CH_4}\left[x_{A,I}^{CH_4}-x_{A,c}^{CH_4}\right]\right\} \quad (71)$$

The CH_4 advective mass flux in aqueous and gaseous phase can be written as:

$$\mathbf{F}_A^{CH_4}\big|_{\text{adv}} = -x_A^{CH_4}\rho_A\left\{\frac{\mathbf{k}k_{rA}}{\mu_A}(\nabla P_A - \rho_A\mathbf{g})\right\} \quad (72)$$

$$\mathbf{F}_G^{CH_4}\big|_{\text{adv}} = -x_G^{CH_4}\rho_G\left\{\frac{\mathbf{k}k_{rG}}{\mu_G}(\nabla P_G - \rho_A\mathbf{g})\right\} \quad (73)$$

The CH_4 diffusive mass flux in aqueous and gaseous phase can be written as:

$$\mathbf{F}_A^{CH_4}\big|_{\text{dif}} = -\rho_A\phi_I S_A\tau_A D_{o,A}^{CH_4}\nabla x_A^{CH_4} \quad (74)$$

$$\mathbf{F}_G^{CH_4}\big|_{\text{dif}} = -\rho_G\phi_I S_G\tau_G D_{o,G}^{CH_4}\nabla x_G^{CH_4} - M^{CH_4}D_s\nabla C_\mu \quad (75)$$

4.1.1.3. Salt Mass Balance Equation

Component salt exists in the aqueous phase in the slit pores (ϕ_I) and in the clay pores (ϕ_c). The salt mass balance equation for two-phase flow can be written as follows:

$$\frac{\partial}{\partial t}\left(x_A^{Salt}\rho_A S_A \phi_I\right) + \nabla.\left\{\mathbf{F}_A^{Salt}\big|_{\text{adv}} + \mathbf{F}_A^{Salt}\big|_{\text{dif}}\right\} + w_{A,Ic}^{Salt} = q^{Salt} \qquad (\ 76\ )$$

The first term in the L.H.S in the salt mass balance equation is the salt mass accumulation in the slit-pore, the second term is salt mass fluxes into or out of the element, and the third term is salt mass exchange between slit-pore and clay-pore. The salt mass fluxes include advective and molecular diffusion fluxes, govern by Darcy's law and Fick's law.

The salt mass exchange between slit pore and clay pore is defined as:

$$w_{A,Ic}^{Salt} = \ell_{IC}\left\{(1-\mathcal{R})\rho_A x_A^{Salt}\left[\frac{k_m}{\mu_A}\left(P_{A,I}-P_{A,C}\right) - \lambda_t \rho_A\left(x_{A,I}^{Salt} - x_{A,c}^{Salt}\right)\right] + (1-\mathcal{R})\rho_A \phi_c \tau_A D_{o,A}^{Salt}\left(x_{A,I}^{Salt} - x_{A,c}^{Salt}\right)\right\} \qquad (\ 77\ )$$

This salt mass exchange between slit pore and clay pore is formulated similarly the way salt mass flux through clays in Chapter 3 which include two terms. The first term is salt flux associated with Darcy's flux and osmosis flux that salt may filtrate or reflect through clay membrane depending on the efficiency of the clay membrane. The second term is diffusive salt flux that also may filtrate or reflect through clay as controlled by the clay membrane efficiency.

The salt advective mass flux can be written as:

$$\mathbf{F}_A^{Salt}\big|_{\text{adv}} = -x_A^{Salt}\rho_A\left\{\frac{\mathbf{k}k_{rA}}{\mu_A}\left(\nabla P_A - \rho_A \mathbf{g}\right)\right\} \qquad (\ 78\ )$$

The salt diffusive mass flux can be written as:

$$\mathbf{F}_A^{Salt}\big|_{\text{dif}} = -\rho_A \phi_I S_A \tau_A D_{o,A}^{Salt} \nabla x_A^{Salt} \quad (79)$$

4.1.2. Constitutive, Equilibrium Restriction and Constraint Equations

Similar to the simulator described in Chapter 3, the thermophysical properties of water including density, viscosity, specific enthalpy, and thermal conductivity are calculated using the IAWPS formulation, 1997 (Wagner et al., 2000). The density of CH_4 is calculated using Peng and Robinson (1976) equation of state. The viscosity of gas-phase is calculated using gas viscosity correlation (Sun and Mohanty, 2005).

The constraints are applied as follows:

$$x_A^{H_2O} + x_A^{Salt} + x_A^{CH_4} = 1 \quad (80)$$

$$x_G^{H_2O} + x_G^{CH_4} = 1 \quad (81)$$

$$x_{A,Clay}^{H_2O} + x_{A,Clay}^{Salt} + x_{A,Clay}^{CH_4} = 1 \quad (82)$$

Henry's constant for methane can be calculated as follows (Sun and Mohanty, 2005):

$$\ln H^{CH_4} = 1.0\text{E}3 \left(5.1345 + \frac{7837.0}{T} - \frac{1.509\text{E}6}{T^2} + \frac{2.06\text{E}7}{T^3}\right) \quad (83)$$

The molar fraction of CH_4 in aqueous phase ($y_A^{CH_4}$) is calculated as follow

$$y_A^{CH_4} = \frac{P^{CH_4}}{H^{CH_4}} \quad (84)$$

The molar fraction of CH_4 in gaseous phase ($y_G^{CH_4}$) is calculated as follow:

$$y_G^{CH_4} = \frac{P^{CH_4}}{P_G} \quad (85)$$

$$P_G = P^{CH_4} + P^{H_2O} \quad (86)$$

where,

H^{CH_4} is Henry's constant for CH_4, [Pa]

P^{CH_4} is CH_4 partial pressure, [Pa]

The density of aqueous phase in slit-pore and in clay-pore is calculated as follows:

$$\rho_A = x_A^{H_2O}\rho_A^{H_2O} + x_A^{Salt}\rho^{salt} + x_A^{CH_4}\rho^{CH_4} \quad (87)$$

where,

$\rho_A^{H_2O}$ is the density of water in the aqueous phase, [kg/m^3]

ρ^{salt} is the density of salt, [kg/m^3]

ρ^{CH_4} is the density of CH_4 calculated as the function of CH_4 partial pressure, [kg/m3]

The density of gaseous phase is calculated as follows:

$$\rho_G = x_G^{H_2O}\rho_G^{H_2O} + x_G^{CH_4}\rho^{CH_4} \quad (88)$$

where,

$\rho_G^{H_2O}$ is the density of H_2O in vapor phase calculated as the function of H_2O partial pressure, [kg/m3]

The normalized water saturation (S_w^*) to calculate the imbibition relative permeability is defined as follows (Li and Horne, 2006):

$$S_w^* = \frac{S_w - S_{wr}}{1 - S_{wr} - S_{gr}} \quad (89)$$

The relative permeability to water- and to gas-phase can be calculated as (Corey, 1954):

$$K_{rw} = (S_w^*)^4 \quad (90)$$

$$K_{rg} = (1 - S_w^*)^2[1 - (S_w^*)^2] \quad (91)$$

To accommodate effect of damage in the invaded zone, capillary pressure is combined with the J-function (Leverett, 1941) and calculated as follows (Gdanski et al., 2009):

$$P_{cap} = \frac{\sigma_{IFT}}{a_2 S_w{}^{a_1}} \left(\frac{\phi}{k}\right)^{a_3} \quad (92)$$

where,

P_{cap}	is capillary pressure, [psi]
σ_{IFT}	is interfacial tension, [dyne/cm]
a_1, a_2 and a_3	are adjustable constants

Using the above equation, effect of damage to capillary pressure can be demonstrated as porosity, permeability and interfacial tension are altered. However, in this simulation, all parameters are kept constant to focus the observation to the clay-swelling effect.

4.2. Numerical Solution using Integral Finite Difference Method

4.2.1. Discretization of Mass and Energy Balance Equations

The mass and energy balance equations were discretized in the same manner as described in Chapter 3. These equations were discretized in space using the integral finite difference method and time was discretized as a first-order backward finite difference. All the unknown thermodynamic parameters in the flux and source/sink terms were evaluated at the new time level.

After discretization, the mass balance equations became a set of residual equations in the form of Eq. 55. In this simulator, we include six residual equations for components H_2O, salt and CH_4 in slit-pore, H_2O and salt in clay-pore and temperature to be solved for each volume element. The unknowns are the $N_E * N_\kappa$ independent primary variables (X_i, for $i = 1, \dots, N_E * N_\kappa$) where N_E is the number of elements and N_κ is the number of equations for each element.

4.2.2. Primary Variables

The simulator developed in this part includes four thermophysical state which are aqueous phase, gaseous phase and two-phases in matrix domain which has three pores, and two-phases in fracture domain with single pore. Primary variable were chosen to be able describing a system involving mass exchange by osmosis mechanism between pores within the element. Since we had six residuals equations to be solved, we need to choose six primary variables as the unknowns. Other unknown variables were solved by the use of constitutive, equilibrium restriction and constraint equations.

The details of the primary variables for each domain and state is shown in Table 4, where:

$y_A^{H_2O}, y_A^{CH_4}$ and y_A^{Salt}	are the molar fraction of H_2O, CH_4 and salt in the aqueous phase
$y_G^{H_2O}$ and $y_G^{CH_4}$	are the molar fraction of H_2O and CH_4 in the gaseous phase
$y_{A,Clay}^{H_2O}, y_{A,Clay}^{CH_4}$ and $y_{A,Clay}^{Salt}$	are the molar fraction of H_2O, CH_4 and salt in the clay pore

Table 4 – Domain, state and primary variables for two-phase flow in fracture and shale gas reservoir with multiporosity

Domain	State	Primary Variables (X_i)
Shale Matrix	Single phase, aqueous	$P, y_A^{CH_4}, y_A^{Salt}, y_{A,Clay}^{Salt}, P_{clay}, T$
	Single phase, gaseous	$P, y_G^{CH_4}, y_{A,Clay}^{Salt}, y_{A,Clay}^{H_2O}, P_{clay}, T$
	Two-phase, aqueous and gaseous	$P, S_G, y_A^{Salt}, y_{A,Clay}^{Salt}, P_{clay}, T$
Fracture	Two-phase, aqueous and gaseous	$P, S_G, y_A^{H_2O}, y_A^{Salt}, y_G^{H_2O}, T$

4.2.3. The Newton/Raphson Iteration

The residual equations were solved using Newton/Raphson iteration method in the same manner as described in Chapter 3. I constructed Eq. 57, the Jacobian matrix equations, from the residual equations by differentiating the residual equations in terms of primary variables (X_i). Again, the dimension of the Jacobian matrix is $(N_E * N_\kappa)$*$(N_E * N_\kappa)$ and the unknowns are the $N_E * N_\kappa$ primary variables. Solution of the Jacobian matrix equations proceeded in an iterative manner until the residuals ($R_n^{\kappa,k+1}$) were reduced below a preset convergence tolerance that describes an acceptable (and very low) mass and/or energy balance error.

4.3. Description of Geometry and Parameters in Simulation Case Studies

Simulation of five shut-in cases was conducted to observe the effect of salt concentration, salt type, initial water saturation and clay-membrane efficiency to permeability evolution, the detail of shut-in cases are shown in Table 5. Simulation of production cases after shut-in was also conducted to observe the impact of permeability impairment during shut-in to well production performance.

The specific problem to which the numerical simulation was applied assumes a quarter of a single vertical hydraulic fracture perpendicular to a horizontal well and the adjacent

Table 5 – Shut-in simulation cases

Case	Initial Sw in Slit-Pore and Clay-Pore	Salt Type	Salt Mass Fraction in Fracturing Fluid	Salt Mass Fraction in Aqueous Phase in Shale
Case 1	0.2	NaCl	0.0001	0.05
Case 2	0.2	NaCl	0.02	0.05
Case 3	0.2	NaCl	0.02	0.15
Case 4	0.2	KCl	0.02	0.15
Case 5	0.05	NaCl	0.0001	0.05

stimulated shale gas volume as shown in Fig. 12. The geometry of the problem in *xyz* directions is 5x100x10m, which is divided into 500 gridblocks in the *x*-direction. We set the first gridblock on the left as the hydraulic fracture element. Here, we were interested in understanding co-existence of imbibition and osmosis mechanisms and their impact to the shale formation permeability. We therefore decided to simplify the geometry to one-dimension (ID).

Varying initial salt concentration in the aqueous phase between the hydraulic fracture element and the shale matrix element was applied to imitate condition in the hydraulic-fracture and the shale matrix. Constant pressure of 3,000 psi and water saturation of 100% was applied in the hydraulic-fracture element, which was equal to the initial pressure in the shale matrix elements to simulate shut-in and continuous shale-water interaction after hydraulic-fracturing operation. In all numerical simulations, the initial water saturation, pressure and temperature were kept the same as shown in Table 6 unless pointed to be varied. Initially, water saturation in the slit pores were assumed to be at irreducible water saturation of 20% with maximum capillary pressure values, except for the fifth case when the initial water saturation was a sub-irreducible water saturation. For each case, clay pores and the slit pores contain equal salt concentration. Different clay-membrane efficiencies were applied for each simulation case: 0.01; 0.1; 0.25; 0.5; 0.75 and 1.00. Other reservoir properties such as permeability and porosity are also given in Table 6.

Table 6 – Shale gas properties and parameters used in simulation

Parameter		Value	Unit
Initial slit-shaped pore pressure		3000	psi
Initial clay-pore pressure		3000	psi
Initial temperature		60	^{o}C
Porosity:	ϕ_k (organic)	2%	
	ϕ_I (inorganic)	6%	
	ϕ_C (clay)	10%	
Initial water saturation:	in ϕ_k	0%	
	in ϕ_I	20%	
	in ϕ_C	100%	
Sorption Properties			
Grain Density		2650	kg/m^3
Langmuir volume (V_{sL})		5.66E-03	m^3/kg
Langmuir pressure (P_L)		500	psi
Total organic grain volume / total grain volume (Ɛks)		0.02	
Diffusion Coefficient			
Surface diffusion coefficient		1.00E-09	m^2/s
Diffusion coefficient of CH_4 in aqueous phase		1.72E-09	m^2/s
Diffusion coefficient of salt in aqueous phase		2.60E-13	m^2/s
Diffusion coefficient of CH_4 in gas phase		1.00E-09	m^2/s
Osmotic Model Parameters			
Clay-membrane permeability (k_m)		1.00E+00	nD
Shape factor		1.00E-05	
Clay-membrane efficiency		0.01 - 1.0	
Salt type		NaCl, KCl	
Gangi Model Parameters			
k_0	1.00E-02	md	
m	0.5		
P_1	26000	psi	
P_{conf}	15000	psi	
χ	0.5		
Capillary Pressure Parameters			
a1, a2, a3	1.86, 6.42, 0.1		
σ_{IFT}	72	dyne/cm	
Relative Permeability Parameters			
S_{wirr}	0.2		
S_{gr}	0.05		

4.4. Simulation Results and Analysis

4.4.1. Effect of Clay Membrane Efficiency on Permeability during Shut-in Period

Although initially the pressure is uniform in the system, due to spontaneous imbibition mechanism caused by high capillary pressure in shale matrix, there should exist a net water influx from the hydraulic fracture element containing 100% aqueous phase into the adjacent shale element that has 20% water saturation. Simulation results show that the computed pressure and water saturation values increase with time and that a pressure wave and a saturation wave propagate from the gridblocks adjacent to hydraulic-fracture element, deep into the formation (Fig. 22). In slit pores, the saturation by fracture is significantly increased from the initial value of 20% (Fig. 22b). Indeed, the propagation speeds of the waves are very low, but the increase of pressure and water saturation near the fracture boundary is visible.

The calculated pressure wave propagation velocity during the first day is approximately 2 m/day, and average water invasion velocity is 0.6 m/day (Fig. 22 and Fig. 23). Pressure velocity is faster than water invasion velocity. However, these velocities are decreasing

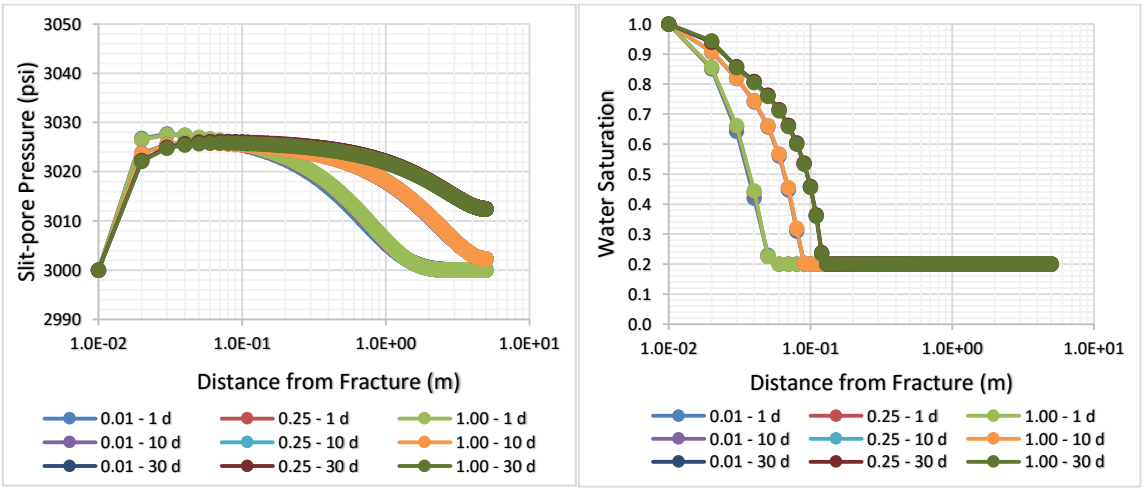

(a) **(b)**

Fig. 22 - Simulation results of Case 1. (a) slit-pore pressure; (b) water saturation in slit pores at time 1, 10, and 30 days using clay membrane efficiency of 0.01, 0.25 and 1.00.

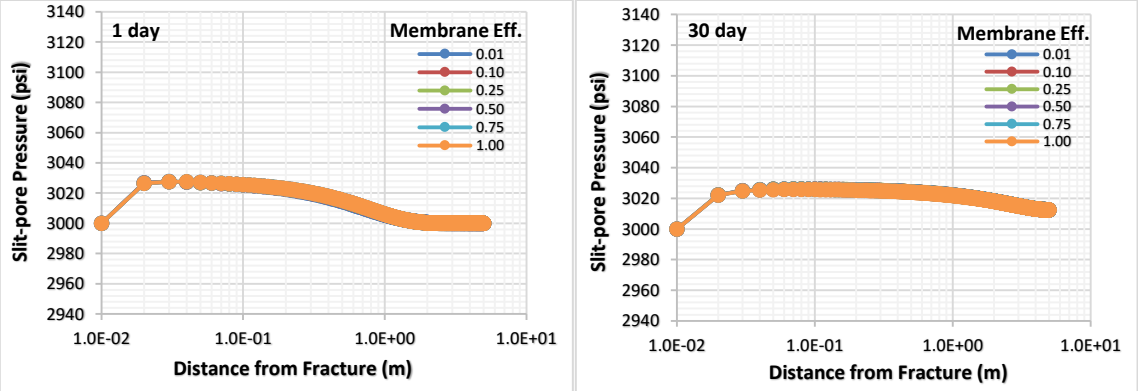

Fig. 23 - Simulation results of Case 1: slit-pore pressure at time 1 and 30 days using clay membrane efficiency of 0.01, 0.1, 0.25, 0.5, 0.75 and 1.00. This plots show that slit-pore pressure is not affected significantly by clay membrane efficiency

and, after the pressure in hydraulic-fracture element is equalized with the fluid pressure in slit pores of the adjacent shale element, the water influx decreases, hence, the wave propagates slower. After 30 days of shut-in, water invades to approximately 11 cm into the shale formation. Simulation results also show that the estimated pressure and water saturation values and their dynamics are mostly independent of clay membrane efficiency since the waves have the same amplitudes and reach nearly the same locations in the formation in the presence of different clay-membrane efficiency.

In clay pores, on the other hand, the predicted pressure is sensitive to the membrane efficiency (Fig. 24). Clay pore pressure increases as the membrane efficiency is increased such that highest clay-pore pressure is reached when the membrane is ideal, i.e., its efficiency is equal to 1.0. Clay-pore pressure keeps increasing in time and propagates deep into the formation and reaches a distance of about 11 cm away from the fracture element during the shut-in time. These increases are related to the fresh water movement into the formation (Fig. 22b).

Fig. 25 shows the computed pressure difference between the slit pores and the clay pores and Fig. 26 shows the evolution permeability reduction in slit pores for varied clay-

membrane efficiency values caused by pressure increase inside clay pores. Initially, as pressure and fresh water saturation waves are propagating in the formation through the slit pore network, the reduction in slit pore or "formation" permeability near the hydraulic-fracture is relatively small because the clay pore and the slit pore pressures counter-balance. Fluid exchange back and forth between the two pore networks due to local variations in pore pressure and salt concentration can be observed as the system went through the transient.

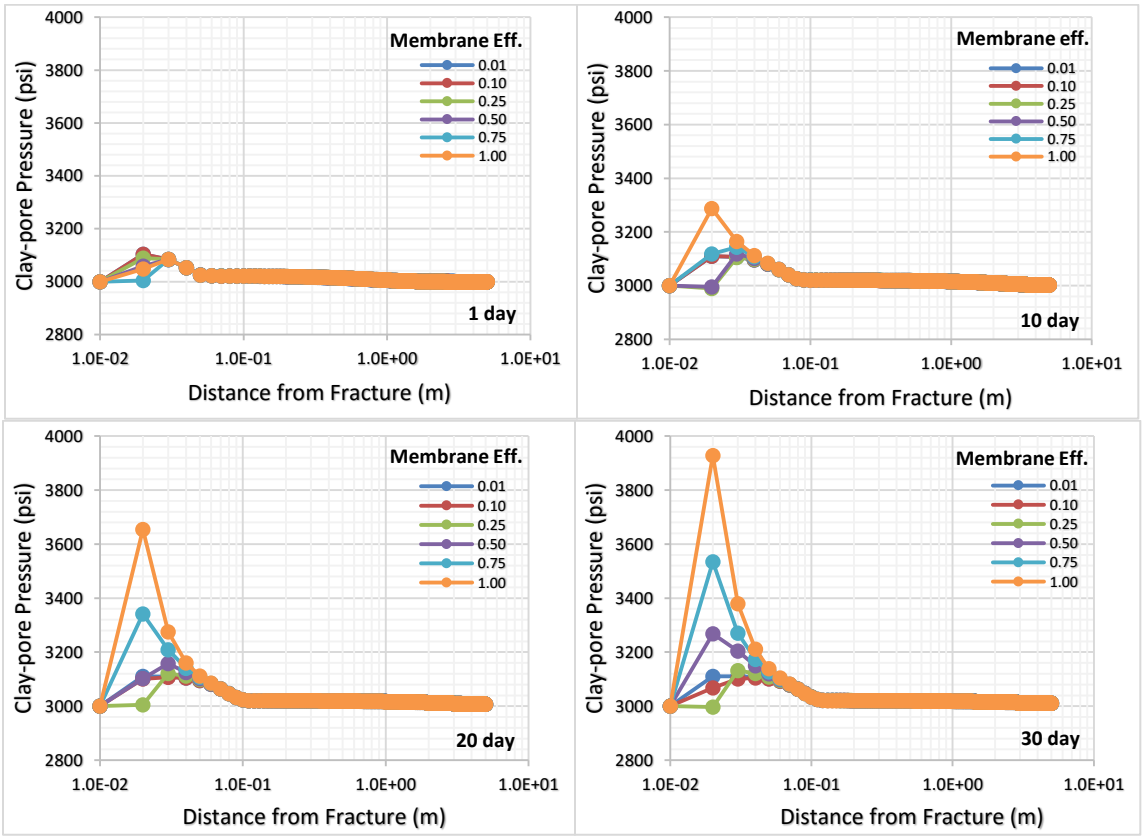

Fig. 24 - Simulation results of Case 1: clay pore pressure at time 1, 10, 20 and 30 days with varied clay-membrane efficiency of 0.01, 0.1, 0.25, 0.5, 0.75 and 1.00. These plots show impact of clay membrane efficiency values to clay-pore pressure, higher efficiency resulting higher clay-pore pressure. These plots also show that clay-pore pressure is increasing with time at elements by fracture.

In clay-pores, on the other hand, the predicted pressure is sensitive to the membrane efficiency (Fig. 24). Clay pore pressure increases as the membrane efficiency is increased such that highest clay-pore pressure is reached when the membrane is ideal, i.e., its efficiency is equal to 1.0. Clay-pore pressure keeps increasing in time and propagates deep into the formation and finally reach a distance of about 11 cm away from the fracture element at the end of the shut-in time. These increases are related to the fresh water movement into the formation (Fig. 22b).

Fig. 25 shows the computed pressure difference between the slit pores and the clay pores and Fig. 26 shows permeability reduction evolution in slit pores for varied clay-membrane

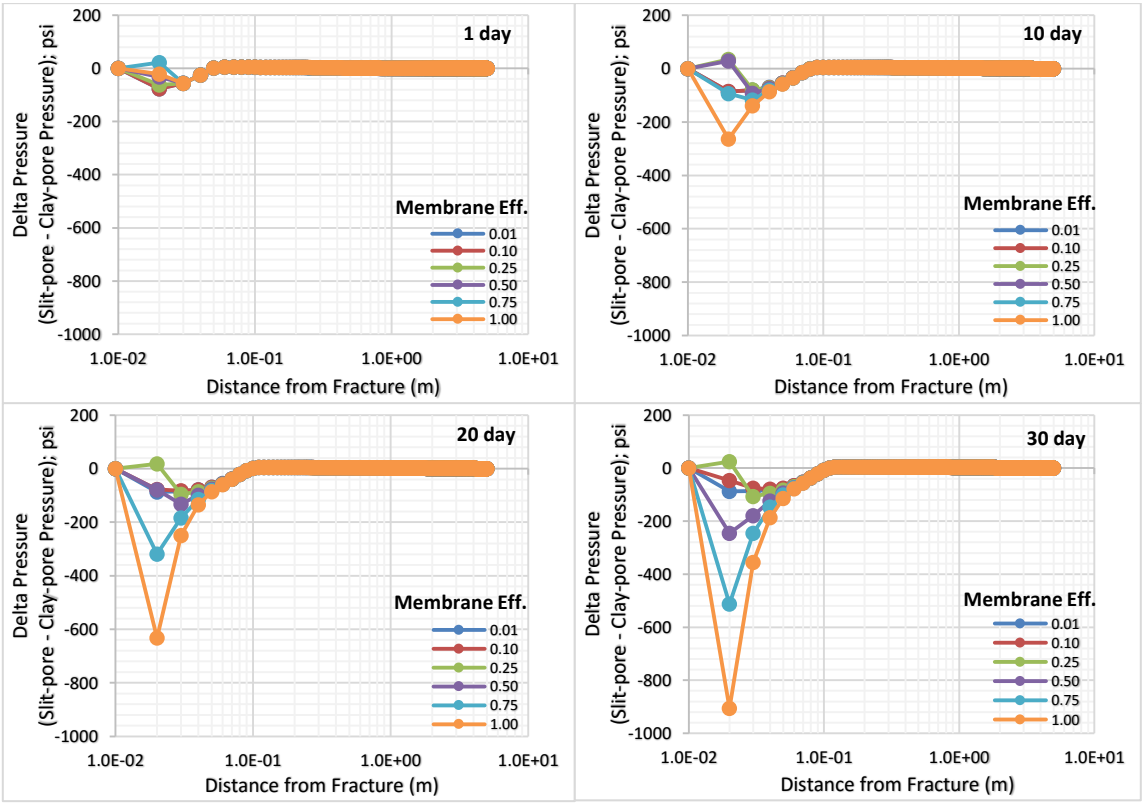

Fig. 25 - Simulation results of Case 1: pressure difference between slit-shaped and clay pores at time 1, 10, 20 and 30 days with varied clay-membrane efficiency of 0.01, 0.1, 0.25, 0.5, 0.75 and 1.00. These plots show that pressure buildup within clay-pore is affected predominantly by clay-membrane and osmosis.

efficiency values caused by pressure increase inside clay pores. Initially, as pressure and fresh water saturation waves are propagating in the formation through the slit pore network, the reduction in slit pore or "formation" permeability near the hydraulic-fracture is relatively small because the clay pore and the slit pore pressures counter-balance. Fluid exchange back and forth between the two pore networks due to local variations in pore pressure and salt concentration can be observed as the system went through the transient effects. At a certain time, however, when pressure in the slit pores near hydraulic-fracture elements has reached equalization with capillary and saturation effects, no significant water can move further into the formation. This is when osmosis takes place more dominantly and pressure begins to build up in the clay pores. When clay-membrane efficiency is low, say equal to 0.01, the buildup pressure in the clay pores is about 100 psi

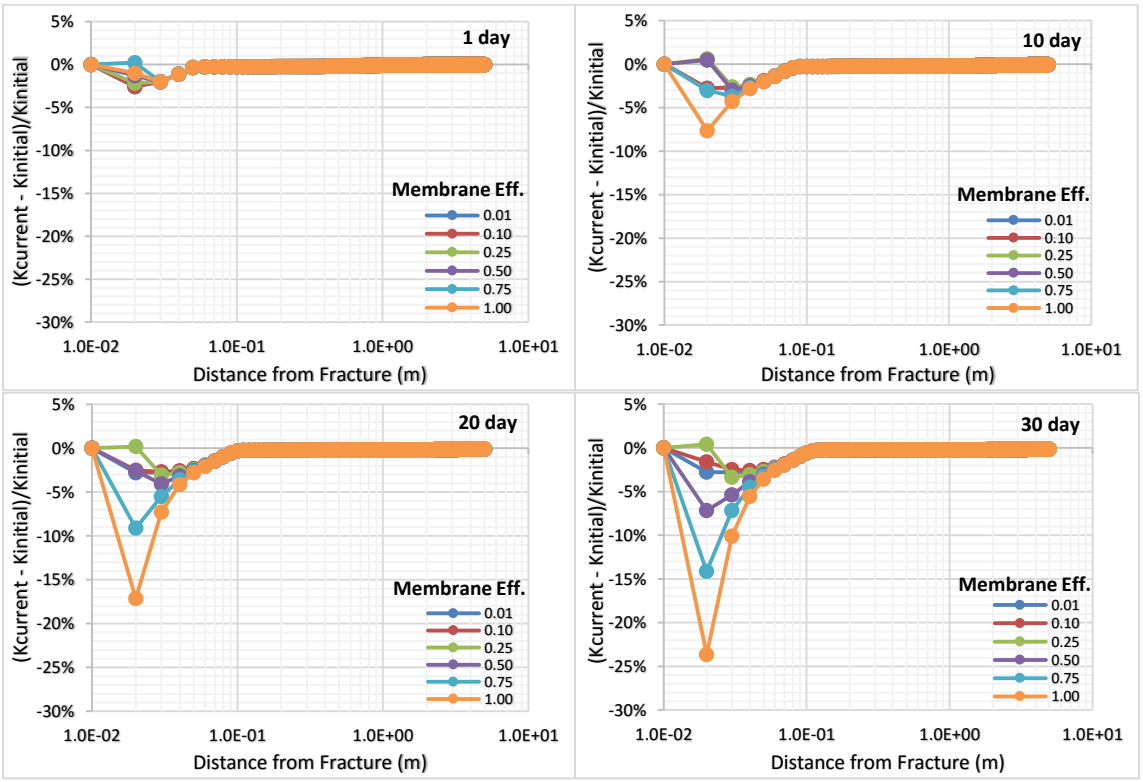

Fig. 26 - Simulation results of Case 1: permeability reduction in slit-pore at time 1, 10, 20 and 30 days with varied clay membrane efficiency of 0.01, 0.1, 0.25, 0.5, 0.75 and 1.00.

higher than slit pore pressures. This leads to a permeability reduction of about 3 – 4%. While assuming an ideal membrane, the buildup pressure in the clay-pores can be as high as 900 psi, which causes a permeability reduction up to 24% in 30 days.

4.4.2. Effect of Salt Concentration Difference on Permeability during Shut-in Period

Simulation results of Cases 1, 2, 3 and 4 are shown in Fig. 27. Formation permeability reduction occurs in all cases with different magnitudes, which indicates dependence on

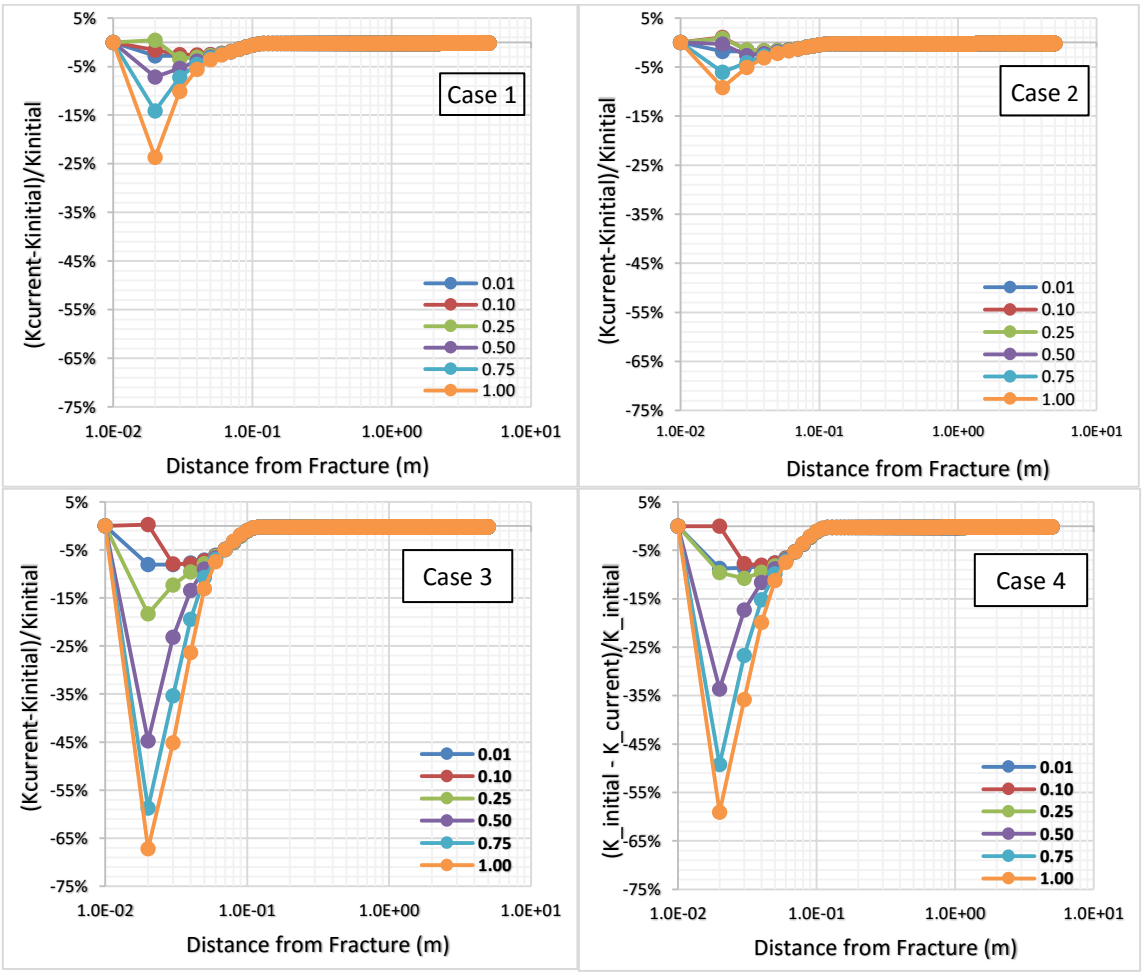

Fig. 27 - Comparison of permeability reduction of slit-shaped pores of all simulation cases at time 30 days. Different colors are indicating different clay membrane efficiency (0.01; 0.1; 0.25; 0.5; 0.75 and 1.0).

the salt concentration differences between the fresh water in hydraulic-fracture and formation water, and on the salt type and the clay-membrane efficiency. Comparing Cases 1 and 2, both of which has a NaCl mass fraction of 0.05 in the formation water, we observe a higher permeability reduction occurring when the fracture is filled with nearly fresh water, compared to the case when the NaCl mass fraction is 0.02. Comparing Case 2 and 3, both of which has hydraulic-fracture containing water with 2% NaCl, the higher permeability reduction is occurred when salt concentration in the aqueous-phase in the formation is higher. Comparing Case 3 and 4, when different salts are dissolved in the aqueous phase, lower permeability reduction is occurred when KCl is the salt dissolved in water.

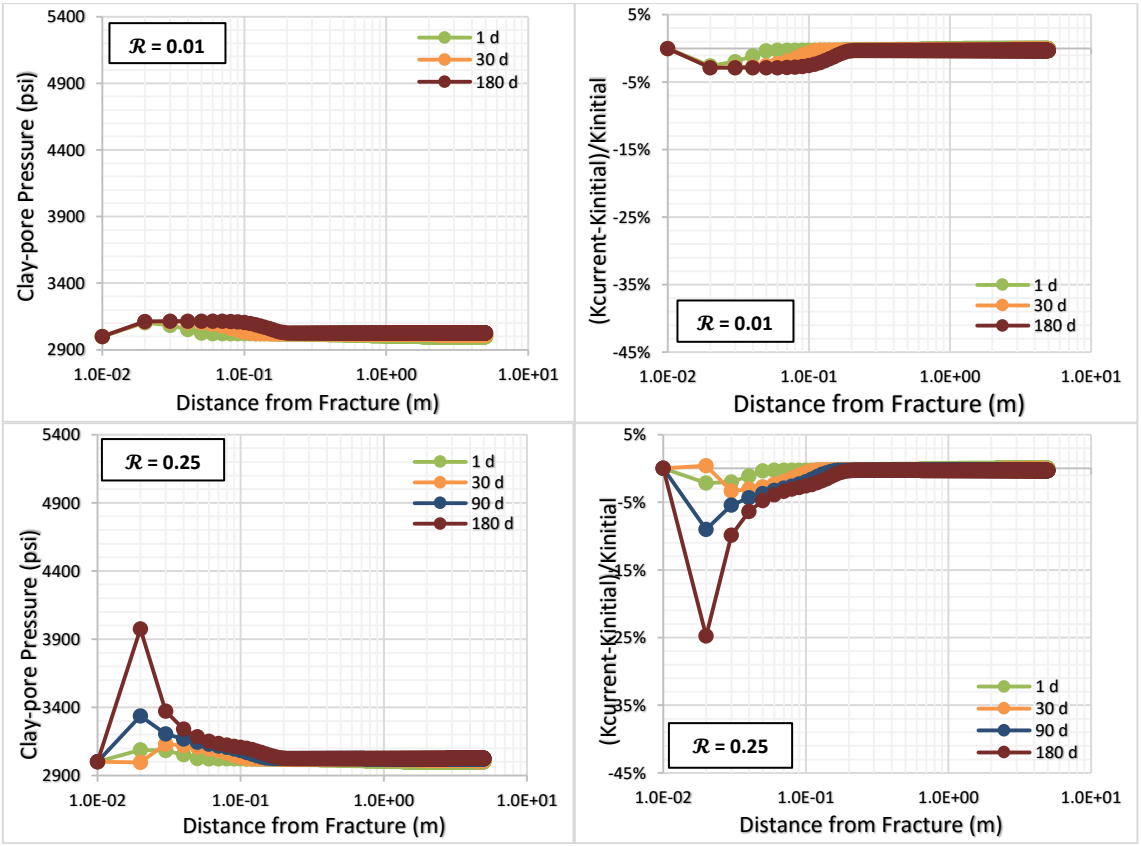

Fig. 28 - Effect of shut-in time to clay-pore pressure increase and the permeability reduction in Case 1 for membrane efficiency 0.01 and 0.25.

4.4.3. Effect of Shut-in Time on Permeability

Fig. 28 shows that, during the shut-in, shale-water interaction continues and this causes the region with reduced permeability to expand. This is mostly due to salt concentration difference between the slit pores and clay-pores. Theoretically, osmotic pressure increases until the salt concentration is equal between the two types of pores, if clay acts as an ideal membrane. Clays are leaky membranes, however, and that causes some ions dissolved in water in the clay pores to filtrate through the clays. Consequently, the ideal osmotic value is not reached. The results show that the damage zone can expand further as the clay-water keep interacting. This indicates that early flow-back may be necessary to avoid expansion of clay-water interaction zone that can cause expansion of permeability damage zone, hence shale gas well production performance reduction.

4.4.4. Effect of Initial Water Saturation on Permeability during Shut-in Period

Case 5 considers a shale formation with a sub-irreducible water saturation. Comparing Cases 1 and 5, I notice, when the formation has a saturation below the irreducible water saturation, the permeability reduction occurs more severely during the same duration of shale-water interaction. Water invasion zone for Case 5 is smaller than case 1 (Fig. 29a). This is because as water penetrates into the slit pores, water remains immobile at the leading edge of the of the saturation wave until the saturation in the pores increases and becomes higher than the irreducible water saturation value. This leads to elongated times of water-clay interaction between the slit pores containing fresh fracturing-water and high salinity water in the clay pores. Consequently, the formation experiences higher level of clay-pore pressure (Fig. 29b), and eventually this lead to larger stress on the slit pores and larger permeability reduction (Fig. 29c).

Other set of simulations were conducted using the same parameters as in Case 5 but now the initial water saturation in the slit pores was varied up to 40%. Fig. 30 shows permeability reduction at 30 day shut-in and with a clay-membrane efficiency 1.0. In 30 days, the permeability damage zone has reached to about 10 cm depth in the formation.

We observe that the permeability damage is higher when the initial saturation is below the irreducible water saturation level in between $0.05<S_w<0.25$.

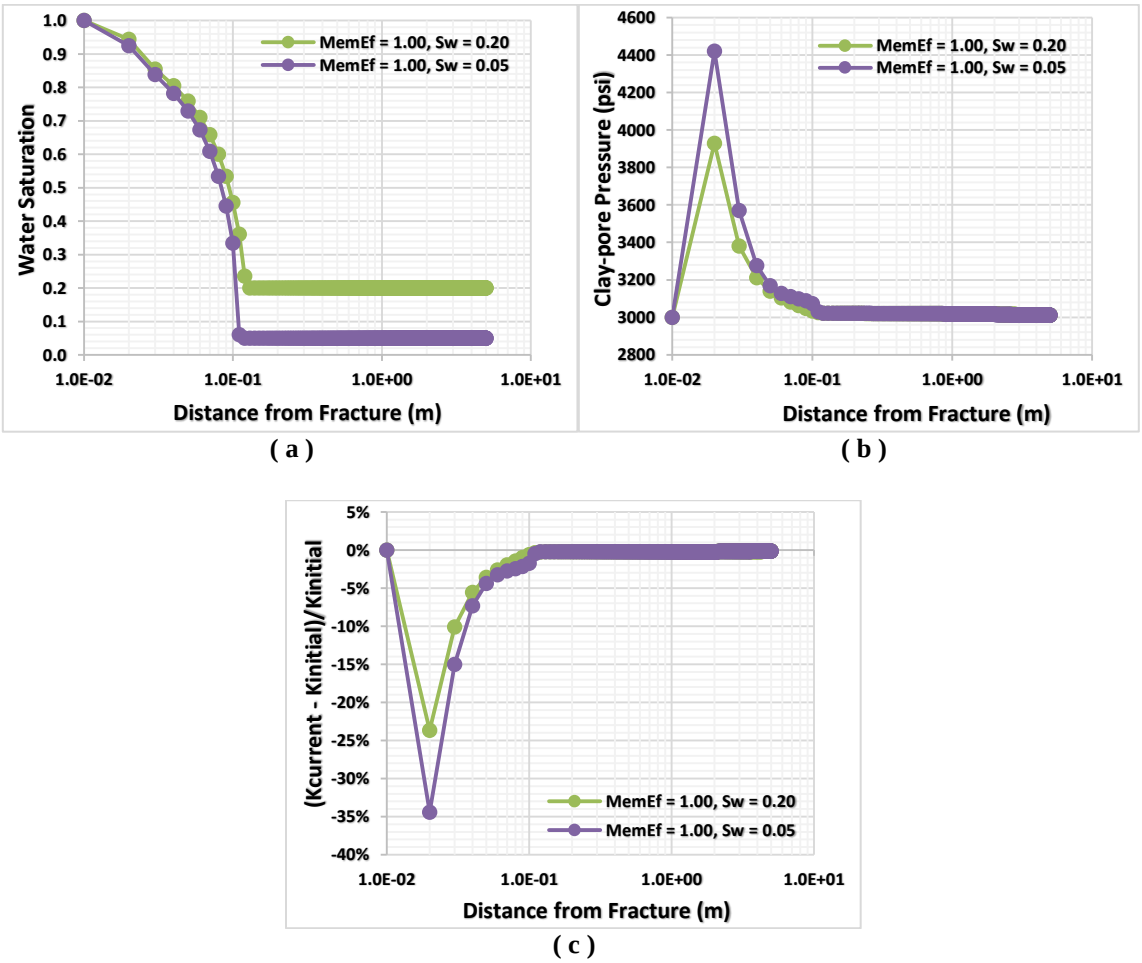

Fig. 29 - Comparison between Case 1 and Case 5 (sub-irreducible water saturation) at 30 day, effect of initial water saturation. (a) Water saturation; (b) clay-pore pressure; (c) permeability reduction.

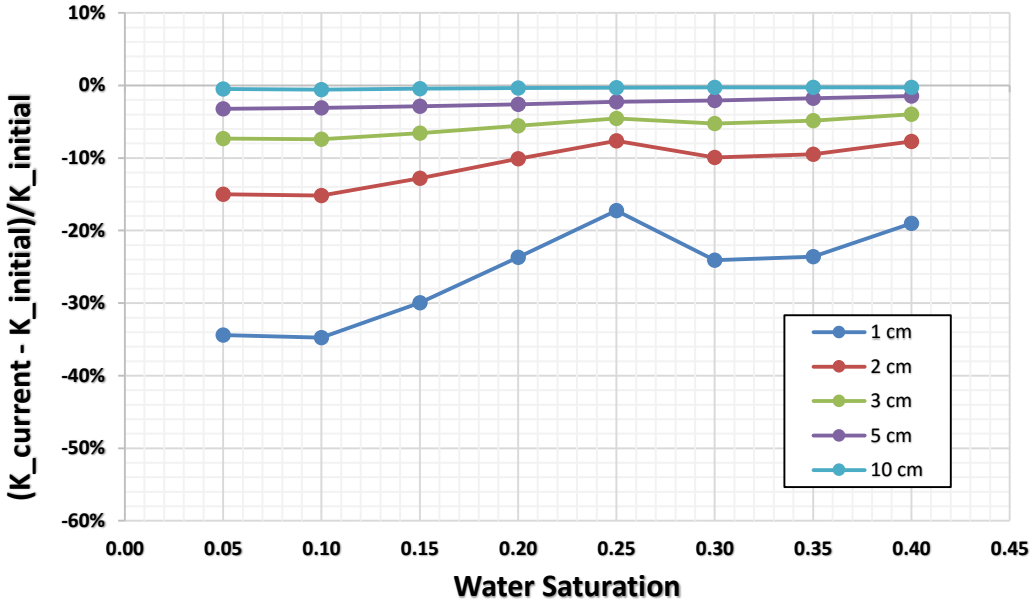

Fig. 30 - Permeability reduction at 30 day for different initial water saturation in model shale at several distances from the hydraulic fracture, using clay-membrane efficiency 1.0.

4.4.5. Production Behavior Following Extended Shut-in Period

In this subsection I investigated the effect of permeability alteration developed during the 30 day shut-in on the gas production performance during the flowback. First, we run simulation cases of production to compare the impact of permeability impairment on the production performance in the presence of irreversible and reversible permeability damage. In the irreversible damage case, we set the permeability damage occurred during the shut-in as permanent such that geomechanics effect to permeability occurs only through the increasing effective stress during production. On the other hand, in the reversible damage case, I did not consider the permeability damage occurred during shut-in as permanent and set the geomechanics effect to permeability fully as it had been described. In the latter case, the permeability was consequently affected by the clay pore pressure as well as slit pore pressure. I also investigated the impact of clay-membrane efficiency and sub-irreducible water saturation.

As expected, when the damage is irreversible, the production performance is much lower than that performance when the damage is reversible (Fig. 31 and Fig. 32). Also, when we used similar clay-membrane efficiency with longer shut-in time, the gas production rate becomes lower, because of higher permeability damage.

In Fig. 33, I compare the effect of varying initial water saturation on the production performance. Here, I observe higher production rate in the case of initial water saturation that is lower than the irreducible water saturation. This case shows the effect of water blocking to the initial gas production rate. Although the case with S_{wi} of 0.05 results in higher permeability damage (Fig. 29c), water saturation is below the irreducible water saturation (Fig. 29a), which immobile, thus, higher initial gas rate.

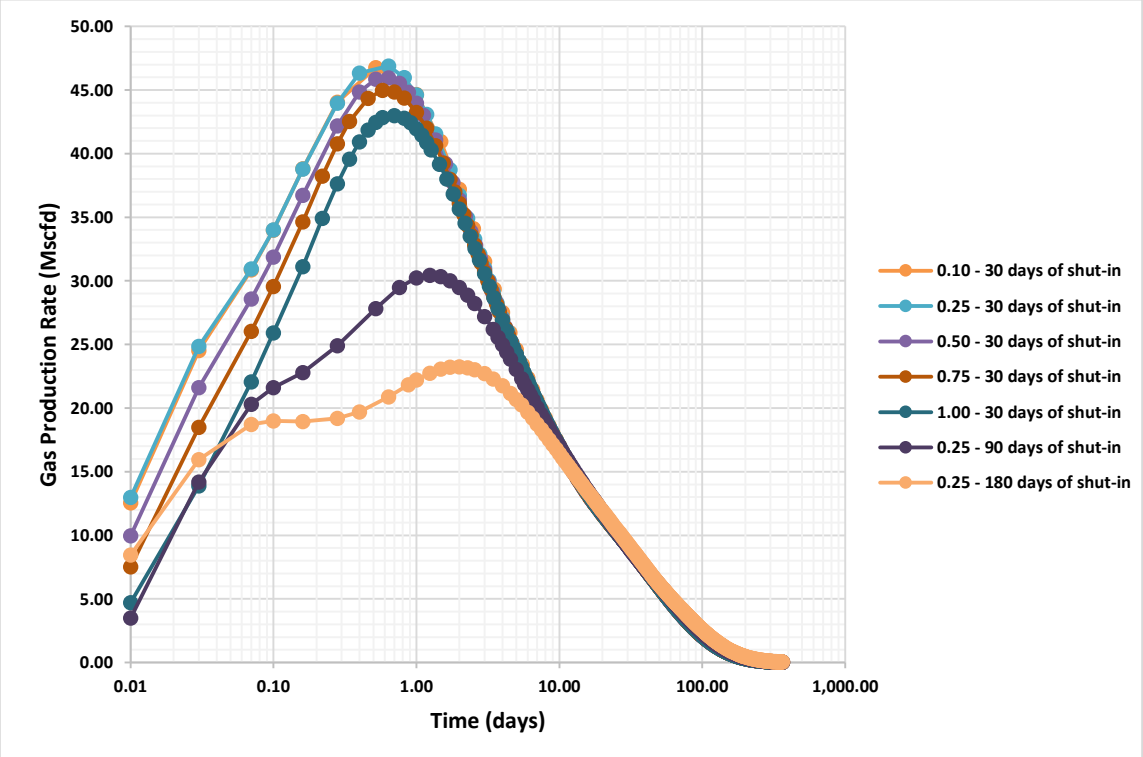

Fig. 31 - 1 year production profile after 30, 90 and 180 days of shut-in time using varied clay-membrane efficiency, reversible case.

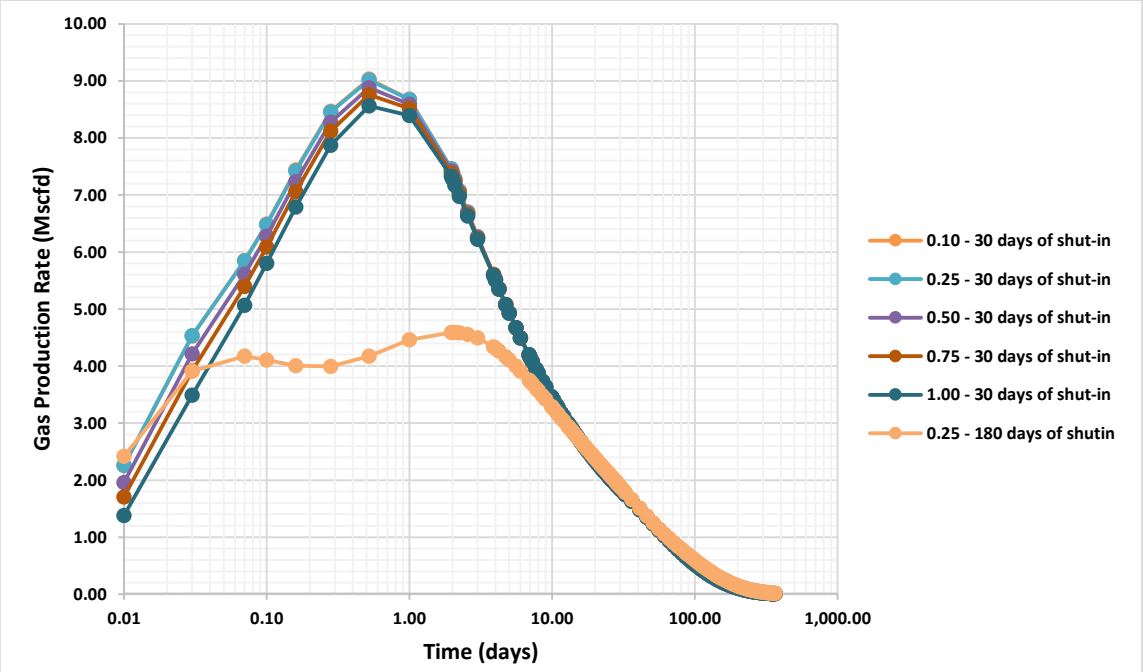

Fig. 32 - 1 year production profile after 30 and 180 days of shut-in time using varied clay-membrane efficiency, irreversible case.

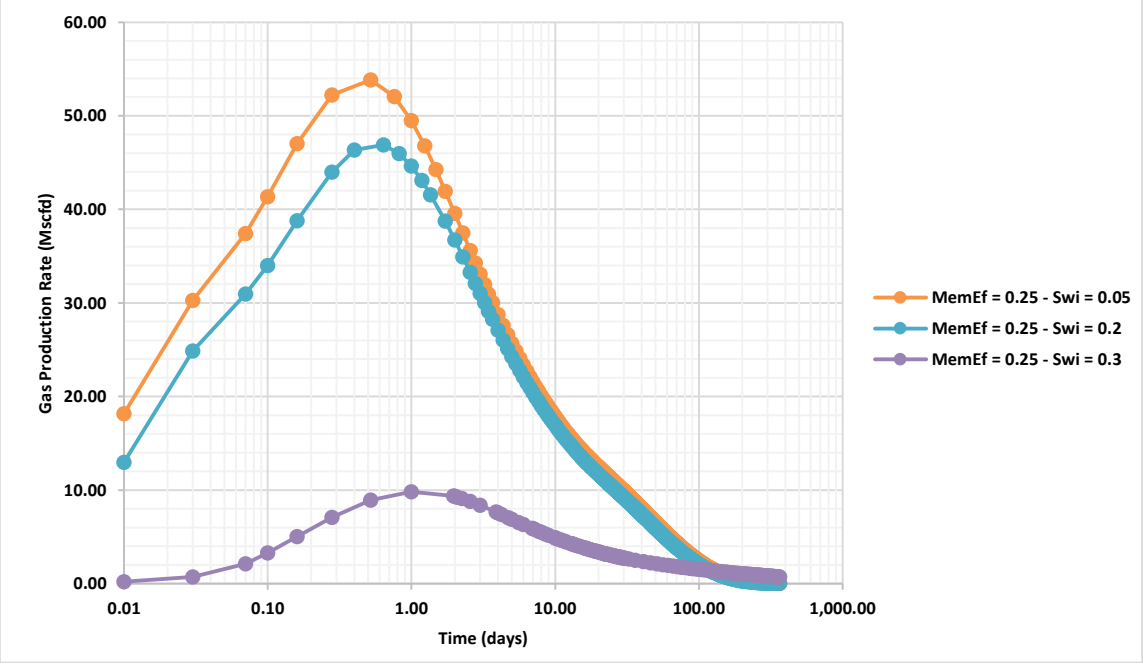

Fig. 33 - 1 year production profile after 30 days of shut-in time using varied initial water saturation (S_{wi}), reversible case.

5. MODELING OF COUPLED TWO-PHASE FLOW AND GEOMECHANICS FOR SHALE GAS FORMATION WITH CLAY-SWELLING EFFECT

In this chapter I discuss numerical modeling of fully-coupled two phase aqueous and gaseous flow and geomechanics for shale gas formations. The objective of this modeling was to clarify imbibition and osmosis mechanisms affecting permeability alteration during shut-in period after hydraulic fracturing and flowback periods under stress. I wanted to understand the stress field, the swelling of the clay and the possibility of inducing micro-fractures due to salt concentration difference between hydraulic fracturing water and formation water by coupling the previous model with geomechanics. The phenomena of clay swelling and microcrack development has been observed in the laboratory, however, how they occur in subsurface under stress in reservoir pressure and temperature conditions is less understood.

Mathematical model for the simulation is an expansion of the model from the previous mathematical model in Chapter 4 adding the momentum balance equation, which will be described in detail below. The mass and heat balance equations and the momentum balance equation were fully coupled and solved simultaneously on a discretized medium in fully implicit manner.

5.1. Mathematical Model

5.1.1. The Governing Geomechanical Equation

The momentum balance equation can be written as follows (Fjar et al., 2008):

$$\nabla . \boldsymbol{\sigma} + \mathbf{F_b} = 0 \qquad (93)$$

where,

$\boldsymbol{\sigma}$ is a stress tensor

$\mathbf{F_b}$ is the body force vector per unit volume, [Pa/m]

The stress strain relations of a nonporous material, Hooke's law, can be expressed in terms of the elastic shear modulus or rigidity (G) and Poisson ratio (v) (Jaeger et al., 2007), in matrix form:

$$\boldsymbol{\varepsilon} = \frac{\boldsymbol{\sigma}}{2G} - \frac{v}{2G(1+v)} tr(\boldsymbol{\sigma})\mathbf{I} \qquad (\ 94\ )$$

The poroelastic constitutive equation relating stress to strain, Hooke's law for porous medium, in term of the effective stress, Biot, 1941(Jaeger et al., 2007):

$$\boldsymbol{\sigma} - \alpha P_p \mathbf{I} = 2G\boldsymbol{\varepsilon} + \lambda tr(\boldsymbol{\varepsilon})\mathbf{I} \qquad (\ 95\ )$$

where

$$tr(\boldsymbol{\varepsilon}) = \varepsilon_{vol} = \varepsilon_b = \varepsilon_{xx} + \varepsilon_{yy} + \varepsilon_{zz} \qquad (\ 96\ )$$

The divergence of the displacement vector ($\nabla . \mathbf{u}$) is the volumetric strain, for very small deformation as being considered here:

$$\nabla . \mathbf{u} = \frac{\partial u_x}{\partial x} + \frac{\partial u_y}{\partial y} + \frac{\partial u_z}{\partial z} = \varepsilon_{xx} + \varepsilon_{yy} + \varepsilon_{zz} = \varepsilon_{vol} \qquad (\ 97\ )$$

By applying the poroelastic constitutive equation relating stress to strain, Hooke's law for porous medium, and substituting the divergence of the displacement vector, and then adding a temperature term, the momentum balance equation can be written as follows (Fakcharoenphol et al., 2013; Winterfeld and Wu, 2016):

$$\alpha \nabla P + 3\beta_t K \nabla T + (G+\lambda)\nabla(\nabla . \mathbf{u}) + G\nabla^2 \mathbf{u} + \mathbf{F_b} = 0 \qquad (\ 98\ )$$

Taking divergence to Eq. 98, yield:

$$\frac{3(1-v)}{1+v}\nabla^2\bar{\sigma} - \frac{2(1-2v)}{1+v}\left\{\alpha\nabla^2 P + 3\beta_t K\nabla^2 T\right\} + \nabla\cdot\mathbf{F_b} = 0 \qquad (\ 99\ )$$

where,

$\bar{\sigma}$ is the mean normal stress, [Pa; psia]

P is the pore pressure, [Pa; psia]

T is the temperature, [°C]

v is Poisson's ratio

α is Biot's coefficient

β_t is linear thermal expansion coefficient, [°C^{-1}]

K is the bulk modulus, [Pa]

The mean normal stress is the average of the normal stress tensor components as follows (Fjar et al., 2008):

$$\bar{\sigma} = \frac{\sigma_{xx} + \sigma_{yy} + \sigma_{zz}}{3} \qquad (\ 100\ )$$

Here, we are assuming an infinitesimal condition.

The details of the derivation of the governing geomechanical equation (Eq. 99) is presented in Appendix A.

The Biot's coefficient (α) is defined as:

$$\alpha = 1 - \frac{K}{K_m} \qquad (\ 101\ )$$

The coefficient values range is $0 \leq \alpha \leq 1$ and most rock have been shown to have $\alpha \leq 1$, indicating that the rock is more sensitive to changes in stress than in pore pressure (Heller

et al., 2014). However, the Biot's coefficient will be near the upper limit, 1.0, for soil-like materials, with K (the bulk modulus) << K_m (the rock matrix/solid modulus) (Rice, 1998).

The governing geomechanical equation that for multi-porosity medium, can be written as follows (Winterfeld and Wu, 2016):

$$\frac{3(1-v)}{1+v}\nabla^2\bar{\sigma} - \frac{2(1-2v)}{1+v}\left[\sum_j\left\{\alpha_j\nabla^2 P_j + 3\beta_t K\omega_j\nabla^2 T_j\right\}\right] + \nabla\cdot\mathbf{F_b} = 0 \qquad (\ 102\ )$$

where subscript *j* refers to multi-porosity continua, which in this work refer to the slit-pore and the clay-pore, while the organic-pore is assumed to reach equilibrium with the slit-pore instantaneously. A weight factor (ω_j) by porous continuum volume fraction can be used if the temperature varies between the multi-porosity continua. However, in this work, it was assumed that temperature in the multi-pore networks are equal.

Volumetric strain (ε_{vol}), as a function of the mean normal stress, can be expressed as follows:

$$\varepsilon_{vol} = \frac{3(1-2v)}{E}\left\{\bar{\sigma} - \sum_j\left[\alpha_j P_j + 3\beta_t K\omega_j(T_j - T_{ref})\right]\right\} \qquad (\ 103\ )$$

where, *E* is Young's modulus, [Pa] and T_{ref} is the reference temperature. The volumetric strain sign is negative for expansion, and positive for compression.

5.1.2. Constitutive Equations, Equilibrium Restriction and Constraint Equations

The equation of state (EOS), permeability, capillary pressure, relative permeability, thermal conductivity, equilibrium restriction and constraint equations were similar to those in previous chapters.

Porosity was varied as function of the volumetric strain as follows (Winterfeld and Wu, 2016):

$$\phi = \phi_{init} + \left(\varepsilon_{vol,init} - \varepsilon_{vol}\right) \quad (104)$$

where subscript *init* refers to initial conditions.

For mass transfer between slit-pores and clay-pores, the clay-membrane efficiency (also called as the reflection coefficient) was estimated as a function of cation exchange capacity (CEC), clay porosity and stress (Marine and Fritz, 1981; Rahman et al., 2005), as follows:

$$\mathcal{R} = 1 - \frac{K_s(R_{ca-w} + 1)}{\left\{\left[R_{ca-w}\left(\frac{C_a}{C_c}\right) + 1\right] + R_{a-mw}\left[R_{ca-m}\left(\frac{C_a}{C_c}\right) + 1\right]\right\}\phi_c} \quad (105)$$

where,

$\mathcal{R}$ is the clay membrane efficiency or reflection coefficient, [-]

K_s is the ratio, $\frac{C_a}{C_s}$

C_a is the anion concentration within the membrane pores, [-]

C_c is the cation concentration within the membrane pores, [-]

C_s is the arithmetic mean solute concentration of the solution pair, [-]

R_{ca-w} is the ratio of f_{cw} to f_{aw}, [-]

R_{ca-m} is the ratio of f_{cm} to f_{am}, [-]

R_{a-mw} is the ratio of f_{am} to f_{aw}, [-]

f_{aw} is the friction coefficient of anion to water, [-]

f_{cw} is the friction coefficient of cation to water, [-]

f_{am} is the friction coefficient of anion to membrane, [-]

f_{cm} is the friction coefficient of cation to membrane, [-]

The anion concentration (C_a) can be calculated by following equation (Rahman et al., 2005):

$$C_a = -\frac{1}{2}C_{EC}\rho_c(1-\phi_c) + \frac{1}{2}\left[{C_{EC}}^2{\rho_c}^2(1-\phi_c)^2 + 4C_s^2\phi_c^2\right]^{\frac{1}{2}} \quad (106)$$

The cation concentration (C_c) can be calculated by following equation (Rahman et al., 2005):

$$C_c = C_a + C_{EC}\rho_c(1-\phi_c) \quad (107)$$

5.2. Numerical Solution using Integral Finite Difference Method

5.2.1. Discretization of Mass and Energy Balance and Geomechanical Equations

The mass and energy balance equations were discretized in the same manner as described in Chapter 3. The mass and energy balance equations were discretized in space using the integral finite difference method and time was discretized as a first-order backward finite difference. All the unknown thermodynamic parameters in the flux and source/sink terms were evaluated at new time level.

After discretization, the mass and energy balance equations became a set of residual equations in the form of Eq. 55. Here, we had six residual equations for component H_2O, salt and CH_4 in slit-pore, H_2O and salt in clay-pore and heat to be solved for each volume element.

The geomechanical equation was discretized using the integral finite-difference method over volume element (V) with outer surface Γ_n. Applying the divergence theorem to the Laplacian operators in Eq. 102 results:

$$\int\left(\frac{3(1-v)}{1+v}\nabla\bar{\sigma} - \frac{2(1-2v)}{1+v}\left[\sum_j\left\{\alpha_j\nabla P_j + 3\beta_t K\omega_j\nabla T_j\right\}\right] + \mathbf{F_b}\right)\bullet\mathbf{n}d\Gamma_n = 0 \quad (108)$$

The governing geomechanical equation can be discretized into this form (Fakcharoenphol et al., 2013):

$$\sum_m \left\{ \frac{3(1-v)}{1+v} \nabla\bar{\sigma} - \frac{2(1-2v)}{1+v} \left[\sum_j \{\alpha_j \nabla P_j + 3\beta_t K \omega_j \nabla T_j\} \right] + \mathbf{F_b} \right\} A_{mn} = 0 \quad (109)$$

The boundary conditions for Eq. 109 are a reference temperature, pressure, and stress at some distance from a given grid block.

The discretized geomechanical equation for shale gas formations containing multi-porosity can be written as:

$$\sum_m \left\{ \frac{3(1-v)}{1+v} \frac{\bar{\sigma}_m - \bar{\sigma}_n}{D_{nm}} - \frac{2(1-2v)}{1+v} \left[\sum_j \left\{ \alpha_1 \frac{P_m - P_n}{D_{nm}} + \alpha_2 \frac{P_{clay,m} - P_{clay,n}}{D_{nm}} + 3\beta_t K \frac{T_m - T_n}{D_{nm}} \right\} \right] + \mathbf{F_b} \right\} A_{mn} = 0 \quad (110)$$

where,

D_{nm} is the distance between the nodal points n and m

m is the neighboring grid blocks of *n*

A_{mn} is the interface area between grid blocks *n* and *m*

P is the pore pressure in slit-pores, [Pa; psia]

P_{clay} is the clay-pore pressure, [Pa; psia]

The geomechanical equation in residual form can be expressed as follows:

$$R_n^{\kappa,\mathrm{k+1}} = \sum_m \left\{ \frac{3(1-v)}{1+v} \nabla\bar{\sigma} - \frac{2(1-2v)}{1+v} \left[\sum_j \{\alpha_j \nabla P_j + 3\beta_t K \omega_j \nabla T_j\} \right] + \mathbf{F_b} \right\} A_{mn} = 0 \quad (111)$$

Here, k and k+1 are the current time and the new time level, respectively; $R_n^{\kappa,\mathrm{k+1}}$ is the residuals of component κ at time k+1, in element n; and A_{nm} is the interface area between elements *n* and *m*. Now, we have additional residual equation which account for the mean stress.

To summarize, in this simulator, we included seven residual equations for component H_2O, salt and CH_4 in slit-pore, H_2O and salt in clay-pore, mean stress and heat to be solved for each volume element. Again, the unknowns are the $N_E * N_\kappa$ independent primary variables (X_i, for $i = 1, \dots, N_E * N_\kappa$) where N_E is the number of elements and N_κ is the number of equations for each element.

5.2.2. Primary Variables

Similar to the simulator described in Chapter 4, the simulator developed in this part included four thermophysical state which are aqueous phase, gaseous phase and two-phases in matrix domain which has three pores, and two-phases in fracture domain with single pore. Since we had seven residuals equations to be solved, we need to choose seven primary variables as the unknowns. In addition to the primary variables for the previous simulator in Chapter 4, another primary variable to be solved was the mean normal stress ($\bar{\sigma}$). The primary variables for each domain and state is shown in Table 7.

Table 7 – Domain, state and primary variables for coupled two-phase flow and geomechanics in a multiporosity gas shale

Domain	State	Primary Variables (X_i)
Shale Matrix	Single phase, aqueous	$P, y_A^{CH_4}, y_A^{Salt}, y_{A,Clay}^{Salt}, P_{clay}, \bar{\sigma}, T$
	Single phase, gaseous	$P, y_G^{CH_4}, y_{A,Clay}^{Salt}, y_{A,Clay}^{H_2O}, P_{clay}, \bar{\sigma}, T$
	Two-phase, aqueous and gaseous	$P, S_G, y_A^{Salt}, y_{A,Clay}^{Salt}, P_{clay}, \bar{\sigma}, T$
Fracture	Two-phase, aqueous and gaseous	$P, S_G, y_A^{H_2O}, y_A^{Salt}, y_G^{H_2O}, \bar{\sigma}, T$

5.2.3. The Newton/Raphson Iteration

The mass and heat balance equations and the geomechanical equation in residual forms were coupled and solved simultaneously on a discretized medium using the Newton/Raphson iteration method in the way that had been described in Chapter 3. We constructed Eq. 57, the Jacobian matrix equations, from the residual equations by differentiating the residual equations in terms of primary variables (X_i). Again, the dimension of the Jacobian matrix is ($N_E * N_\kappa$)*($N_E * N_\kappa$) and the unknowns were the $N_E * N_\kappa$ primary variables. Solution of the Jacobian matrix equations proceeded in an iterative manner until the residuals ($R_n^{\kappa,k+1}$) were reduced below a preset convergence tolerance that described an acceptable (and very low) mass and/or energy balance error.

5.3. Validation using Dean's Problem

The coupled mathematical formulation of flow and geomechanical was validated by comparing to a published problem, Problem 1 in Dean et al. (2006). In the problem, a single aqueous phase (water) reservoir is produced by a single vertical well at the center and completed along the thickness at a constant rate of 27.77 kg/s (15,000 B/D) for 500 days.

The reservoir geometry was 11x11x10 with Δx = Δy = 200 ft (60.96 m) and Δz = 20 ft (6.096 m). Initial pore pressure at top reservoir was 20.7 MPa (3,000 psi), at a depth of

1,829 m (6,000 ft) and had a vertical hydrostatic gradient of 0.433 psi/ft. Initial horizontal stress is 27.6 MPa (4,000 psi) over the entire reservoir depth. The initial vertical stress is 6,000 psi at 1,829 m (6,000 ft), with a vertical stress gradient of 1.0231 psi/ft. No flow boundary conditions are assumed at all faces of the grid. Zero normal displacement is

Table 8 – Parameters used in simulation of Dean's problem (Dean et al., 2006)

Property	Value	Unit
Initial porosity	0.2	-
Horizontal permeability	$5x10^{-14}$	m^2
Vertical permeability	$5x10^{-15}$	m^2
Young's modulus	$6.87x10^{7}$	Pa
Poisson's ratio	0.3	-
Rock density	2700	kg/m^3
Biot coefficient (α)	1.0	

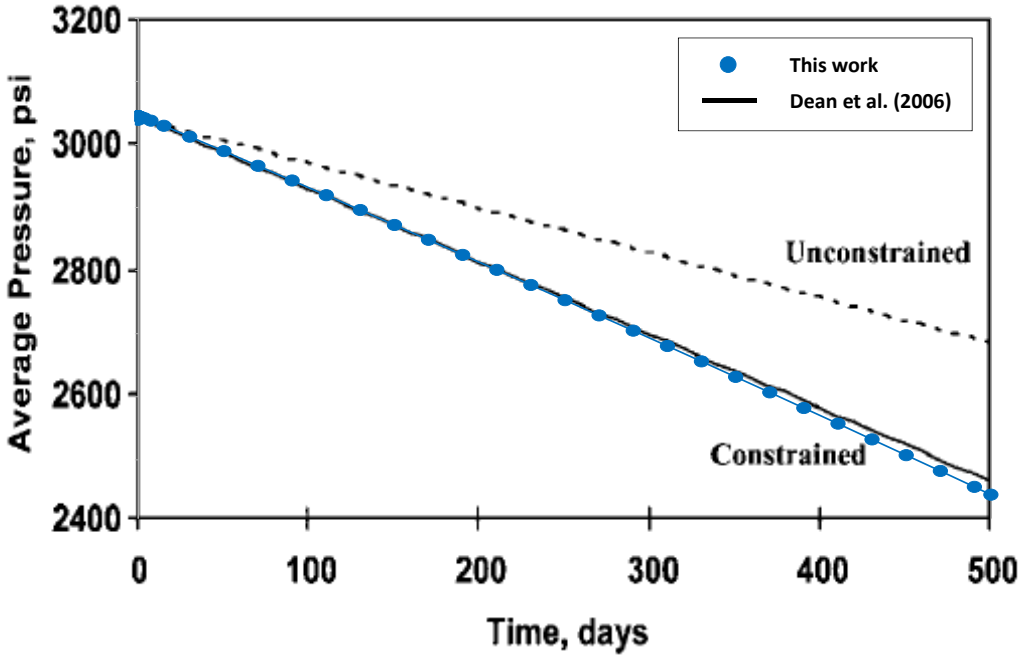

Fig. 34 – Comparison of average pore pressure from this work to Dean et al. (2006).

enforced at the four vertical faces of the reservoir, i.e., constant gridblock volume. To comply with those boundary conditions, additional layer of gridblocks, at top and bottom of the reservoir and at the four vertical faces are added as a constant no flow boundary. Parameters used in this simulation are described in in Table 8. Fig. 34 shows that average reservoir pressure simulated using the coupled flow and geomechanics match Dean et al. (2006) results.

5.4. Description of Geometry and Parameters in Simulation Case Studies

The simulation in this section considers a period of time during which one side of a shale formation is exposed to stimulation water that is left or trapped in fractures after hydraulic fracturing and flow back period before the well is put into production. This period of time here is called as shut-in period.

Multi-stage hydraulic fracturing may create both primary hydraulic fractures that connect to the well and secondary fracture networks surrounding the primary hydraulic fractures. During the hydraulic fracturing, the secondary fracture network is filled mainly with the hydraulic fracturing water. After the stimulation, these unpropped secondary fracture networks may be disconnected from the primary hydraulic fractures and isolated, trapping water inside them. Flowback operation may not recover this trapped water due to lack of connection to the primary hydraulic fractures that connected to well. On the other hand, after flowback period, some water may still exist inside the primary hydraulic fractures. We considered the stimulation water, in both primary and secondary fractures, may cause shale-water interactions during shut-in time.

I consider the geometry of the modeling domain by assuming the possible symmetric circumstances that water imbibes from fracture into shale matrix in the direction perpendicular to fracture-matrix interface as illustrated in Fig. 35. Here, I am interested in studying clay swelling and permeability alteration in the direction perpendicular to

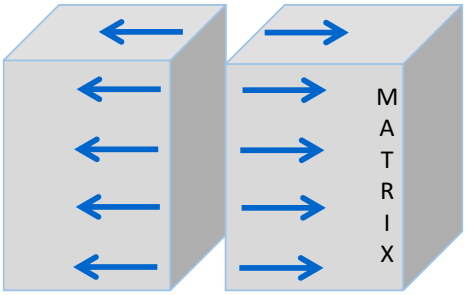

Fig. 35 - This figure illustrate water from a fracture imbibes into shale matrix in the direction that is perpendicular to the fracture-matrix interface.

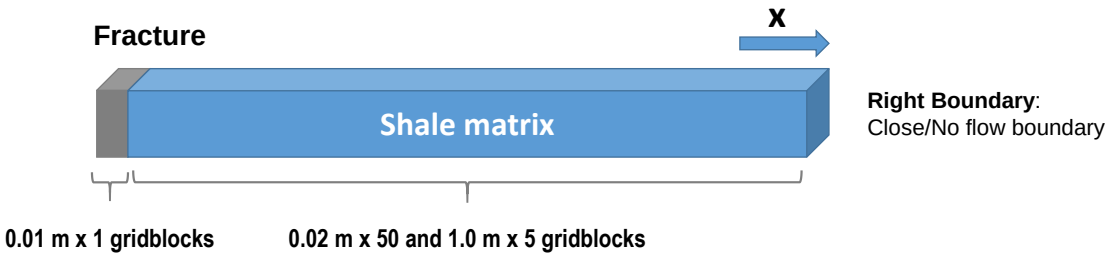

Fig. 36 - The modeling domain consists of a single fracture domain at one end and a shale matrix domain for the rest of the elements. The fracture domain width is 0.01 m. The shale matrix domain consist of 0.02 m x 50 elements and 1.0 m x 5 gridblocks.

fracture face, which was here we selected as the x direction. To take advantage of the symmetry of the mechanism that take into place, I conducted 1D simulation with geometry of the domain is 6.01 x 0.25 x 0.2 m divided into 56 x 1 x 1 in x, y, and z directions. The modeling domain consists of a single fracture domain at one end and a shale matrix domain for the rest of the elements. The fracture domain width is 0.01 m. The shale matrix domain consist of 0.02 m x 50 elements and 1.0 m x 5 elements. We refined the element size near the fracture considering most process will occur near fracture-matrix interface. Fig. 36 demonstrates this model setup.

We may estimate the overburden stress as function of depth using the following relation (Constant and Bourgoyne Jr, 1988; Watson et al., 2003):

$$\sigma_{OB} = 0.0519\left\{\rho_{ma}D - \frac{(\rho_{ma} - \rho_f)\phi_{surf}}{d_\phi}\left[1 - e^{-d_\phi D}\right]\right\} \quad (112)$$

where,

σ_{OB} is the overburden stress, [psi]

ρ_{ma} is the density of rock matrix, [ppg]

ρ_f is the density of pore fluid, [ppg]

D is the formation depth, [ft]

ϕ_{surf} is the rock porosity at surface

d_ϕ is the porosity decline constant, [1/ft]

Assuming linear-elastic and isotropic material, the horizontal stress (σ_H) can be estimated as function of Poisson's ratio and vertical overburden stress using the following relation (Watson et al., 2003):

$$\sigma_H = \left(\frac{v}{1 - v}\right)(\sigma_{OB} - \alpha P_p) + \alpha P_p \quad (113)$$

where,

v is Poisson ratio

α is Biot or poroelastic constant

P_p is pore pressure, [psi]

Let us assume a shale formation at depth 8,000 ft, having pore pressure of 3,800 psi. The porosity decline constant can be calculated for example from the sonic and density log data. In the Gulf Coast, the surface porosity and the porosity decline constant is approximately 8.5E-5 ft^{-1} (Watson et al., 2003). Using those values of the surface porosity and the porosity decline constant with the density of matrix of 21.66 ppg (2.6 g/cm^3) and the density of pore fluid of 8.94 ppg, we get the overburden stress at depth 8,000 ft is 7,422 psi. Using Eq. 113, I obtained the horizontal stress approximately of 5,352 psi using Poisson ratio of 0.3, Biot constant of 1.0 and pore pressure of 3,800 psi. Then, I estimated the mean normal stress approximately equal to 6,042 psi. Fig. 37 illustrates the estimated

stresses with the formation depth. I simulated the shale formation at 8,000 ft and at 17,000 ft, bearing mean stress approximately of 6,000 and 12,000 psi to study the permeability alteration due to clay swelling effect at these depth.

We selected the shale reservoir properties as close as possible to resemble the real shale reservoir because we wanted to understand the effect of stress to the permeability alteration during shut-in which is related to the current overburden stress condition. Here, we picked a shale formation that has pore pressure approximately of 3,800 psi, porosity of 6% and permeability about of 60 nD at effective stress approximately of 6,000 psi. Using Gangi's stress-dependent permeability equation (Eq. 2) we can construct permeability vs effective stress as shown in Fig. 38. Here, we used P_1, the effective stress when the pore is close completely, of 42,000 psi. This permeability vs effective stress can

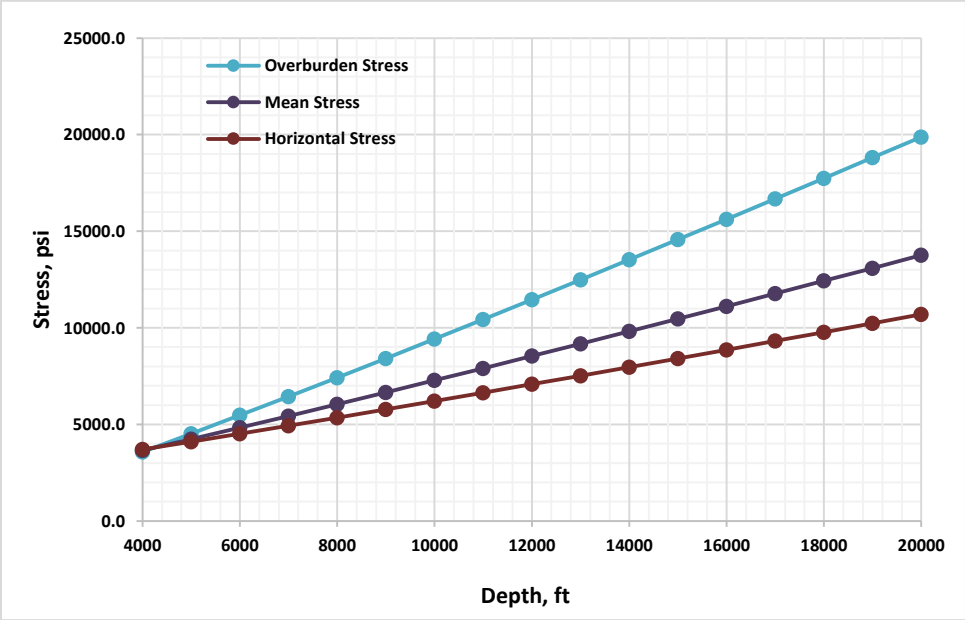

Fig. 37 - The estimated overburden stress, horizontal stress and mean stress with depth.

Table 9 – Gangi's stress-dependent permeability parameters used in simulation coupled problem.

Parameter	Value	Unit
k_0	250	nD
P_1	42,000	psi
P	3,800	psi
χ	0.68	
m	0.5	

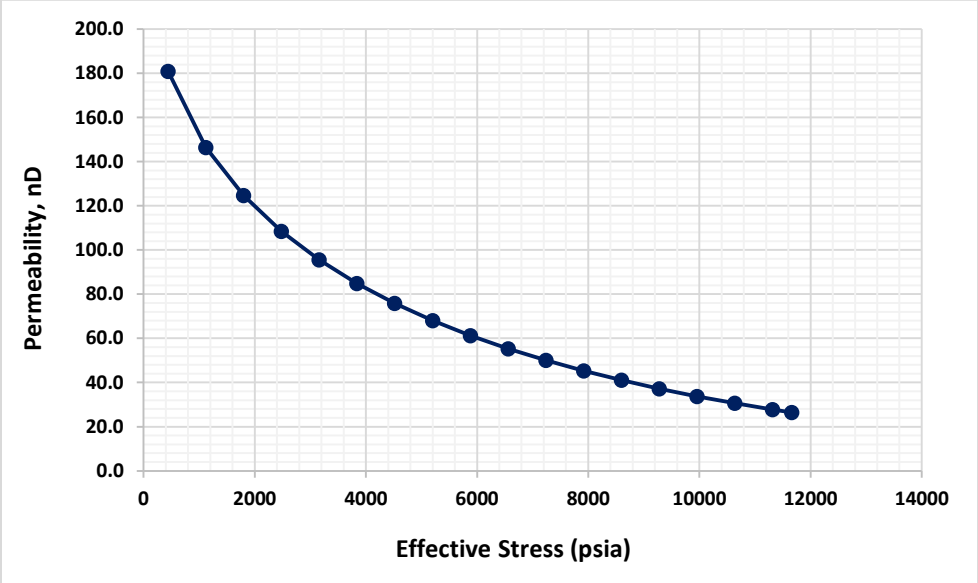

Fig. 38 - Shale permeability as a function of effective pressure as described using Gangi's stress-dependent permeability.

be considered as similar to a particular Barnett shale permeability as function of effective stress (Heller et al., 2014). The permeability at zero effective stress (k_0) is 250 nD, the effective stress coefficient (χ) is 0.68 m, and a coefficient related to the surface roughness of 0.5. The Gangi's stress-dependent permeability model parameters used in this simulation are given in Table 9. For a shale formation with pore pressure of 3,800 psi at depth 8,000 ft, overburden stress of 7,422 psi, mean stress of 6,000 psi, the permeability is approximately of 91 nD. Assuming formation depth approximately of 11,000, 14,000

and 17,000 ft, the mean stress is 8,000, 10,000 and 12,000 psi, and the shale permeability is approximately of 66, 49 and 37 nD. I considered the formation depth and stress fields in our simulation case studies here.

We have observed the effect of clay membrane efficiency to clay-pore pressure using the previous simulator for two-phase flow in shale gas formation containing multi porosity with clay swelling effect, described in Chapter 4. In this section, we wanted to study further the effect of clay membrane efficiency to clay-pore pressure increase when flow is coupled with geomechanics, how clay-pore pressure dynamics evolve with different stress field. In addition to that, we wanted to observe stress effect to clay membrane efficiency which simultaneously affect clay-pore pressure and permeability.

In this section, we used varied clay membrane efficiency predicted using Eq. 105 as described by Marine and Fritz (1981) and Rahman et al (2005). Membrane efficiency of clays is a function of cation exchange capacity (CEC) of clays, clay porosity, mean salt concentration and stress (Marine and Fritz, 1981; Rahman et al., 2005). CEC of clays are different for different type of clay minerals. Table 10 shows range of CEC for common clay minerals. Using CEC of 5, 40, 80 and 150 meq/100g, we may assume shale formation containing different clay types, as kaolinite, illite, chlorite or montmorillonite. Some US gas shale formations are clay-rich formation, containing illite, kaolinite and chlorite, as shown in Table 11 (Chalmers et al., 2012).

I calculated membrane efficiency for CEC of 5, 40, 80 and 150 meq/100g for different stress as shown in Fig. 39, using clay porosity of 10%, mean salt concentration (C_s) of 1.9E-3 mol/cm^3. It can be observed that at high stress environment, membrane efficiency is high for CEC higher than 40 meq/100g, range from 0.7 to 0.9 at stress range of 2,000 – 12,000 psi. At stress field 6,000 psi, membrane efficiency of clay containing CEC of 5 meq/100g is about 0.4 and it ranges from 0.28 to 0.5 at stress range of 2,000 – 12,000 psi.

Table 10 – Cation exchange capacity (CEC) of clay minerals. Reprinted from Grim (1968).

Clay Minerals	CEC, in meq/100 g
Kaolinite	3 - 15
Illite	10 - 40
Chlorite	10 - 40
Montmorillonite	80 - 150
Vermiculite	100 - 150

Table 11 – Mineralogical composition of sample suites. Reprinted from Chalmers et al. (2012).

Sample ID	Quartz	Illite	Kaolinite	Chlorite	Total Clay	Feldspar	Gypsum	Pyrite	Apatite	Calcite	Siderite	Dolomite	Total Carbonate
Haynesville	24.1	43.2	0.9	0.6	44.7	6.6	0.0	2.5	0.0	17.9	0.0	3.0	20.9
Doig siltstone	58.5	5.5	0.0	0.0	5.5	15.2	0.0	0.6	1.2	1.8	0.0	17.3	19.1
Woodford	32.0	41.0	1.4	3.4	45.8	9.0	0.0	3.1	0.0	6.2	0.0	3.9	10.1
Marcellus	28.7	33.6	3.4	6.0	43.0	21.3	0.0	0.6	0.0	3.5	3.0	0.0	6.5
Barnett	46.7	31.4	3.8	1.1	36.3	3.8	1.0	3.0	1.5	5.7	0.9	1.2	7.8
Doig phosphate	20.4	10.5	0.0	0.0	10.5	18.3	0.0	2.1	3.9	22.4	0.0	22.6	45.0

*From x-ray diffraction and Reitveld Refinement (Rietveld, 1967).

It can be concluded that at subsurface, it could be rare to find clay with membrane efficiency lower than 0.2.

I conducted simulation of several case studies using varied CEC values of 5, 40, 80 and 150 meq/100g. It was assumed that the fracture has constant pressure and temperature and contains constant 100% water saturation and salt concentration because the dimension of shale pore volume can be considered to be much smaller than the dimension of fracture volume. I used Gangi's permeability parameters as described in Table 9. I varied the initial mean stress 6,000, 8,000, 10,000 and 12,000 psi, such that we may find the formation at a depth of 8,000, 11,000, 14,000 or 17,000 ft. Other parameters used in the simulation is listed in Table 12.

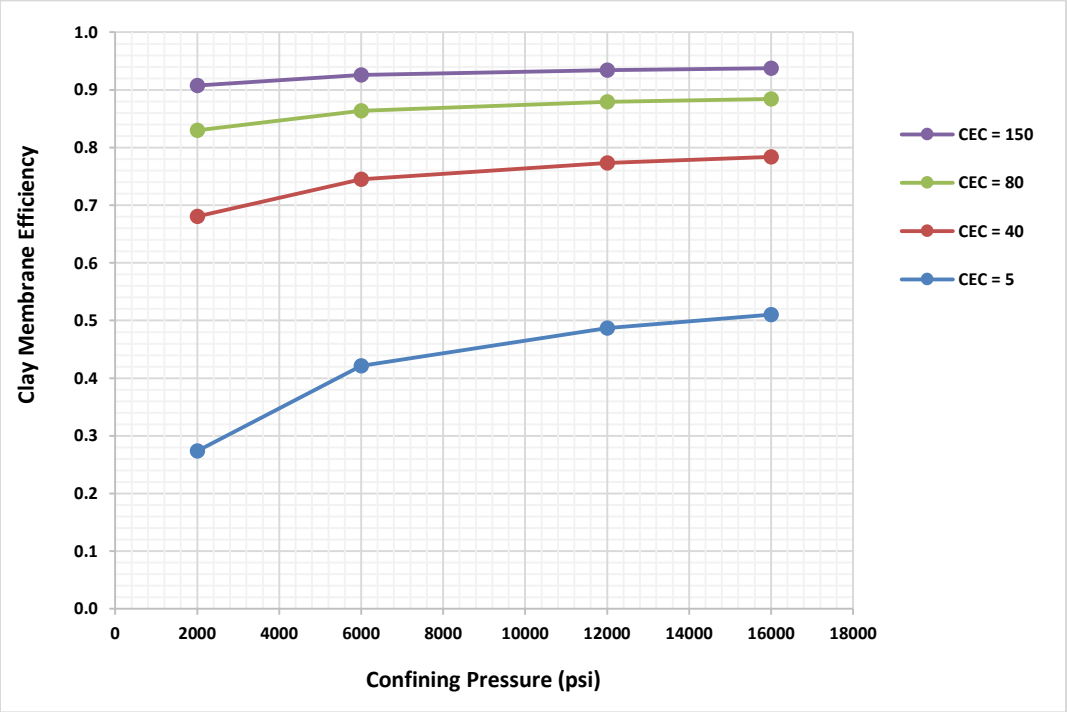

Fig. 39 - Clay membrane efficiency estimation for different CEC and confining pressure (stress).

Table 12 – Shale gas properties and parameters used in simulation

Parameter	Value	Unit
Initial slit-shaped pore pressure	3800	psi
Initial clay-pore pressure	3800	psi
Initial temperature	70	^{o}C
Porosity:		
ϕ_k (organic)	2%	
ϕ_I (inorganic)	6%	
ϕ_C (clay)	10%	
Initial water saturation:		
in ϕ_k	0%	
in ϕ_I	20%	
in ϕ_C	100%	
Sorption Properties		
Grain Density	2650	kg/m^3
Langmuir volume (V_{sL})	5.66E-03	m^3/kg
Langmuir pressure (P_L)	3.45E+06	Pa
Total organic grain volume / total grain volume (Ɛks)	0.02	
Diffusion Coefficient		
Surface diffusion coefficient	1.00E-09	m^2/s
Diffusion coefficient of CH_4 in aqueous phase	1.72E-09	m^2/s
Diffusion coefficient of salt in aqueous phase	2.60E-13	m^2/s
Diffusion coefficient of CH_4 in gas phase	1.00E-09	m^2/s
Osmotic Model Parameters		
Clay-membrane permeability (k_m)	1.00E-01	nD
Shape factor	1.00E-02	
Clay-membrane efficiency	Eq. 105	
Salt type	NaCl	
Elastic Parameters		
Poisson Ratio	0.3	
Biot Coefficient	1.0	
Young's Modulus	3.00E+10	
Rock Thermal Expansion (b)	0.00E+00	

5.5. Simulation Results and Analysis

5.5.1. Effect of Formation Depth and Overburden Stress on Clay-membrane Efficiency

Fig. 40 and Fig. 41 shows the predicted clay-membrane efficiency for the two cases of shale formation at initial mean stress of 6,000 psi and 12,000 psi. CEC is kept constant at 80 meq/100g during the computations For the case of 6,000 psi, the clay-membrane efficiency varies in between 86.5% and 91.5% and for the case of 12,000 psi the efficiency is in between 88% and 92%. Clearly, the shale's clay membrane efficiency does not change significantly because it is controlled by the CEC value of the clay which is kept constant. The small difference observed is due to the difference in initial mean stress. The mean stress affects the clay-membrane efficiency directly because clay porosity and the friction coefficient of anion to membrane are functions of the mean stress. In fact, the friction coefficient of anion to membrane is directly affected by the mean stress. The porosity of clay is function of the clay-pore pressure. These show the complexity of the relations between the clay-pore pressure, the clay-membrane efficiency and the mean stress as they are affecting each other.

Fig. 40 and Fig. 41 show that the clay-membrane efficiency values for the elements near fracture-face are larger and increase in time. These are due to the increasing mean stress and the decreasing mean salt concentration with the shut-in time. Fig. 42 and Fig. 43 show the mean stress profiles at different shut-in time for the cases of initial mean stress of 6,000 psi and 12,000 psi. Initially (0.0001 day) the mean stress jumps about 150 psi in both cases due to spontaneous imbibition mechanism. At 0.5 day, the mean stress in both cases is lower to 100 psi as pore pressure (in slit-pore) dissipate towards outer boundary. Subsequently, for case 6,000 psi, the mean stress keep increasing with increase shut-in time. However, for case 12,000 psi, the mean stress is still decreasing until about shut-in time of 1 day and after that the mean stress is increasing and propagating towards outer boundary. The increase of the mean stress at later time is mostly related to clay-pore

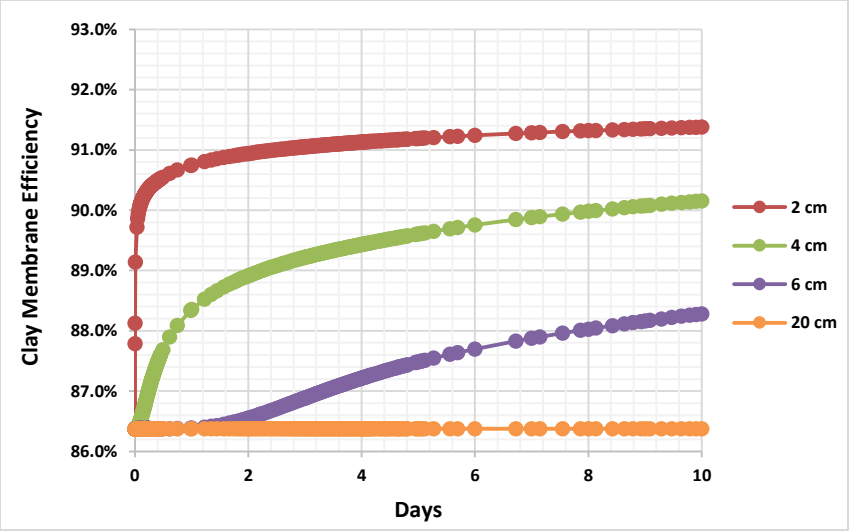

Fig. 40 - Clay membrane efficiency profile for the matrix elements at 2, 4, 6 and 20 cm from the fracture element at shut-in time 0 to 10 days for case with initial mean stress of 6,000 psi and CEC = 80 meq/100g.

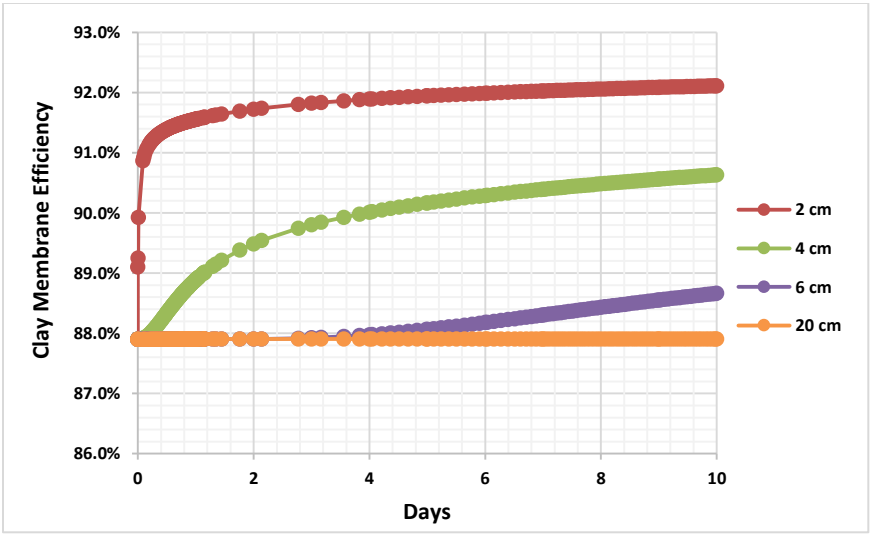

Fig. 41 - Clay membrane efficiency profile for the matrix elements at 2, 4, 6 and 20 cm from the fracture element at shut-in time 0 to 10 days for case with initial mean stress of 12,000 psi and CEC = 80 meq/100g.

pressure increase due to osmosis. This increasing mean stress causes an increase in membrane efficiency over time. However, at the initial time, the increase of membrane efficiency values in both cases are resulted from the lowering of mean salt concentration as fresher water from fracture flow into slit-pore then into clay-pore. As predicted by Eq. 105, lower mean salt concentration means higher membrane efficiency. Fig. 44 and Fig. 45 show that salt mass fraction in both cases have similar values. Comparing Fig. 46 to Fig. 47, we can observe that salt mass fraction in clay-pore is lower in case initial mean stress of 6,000 psi than of 12,000 psi. This can be explained by the effect of membrane efficiency itself that the higher the value less salt can be flow in or out of the membrane. Here, one can conclude that the formation depth and the overburden stress affect the clay-membrane efficiency values directly due to the mean stress values and indirectly due to mean salt concentration controlled by the membrane efficiency values.

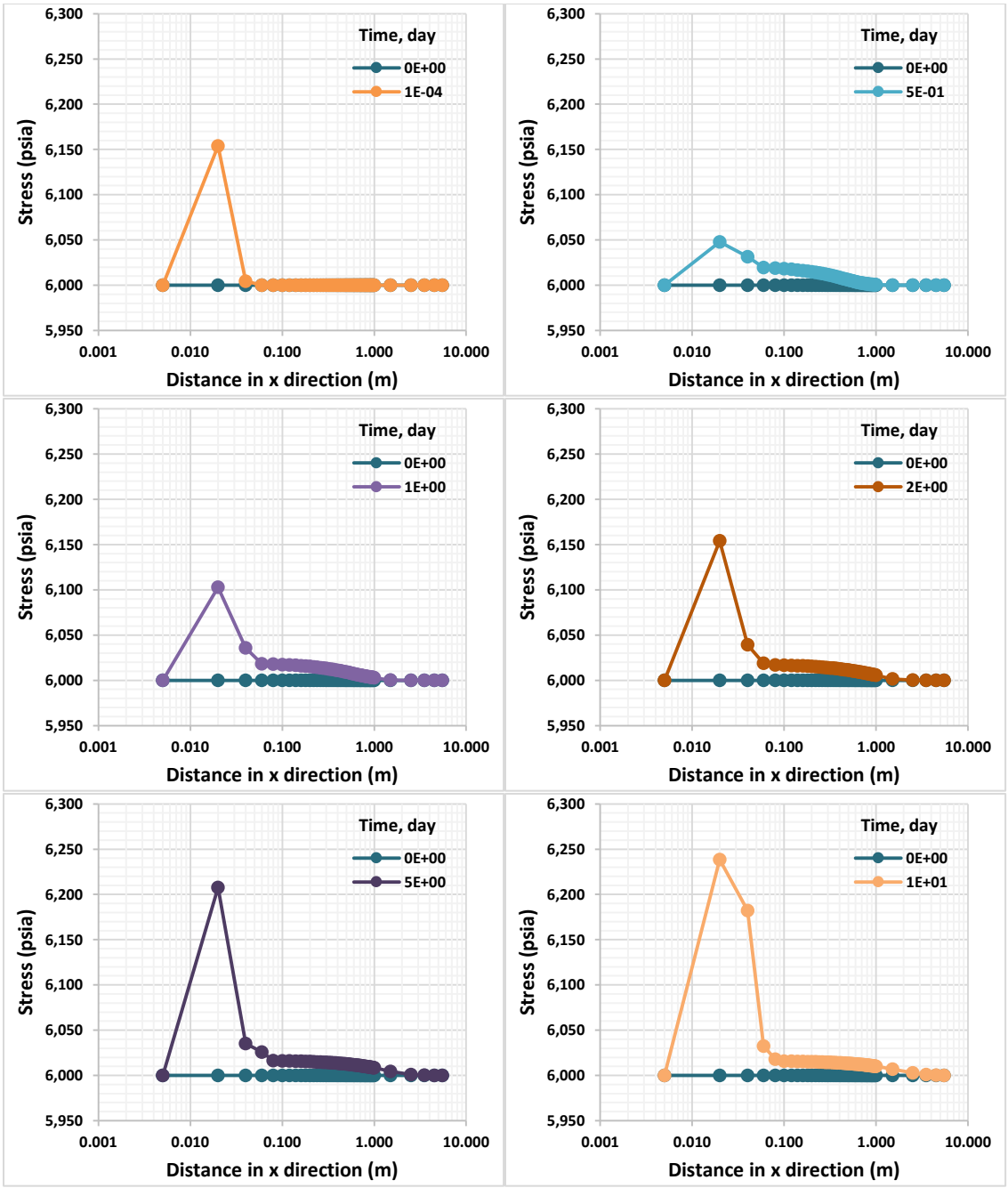

Fig. 42 - Mean stress profile at shut-in time 0.0001, 0.5, 1, 2, 5, and 10 days for case with initial mean stress of 6,000 psi and CEC = 80 meq/100g.

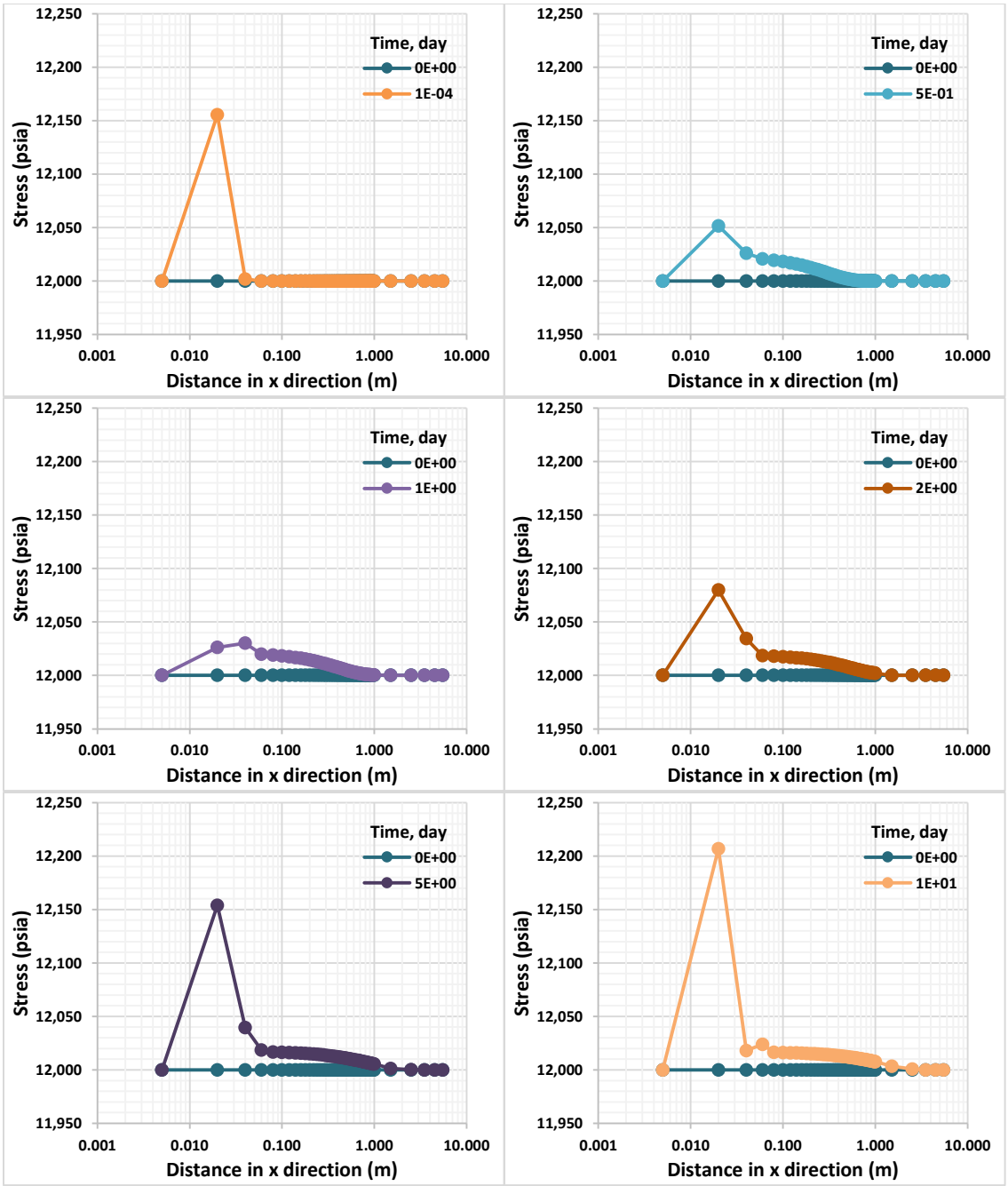

Fig. 43 - Mean stress profile at shut-in time 0.0001, 0.5, 1, 2, 5, and 10 days for case with initial mean stress of 12,000 psi and CEC = 80 meq/100g.

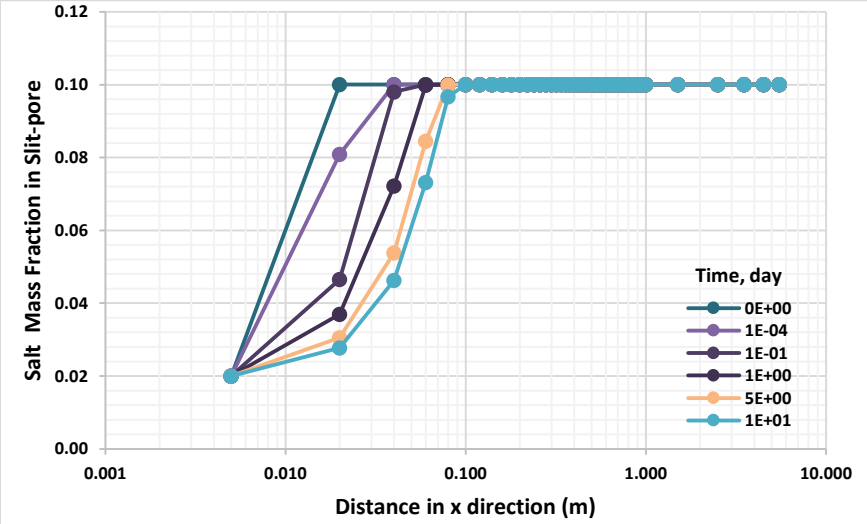

Fig. 44 - Salt mass fraction in slit-pore profile at shut-in time 0.0001, 0.1, 1, 5, and 10 days for case with initial mean stress of 6,000 psi and CEC = 80 meq/100g.

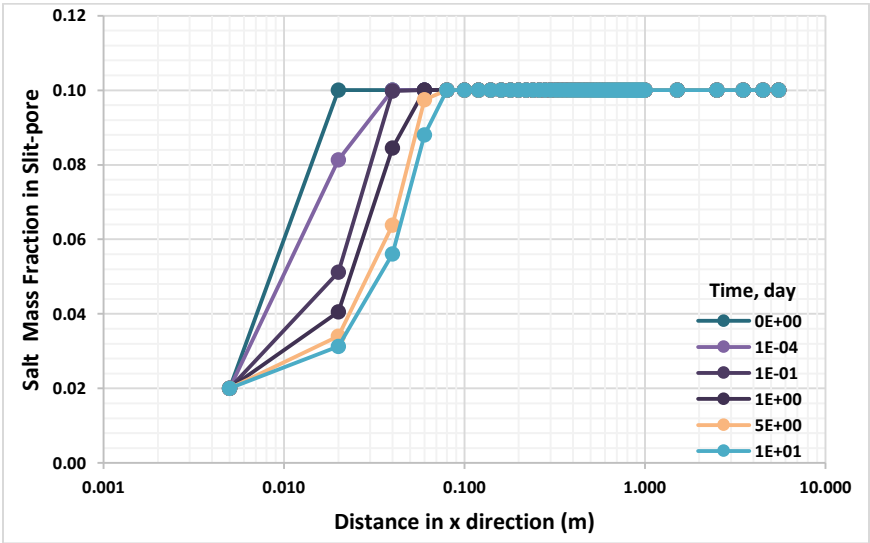

Fig. 45 - Salt mass fraction in slit-pore profile at shut-in time 0.0001, 0.5, 1, 2, 5, and 10 days for case with initial mean stress of 12,000 psi and CEC = 80 meq/100g.

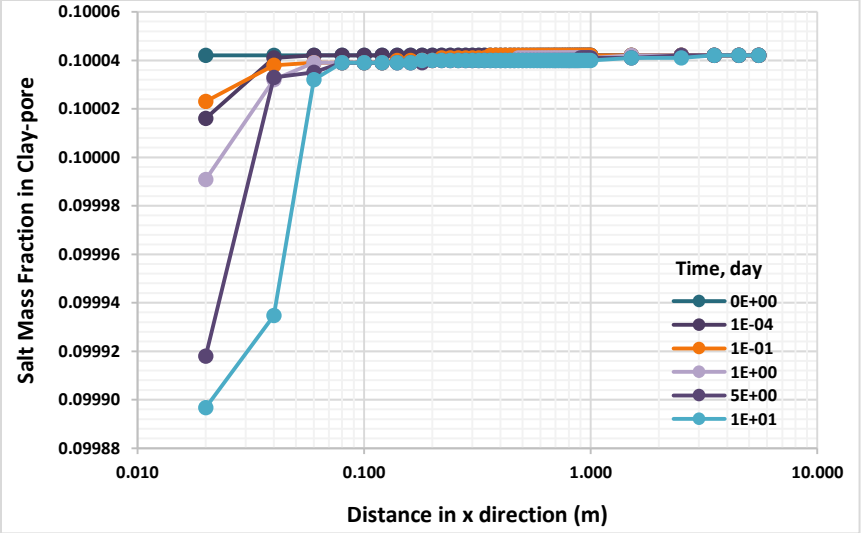

Fig. 46 - Salt mass fraction in clay-pore profile at shut-in time 0.0001, 0.1, 1, 5, and 10 days for case with initial mean stress of 6,000 psi and CEC = 80 meq/100g.

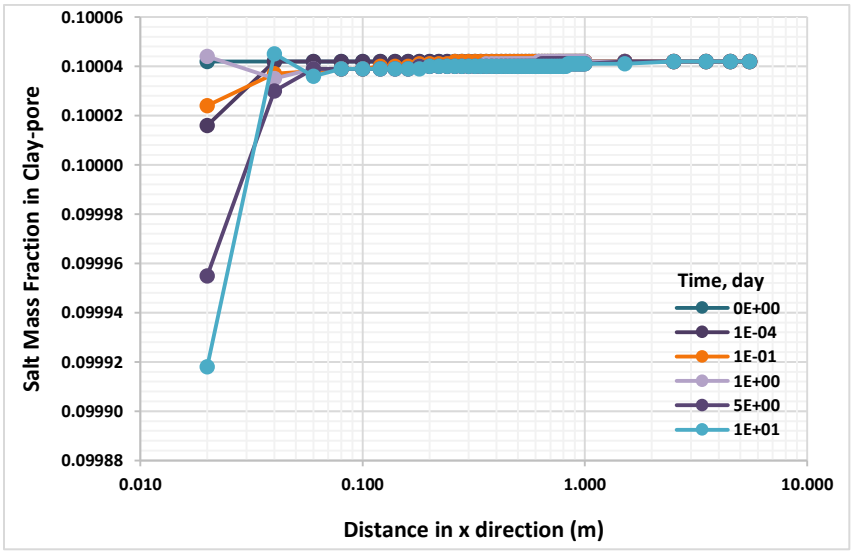

Fig. 47 - Salt mass fraction in clay-pore profile at shut-in time 0.0001, 0.5, 1, 2, 5, and 10 days for case with initial mean stress of 12,000 psi and CEC = 80 meq/100g.

5.5.2. Effect of Formation Depth and Overburden Stress on Clay-pore Pressure

To study the effect of the overburden stress on the clay-pore pressure, I varied the initial mean stress while other parameters are kept the same at their base values. First, I compared the case with the initial mean stress of 6,000 psi and of 12,000 psi, CEC = 80 meq/g. The clay-pore pressure resulted from these simulations for shut-in time 0.0001, 0.5, 1, 2, 5, and 10 days are shown in Fig. 48 and Fig. 49. I compared the initial shut-in time because at longer times, a combination of several mechanisms affects the clay-pore pressure and the behavior is nonlinear and more complex. The clay-pore pressure at element near fracture-face generally increases with shut-in time. The region of increased clay-pore pressure is expanding toward outer right boundary in a slow manner such that after 10 days of shut-in the pressure wave reaches to approximately 8 cm into the matrix for the case of 6,000 psi and 6 cm for the case of 12,000 psi. At initial time, less than 1 day, the clay-pore pressure values are similar about 3,970 psi for case initial mean stress of 6,000 psi and 3,980 psi for case 12,000 psi. After the first jump, however, the clay-pore pressure is decreasing and subsequently is increasing at shut-in time of 1 day for the case with initial mean stress of 6,000 psi and later for the other case. The clay-pore pressure is increasing initially at the first element and then at the next elements in time. I compared the clay-pore pressure profile at shut-in time of 10 days in Fig. 50 for the case with CEC = 80 meq/100g and initial mean stress of 6000, 8000, 10000 and 12000 psi. The profiles show lower clay-pore pressure at higher initial mean stress.

Mean stress has significant effect on the clay-pore pressure magnitude and profile. As shown in Fig. 48 and Fig. 49, although the clay-membrane efficiency is higher in the case with initial mean stress of 12,000 psi, which is initially equal to 88%, the clay-pore pressure at shut-in time of 10 days is lower than the case with initial mean stress of 6,000 psi that has initial membrane efficiency of 86.5%. At shut-in time of 10 days, the clay-pore pressure at fracture-face is 4,300 psi for case 12,000 psi and 4,400 psi for case 6,000 psi. It can be concluded that stress has depressed the increase in clay-pore pressure.

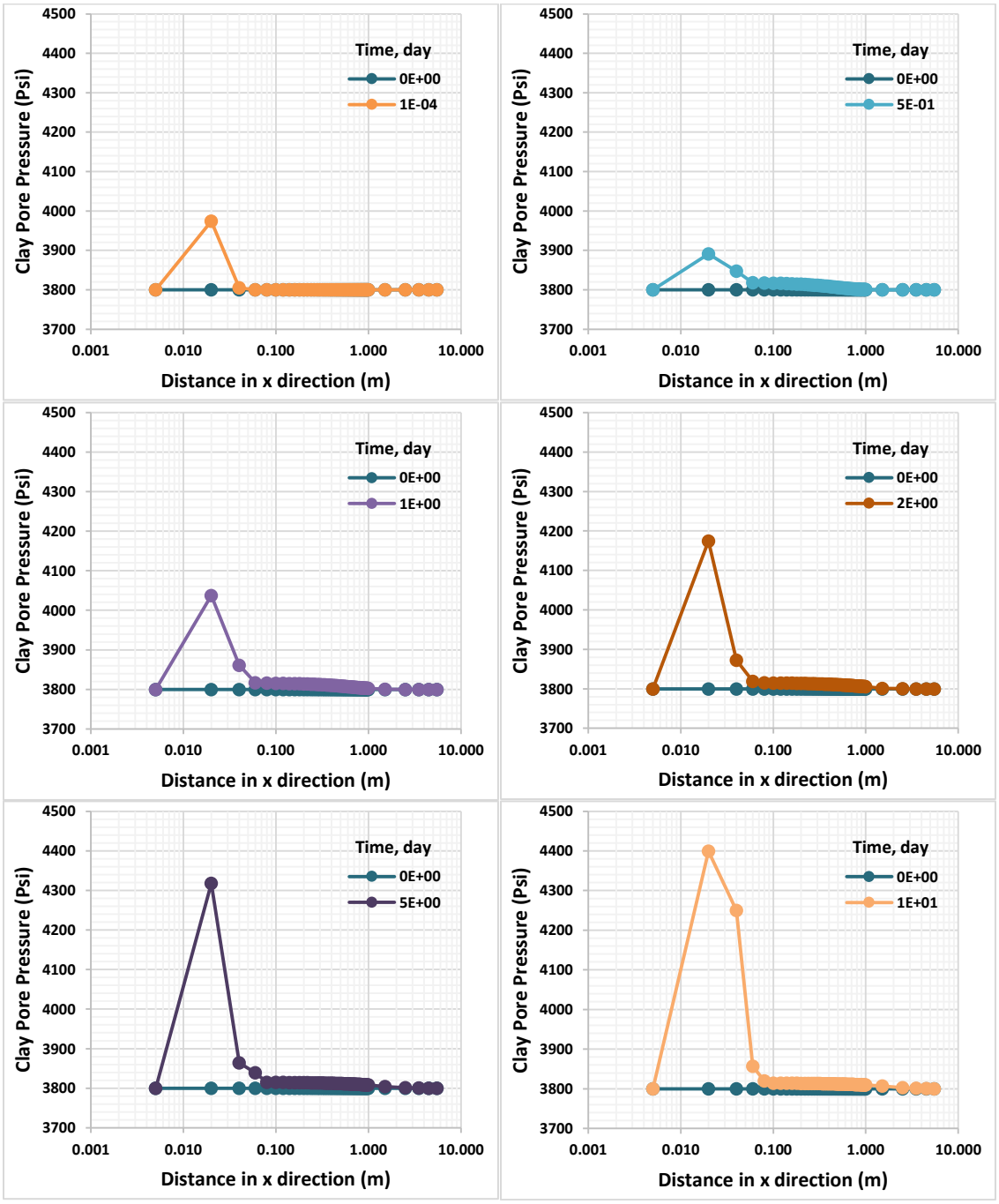

Fig. 48 - Clay-pore pressure distribution at shut-in time 0.0001, 0.5, 1, 2, 5, and 10 days for case with initial mean stress of 6000 psi and CEC = 80 meq/100g.

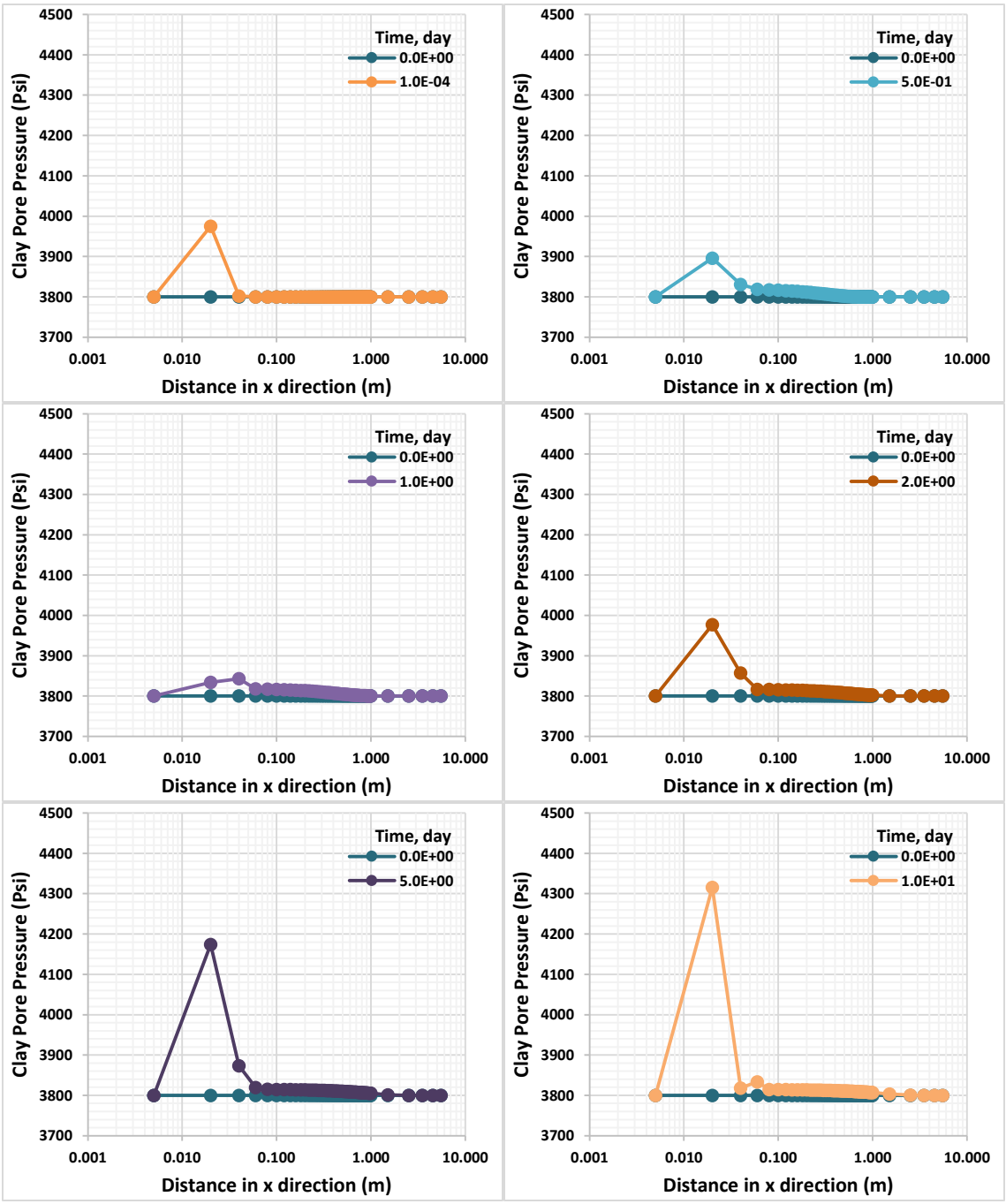

Fig. 49 - Clay-pore pressure distribution at shut-in time 0.0001, 0.5, 1, 2, 5, and 10 days for case with initial mean stress of 12000 psi and CEC = 80 meq/100g.

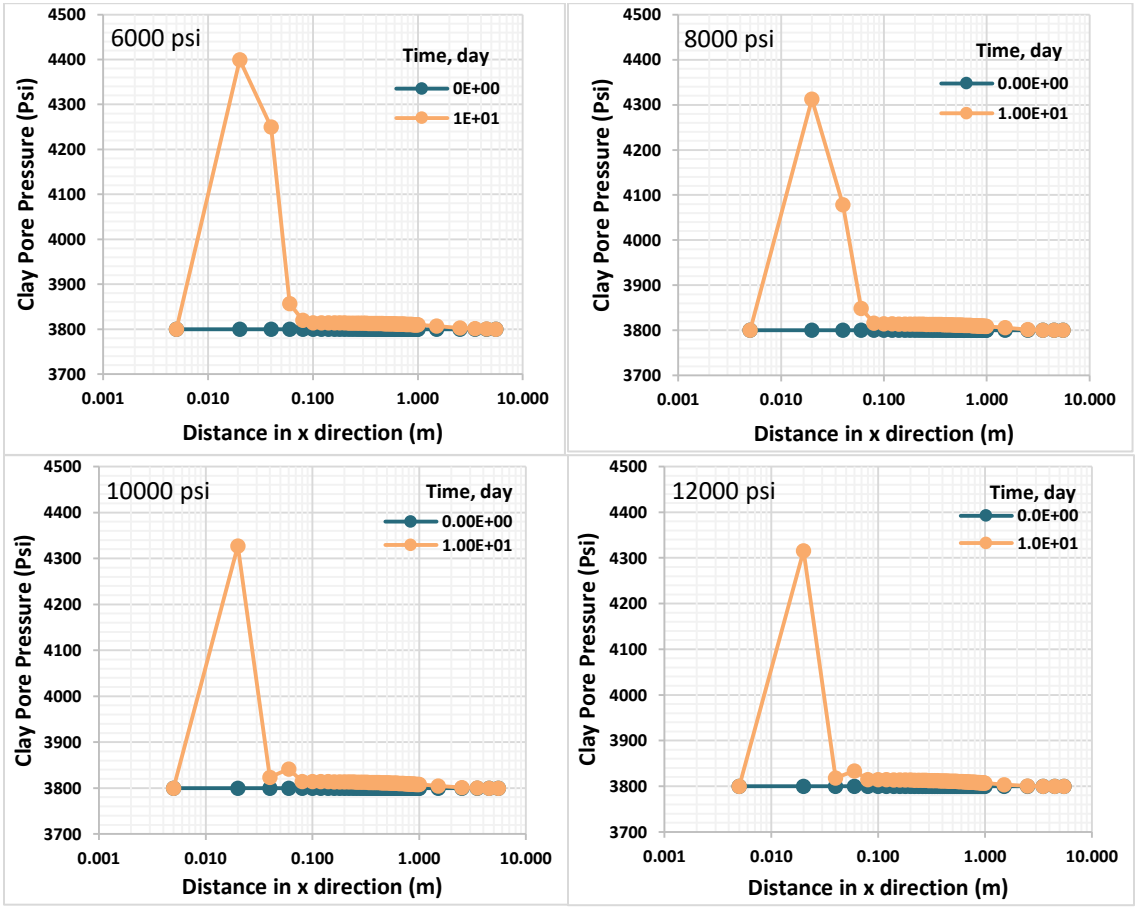

Fig. 50 - Clay-pore pressure profile at shut-in time 10 days for case with CEC = 80 meq/100g and initial mean stress of 6000, 8000, 10000 and 12000 psi.

5.5.3. Effect of Formation Depth and Overburden Stress on Permeability

Fig. 51 to Fig. 54 show that the shale matrix permeability is affected by the overburden stress. Higher stress results in lower permeability reduction. At shut-in time of 10 days, the permeability reduction is approximately 13% and 10% at the element 2 and 4 cm from fracture for the case of initial mean stress of 6,000 psi (Fig. 51) and about 9.6% and 0.2% for the case of 12,000 psi (Fig. 52). Fig. 53 shows permeability values for elements at 2, 4, 6 and 10 cm from fracture during 10 days of shut-in for the case with initial mean stress of 6,000 psi and CEC = 80 meq/100g that permeability at the fracture-face, at 2 cm from fracture, has reduced from the initial permeability of 90 nD to 80 nD and at 4 cm from fracture has reduced to 82 nD. For the case with initial mean stress of 12,000 psi and CEC = 80 meq/100g as shown in Fig. 54, at shut-in time of 10 days, significant permeability reduction only occur at fracture-face, at 2 cm from fracture, and other elements are still near to their initial permeability values.

Here, the permeability of the shale matrix is affected and varied with formation depth and overburden stress by two mechanisms. First, the permeability decreases with the increase in the effective stress, which is the function of formation depth, i.e. the overburden stress, and with the pore pressure through Gangi's dynamic permeability model. Secondly, the permeability decreases due to additional stress caused by the clay-pore pressure and the subsequent clay swelling effect, which varies depending on the overburden stress as shown in the previous section 5.5.2.

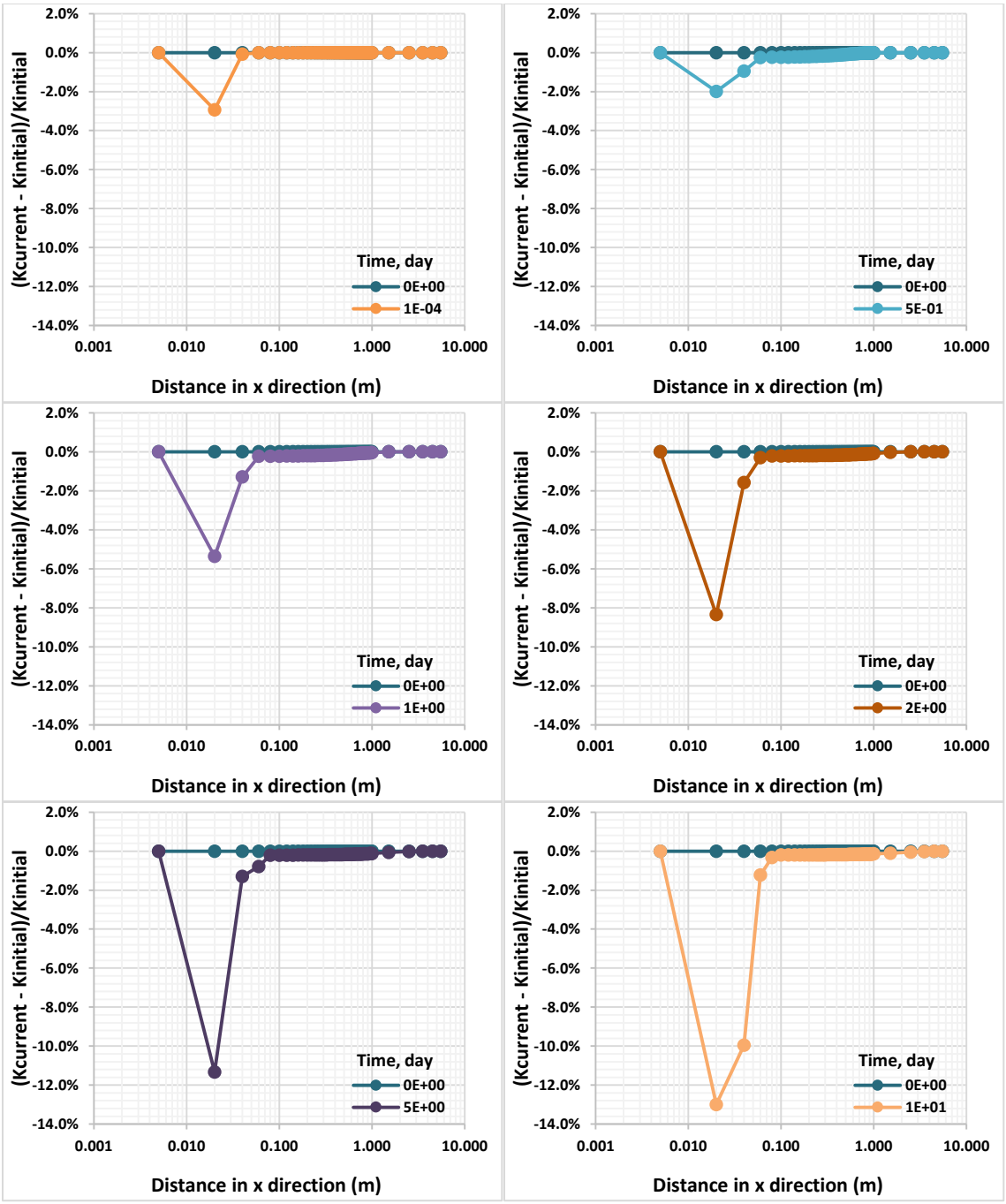

Fig. 51 - Permeability reduction profile at shut-in time 0.0001, 0.5, 1, 2, 5, and 10 days for case with initial mean stress of 6,000 psi and CEC = 80 meq/100g.

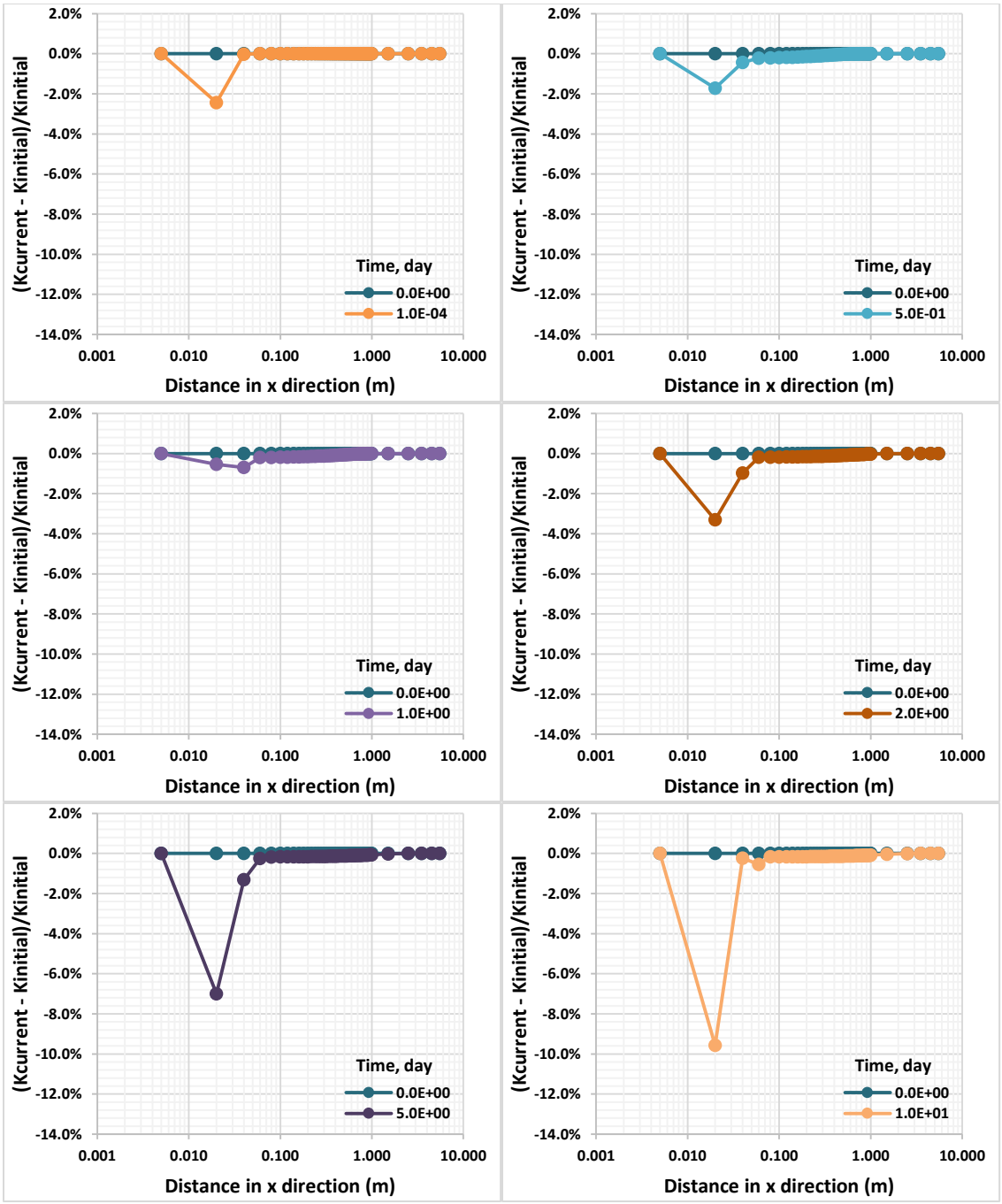

Fig. 52 - Permeability reduction profile at shut-in time 0.0001, 0.5, 1, 2, 5, and 10 days for case with initial mean stress of 12,000 psi and CEC = 80 meq/100g.

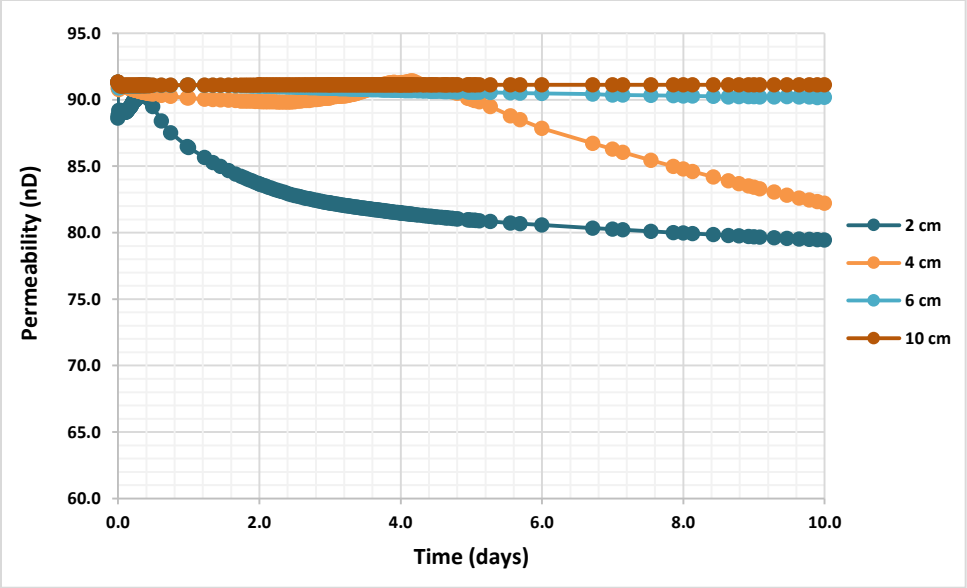

Fig. 53 - Permeability reduction history for elements at 2, 4, 6 and 10 cm from fracture during 10 days of shut-in for case with initial mean stress of 6,000 psi and CEC = 80 meq/100g.

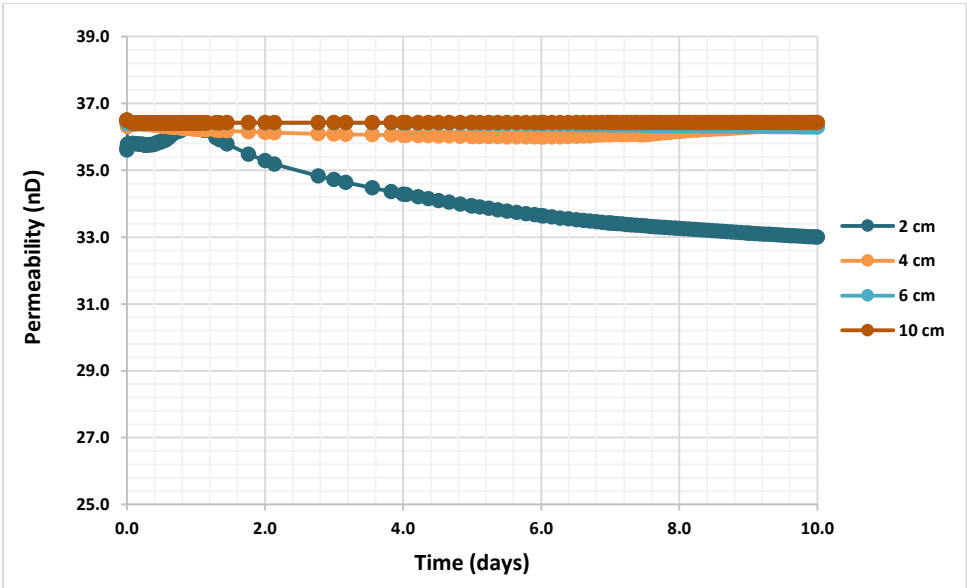

Fig. 54 - Permeability reduction history for elements at 2, 4, 6 and 10 cm from fracture during 10 days of shut-in for case with initial mean stress of 12,000 psi and CEC = 80 meq/100g.

5.5.4. Effect of CEC on Clay-pore Pressure and Permeability

In this section, the simulation cases were run using different CEC values while the other parameters are kept unchanged. As discussed before, higher CEC results in higher clay-membrane efficiency. Previously, we have observed numerically in Chapter 4 that higher clay-membrane efficiency causes higher clay-pore pressure. As shown in Fig. 55 to Fig. 57, under the same stress field, the higher CEC value generally causes a higher clay-pore pressure during the shut-in time. The clay-pore pressure at 2 and 4 cm from fracture are 4,410 and 4,010 psi for case with CEC of 5 meq/100g, and 4,370 and 4,140 psi for case with CEC of 40 meq/100g at shut-in time of 10 days as can be seen in Fig. 55 and Fig. 56. In Fig. 57, it can be seen that after 30 days of shut-in, the clay-pore pressure at 2 and 4 cm from fracture are 4,530 and 4,450 psi for case with CEC of 5 meq/100g, and 4,520 and 4,690 psi for case with CEC of 80 meq/100g.

By the mechanisms as discussed previously, the increase of the clay-pore pressure, causes additional stress to the shale matrix and results permeability reduction. Since higher CEC leads to higher clay-pore pressure, then the higher CEC in clay causes higher permeability reduction. Permeability reduction for the case with initial mean stress of 6,000 psi, CEC = 5 meq/100g (as shown in Fig. 58) is approximately 13% and 4.7% and for case with CEC = 40 meq/100g (as shown in Fig. 59) is 12% and 7.7% at 2 and 4 cm from fracture after shut-in of 10 days. At shut-in time of 30 days, significant permeability reductions occur only at 2 and 4 cm from fracture, decreasing the permeability from 90 nD to 77 and 79 nD for the case with CEC of 5 meq/100g as shown in Fig. 60. For the case with CEC of 80 meq/100g, significant permeability reductions occur at 2, 4 and 6 cm from fracture, decreasing the permeability from 90 nD to 77, 74 and 81 nD at shut-in time of 30 days as can be seen in Fig. 61.

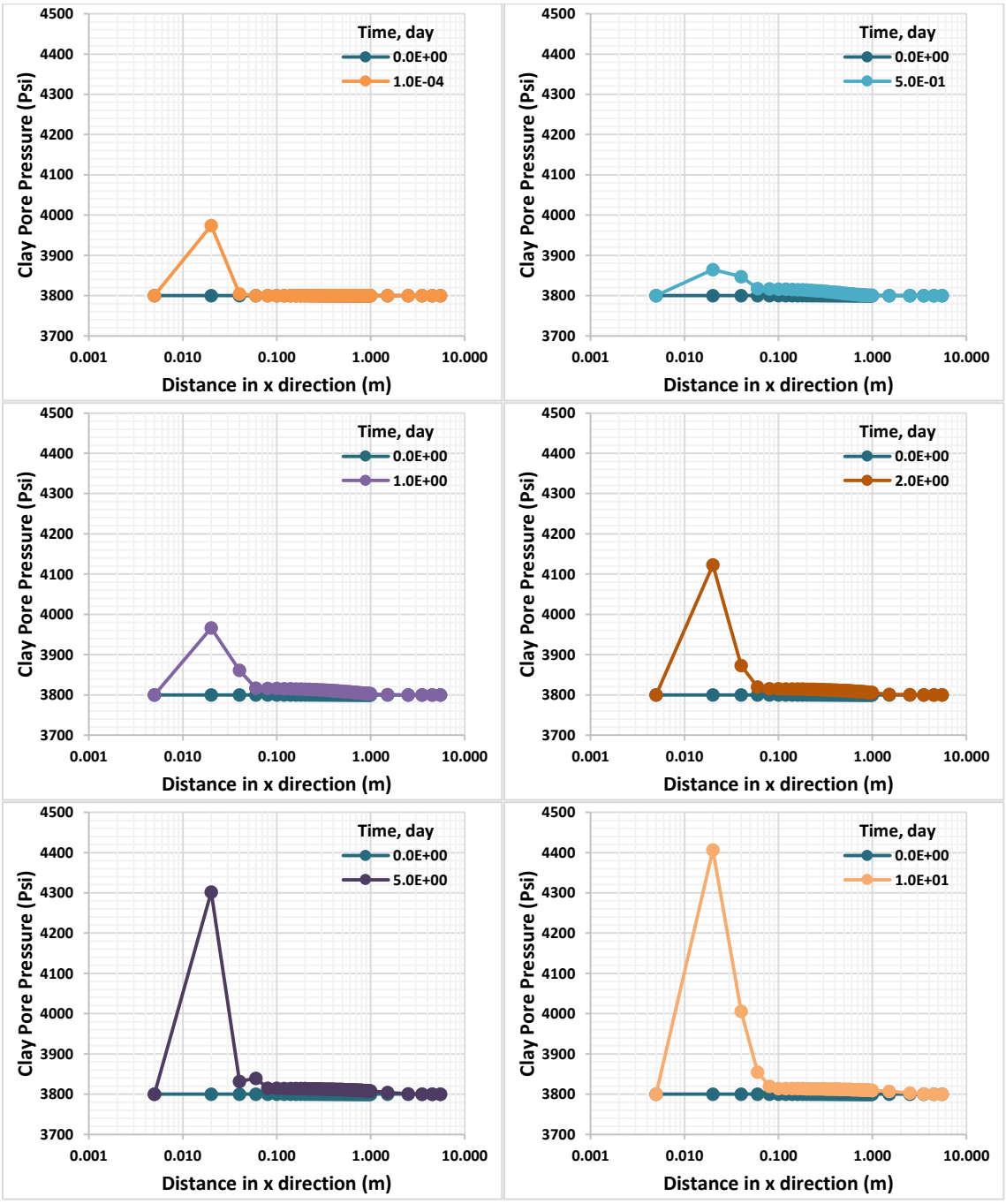

Fig. 55 - Clay-pore pressure distribution at shut-in time 0.0001, 0.5, 1, 2, 5, and 10 days for case with initial mean stress of 6000 psi and CEC = 5 meq/100g.

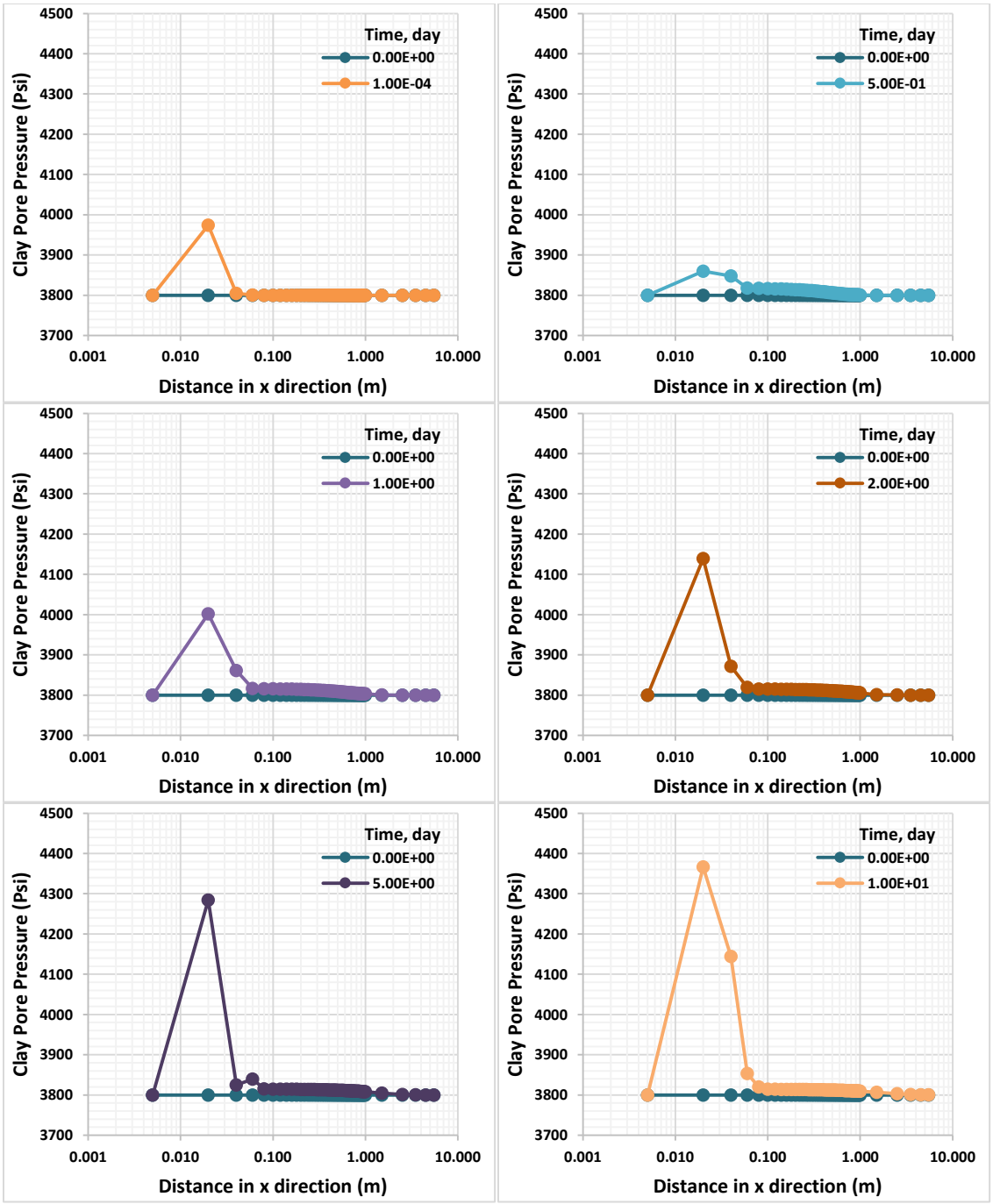

Fig. 56 - Clay-pore pressure distribution at shut-in time 0.0001, 0.5, 1, 2, 5, and 10 days for case with initial mean stress of 6000 psi and CEC = 40 meq/100g.

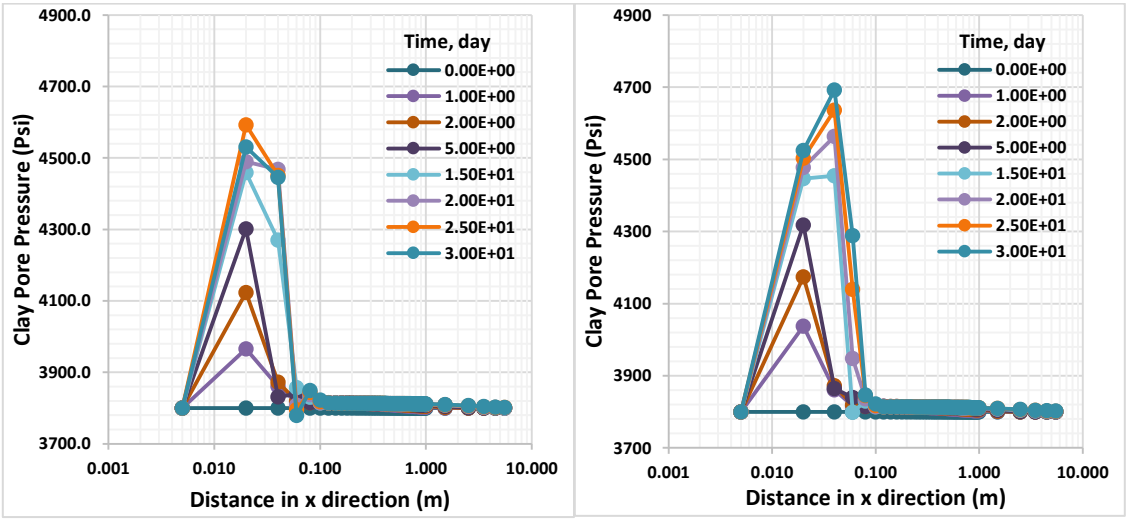

Fig. 57 - Clay-pore pressure profile at shut-in time 0 - 30 days for case with initial mean stress of 6000 psi and CEC of 5 meq/100g and 80 meq/100g.

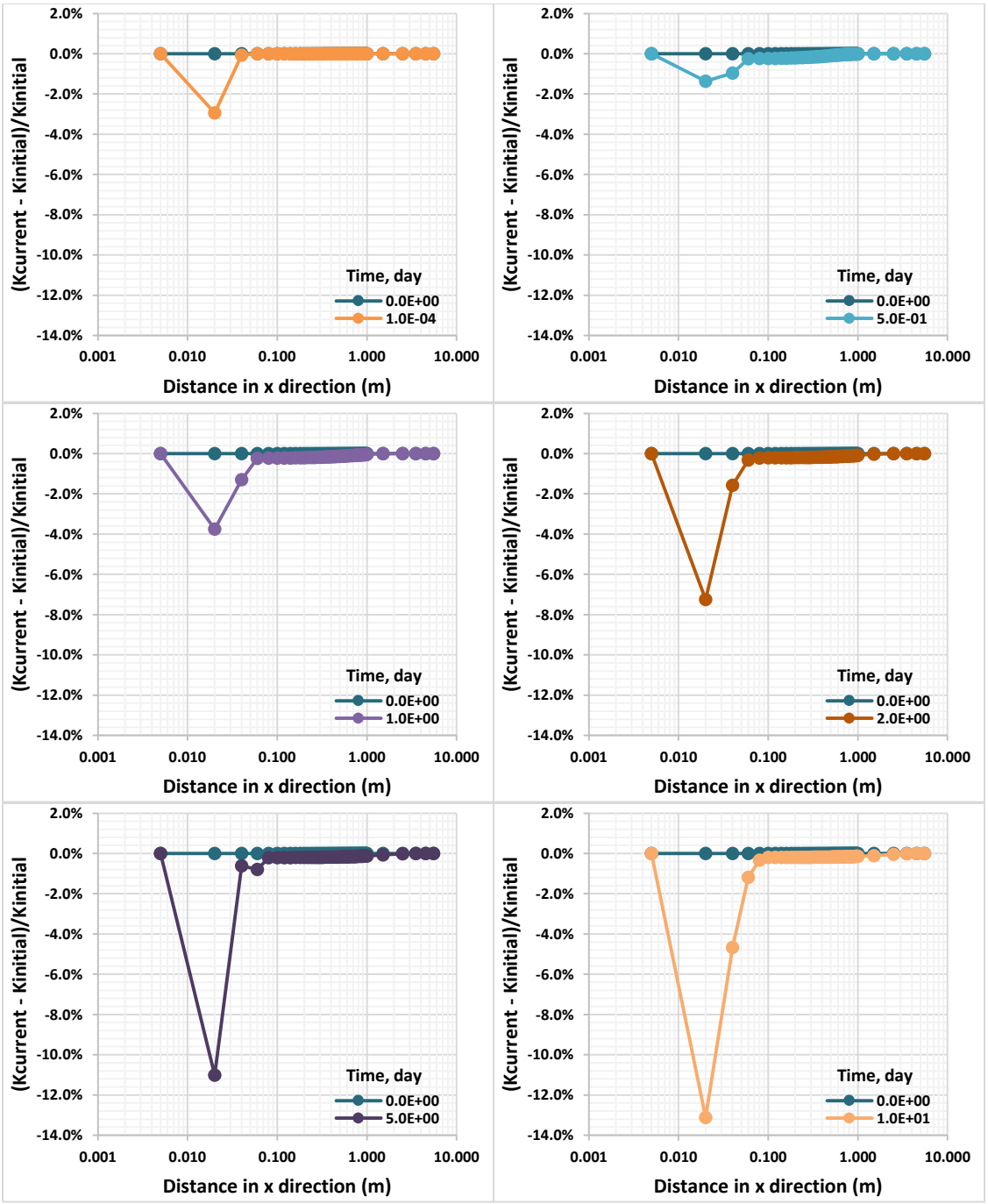

Fig. 58 - Permeability reduction profile at shut-in time 0.0001, 0.5, 1, 2, 5, and 10 days for case with initial mean stress of 6,000 psi and CEC = 5 meq/100g.

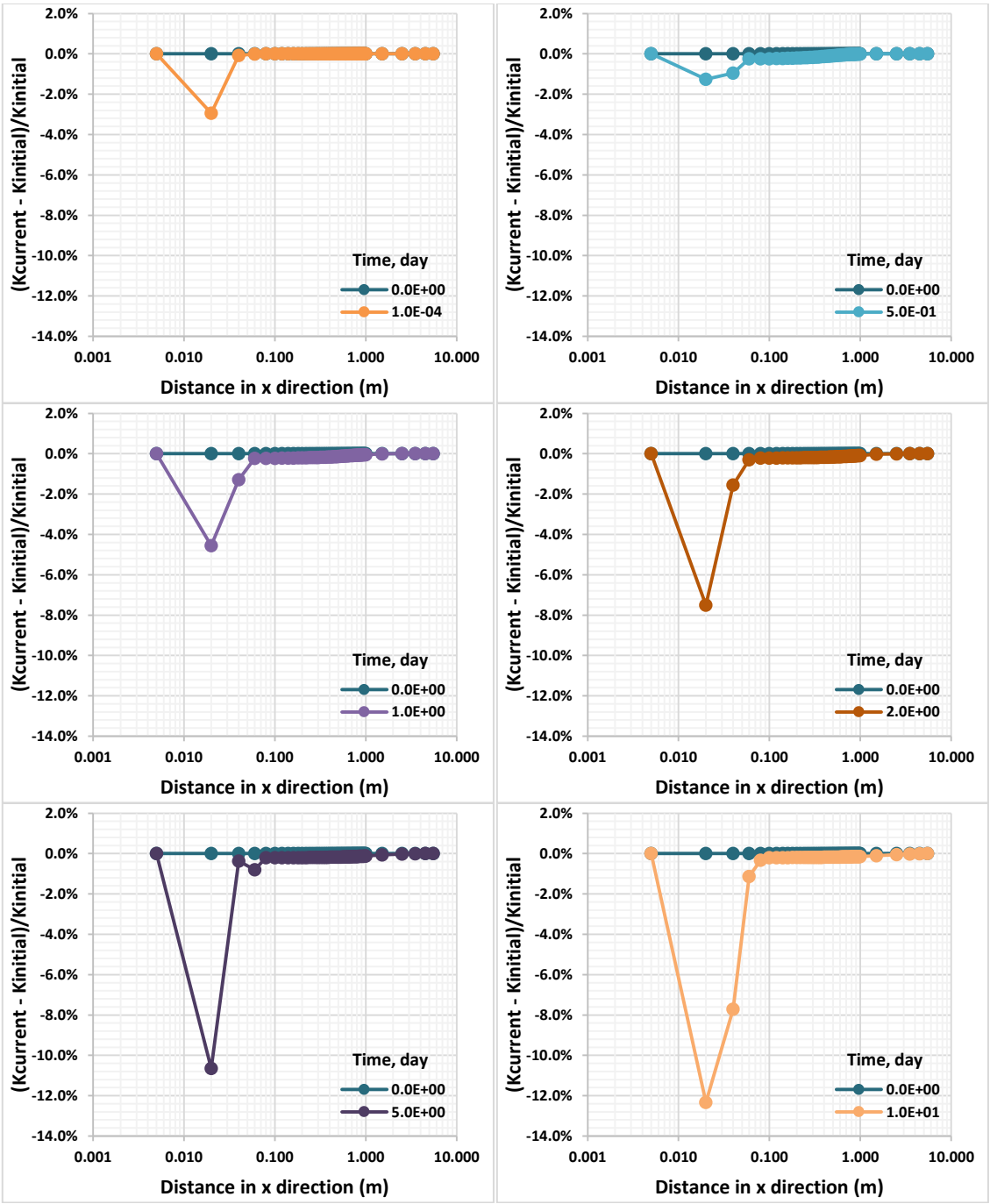

Fig. 59 - Permeability reduction profile at shut-in time 0.0001, 0.5, 1, 2, 5, and 10 days for case with initial mean stress of 6,000 psi and CEC = 40 meq/100g.

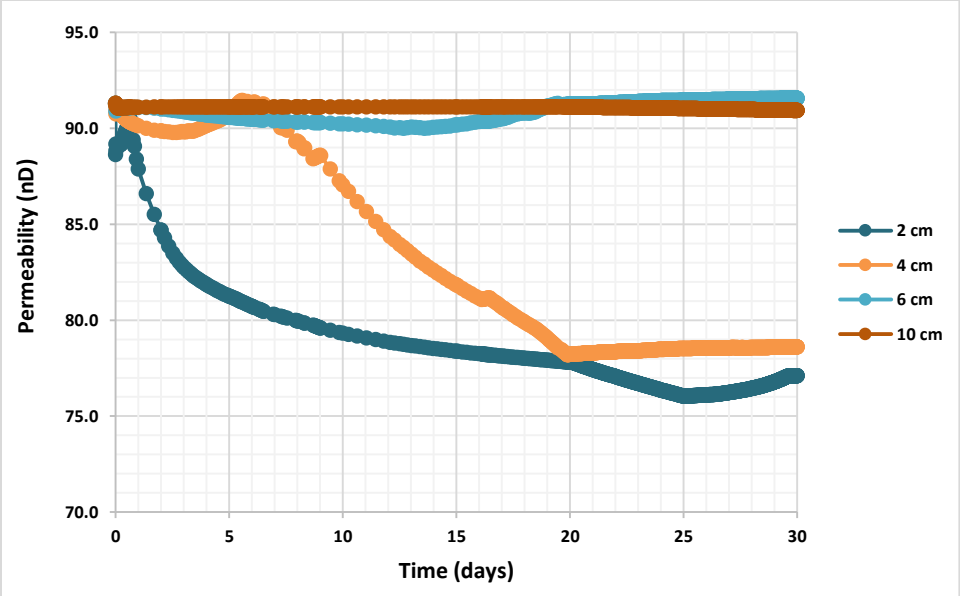

Fig. 60 - Permeability reduction history for elements at 2, 4, 6 and 10 cm from fracture during 30 days of shut-in for case with initial mean stress of 6,000 psi and CEC = 5 meq/100g.

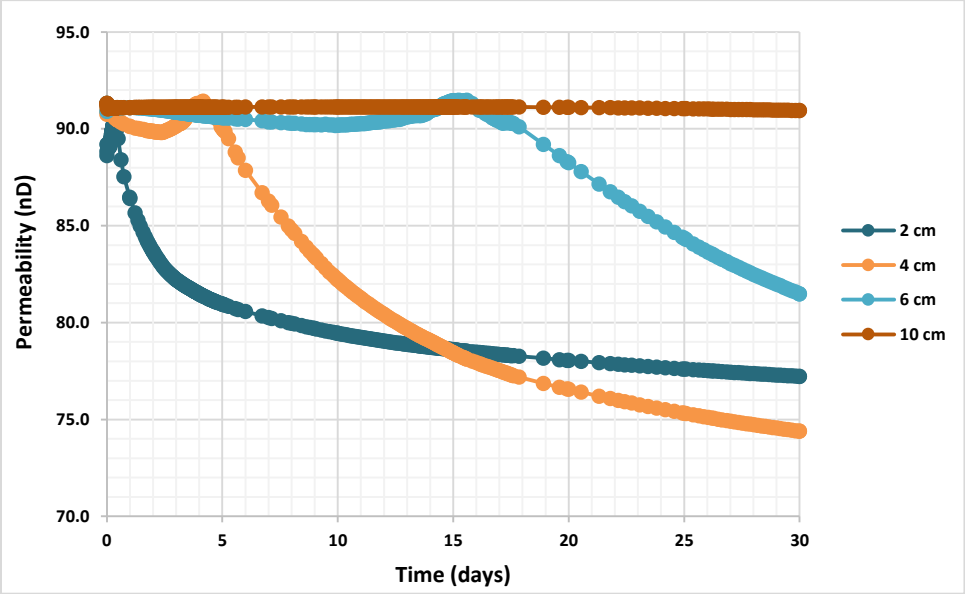

Fig. 61 - Permeability reduction history for elements at 2, 4, 6 and 10 cm from fracture during 30 days of shut-in for case with initial mean stress of 6,000 psi and CEC = 80 meq/100g.

5.5.5. Effect of Clay Porosity on Clay-pore Pressure

At high stress environment, we may find lower clay porosity value. To see the effect of lower clay porosity, in this subsection I present simulation results using a clay porosity of 0.05 instead of 0.1 for the case with an initial mean stress of 12,000 psi and a CEC of 80 meq/100g. The predicted clay-membrane efficiency values, as expected, are higher in the range of 94.2% to 96.2% as shown in Fig. 62 compare to those using clay porosity of 0.1 with the range of 88% to 92% as previously shown in Fig. 41. Hence, I expect higher clay-pore pressure with the lower clay porosity. As shown in Fig. 63, at 10 days shut-in, the clay-pore pressure at the fracture-face is 4,380 psi compared to the case using higher porosity, 0.1, the clay-pore pressure is 4,320 psi as shown in Fig. 49.

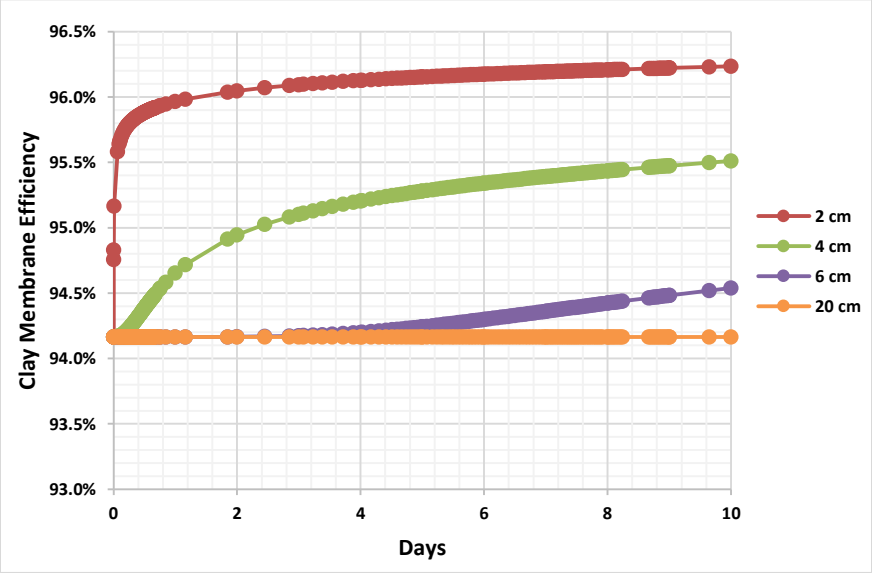

Fig. 62 - Clay membrane efficiency profile for the matrix elements at 2, 4, 6 and 20 cm from the fracture element at shut-in time 0 to 10 days for case with initial mean stress of 12,000 psi and CEC = 80 meq/100g. For this simulation, lower clay-porosity of 0.05 is used. Higher clay-membrane efficiency is observed when using the clay-porosity of 0.05 than of 0.1.

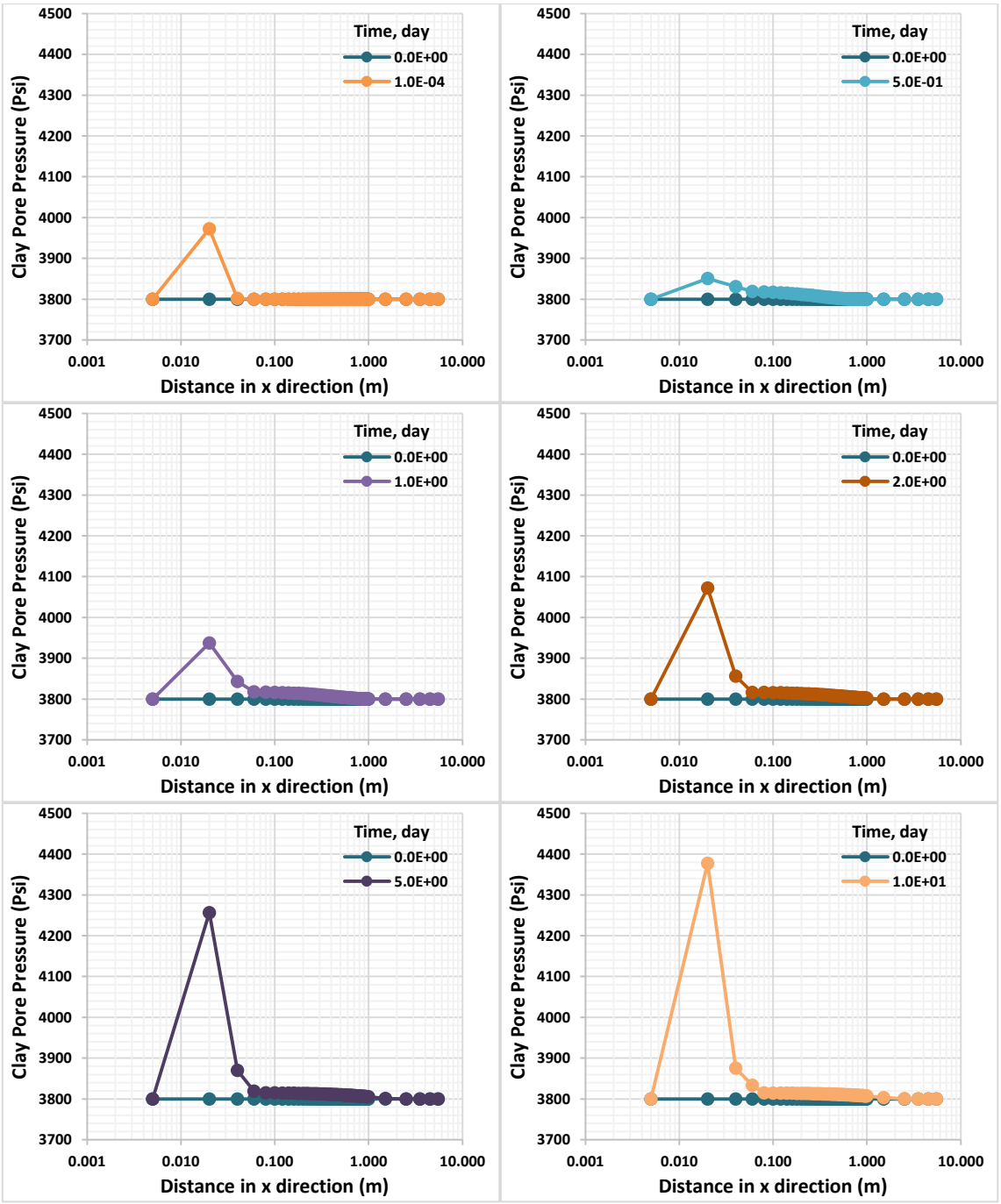

Fig. 63 - Clay-pore pressure distribution at shut-in time 0.0001, 0.5, 1, 2, 5, and 10 days for case with initial mean stress of 12000 psi and CEC = 80 meq/100g. For this simulation, lower clay-porosity of 0.05 is used. Higher clay-pore pressure is observed when using the clay-porosity of 0.05 than of 0.1.

5.5.6. Effect of Salt Concentration on Clay-pore Pressure

To see the effect of salt concentration, in this subsection I present simulation results using a salt mass fraction of 0.15 in the clay pores instead of 0.1 for the case with an initial mean stress of 12,000 psi and a CEC of 80 meq/100g. The clay-membrane efficiency values as expected from Eq. 105 is lower, range from 81.5% to 88.2% as shown in Fig. 64 compare to those using salt mass fraction of 0.1 that range from 88% to 92% as shown in Fig. 41. Hence, I expect lower clay-pore pressure increase because of the lower clay-membrane efficiency. However, due to higher salt concentration in the clay pore, higher clay-pore pressure occur. As shown in Fig. 65, at shut-in of 10 days, the clay-pore pressure at fracture-face is 4,430 psi compare to the case using higher porosity, 0.1, the clay-pore pressure is 4,320 psi as shown in Fig. 49.

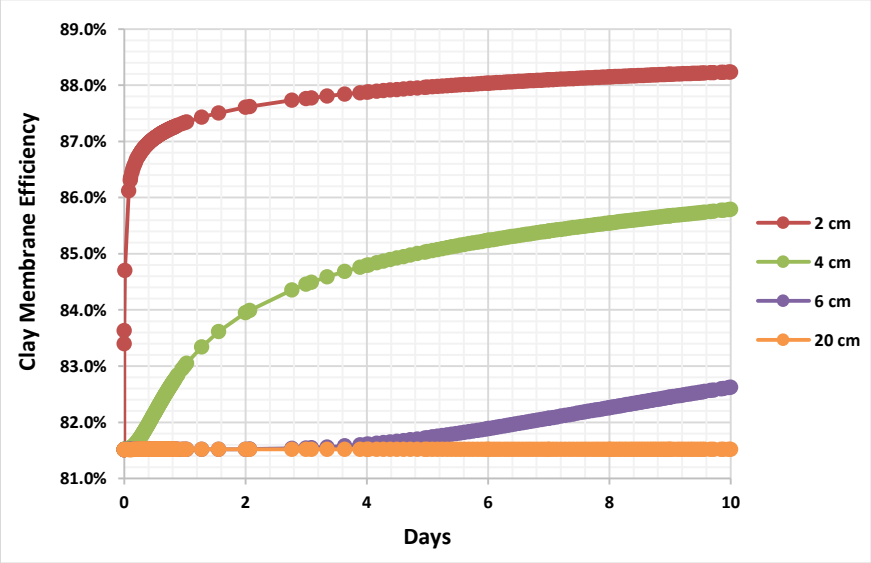

Fig. 64 - Clay membrane efficiency profile for the matrix elements at 2, 4, 6 and 20 cm from the fracture element at shut-in time 0 to 10 days for case with initial mean stress of 12,000 psi and CEC = 80 meq/100g. For this simulation, higher salt mass fraction of 0.15 is used. Lower clay-membrane efficiency is observed when using salt mass fraction of 0.15 than of 0.1.

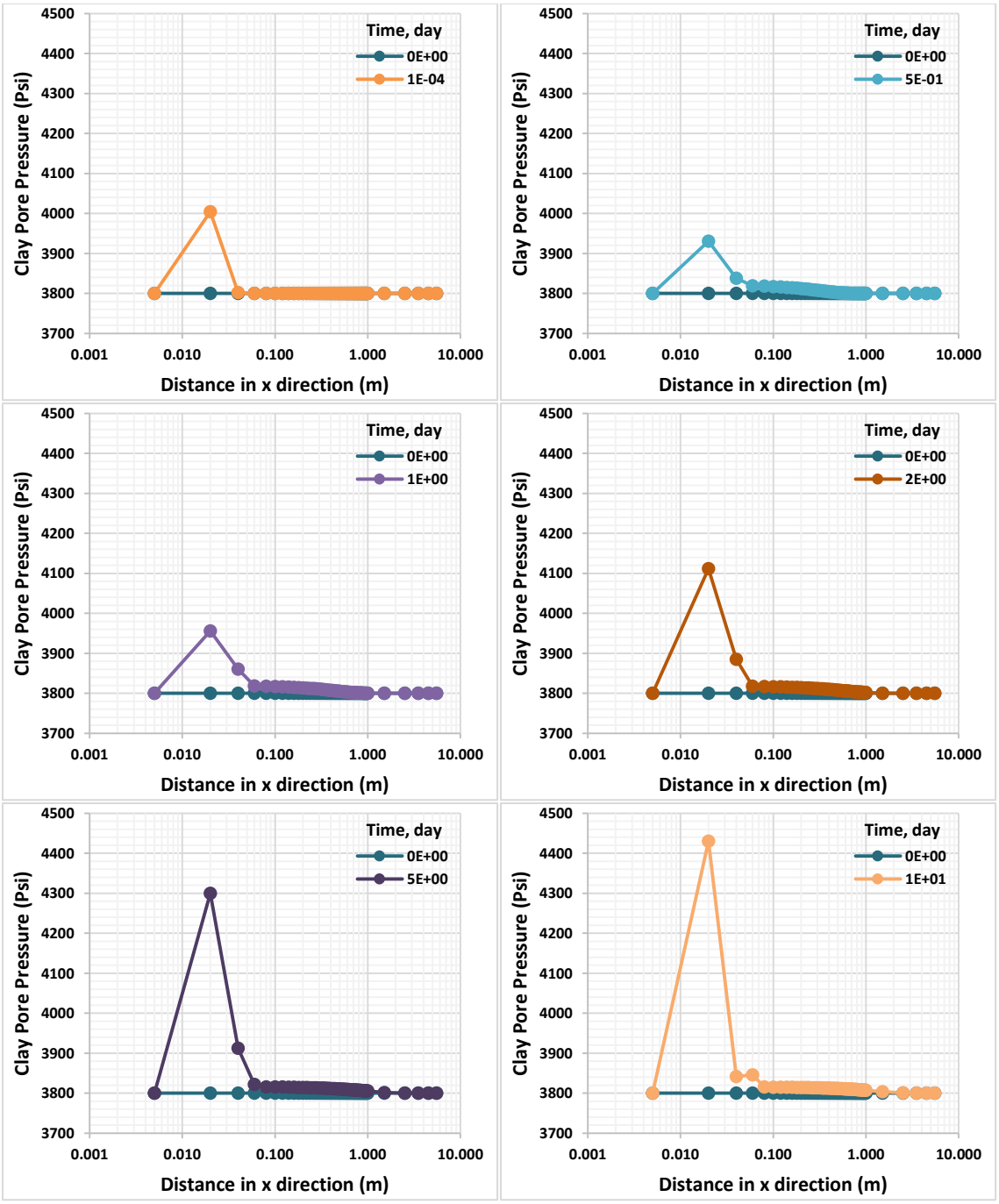

Fig. 65 - Clay-pore pressure distribution at shut-in time 0.0001, 0.5, 1, 2, 5, and 10 days for case with initial mean stress of 12000 psi and CEC = 80 meq/100g. For this simulation, higher salt mass fraction of 0.15 is used. Higher clay-pore pressure is observed when using salt mass fraction of 0.15 than of 0.1.

5.5.7. Tensile Fracturing Analysis

In this subsection, we analyze the possibility of inducing microfractures during shut-in time under overburden stress using the criteria previously presented by Ozkaya (1988). This model considers a pore with elliptical cross-section in the plane of principle stress and least stress and it has a width of *w* and a height of *h* (Fig. 66). Lateral tensile fracturing may occur at point A and a vertical tensile fracturing at point B as functions of existing stresses, pore pressure, as well as the tensile strength and pore cross-section geometry of the shale matrix.

The criteria for lateral fracturing can be written as follows (Özkaya, 1988):

$$P_p\left(\frac{2w}{h}-1\right) > \sigma_{OB}\left(1+\frac{2w}{h}\right)-\sigma_H+T \qquad (\ 114\ )$$

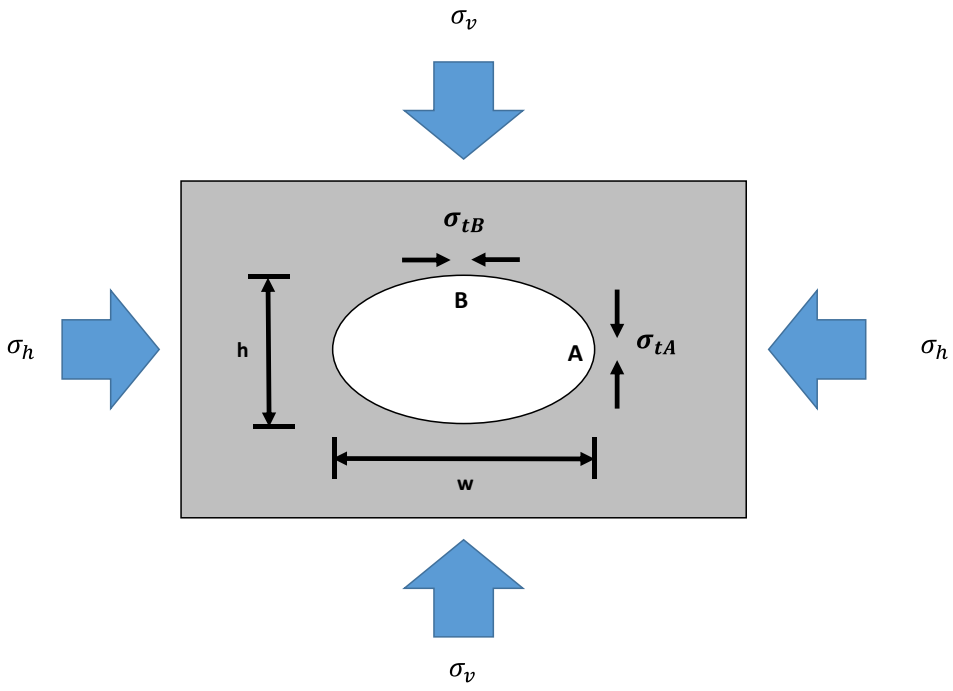

Fig. 66 - A pore with elliptical cross-section in subsurface experiencing overburden and horizontal stresses, adapted from Ozkaya (1988). σ_{tA} and σ_{tB} are tangential stresses at point A and B, respectively.

The criteria for vertical fracturing can be written as follows (Özkaya, 1988):

$$P_p\left(\frac{2h}{w}-1\right) > \sigma_H\left(1+\frac{2h}{w}\right) - \sigma_{OB} + T \qquad (115)$$

When $w = h$, the criteria for lateral and vertical fracturing are as follows:

$$P_p > 3\sigma_{OB} - \sigma_H + T \qquad (116)$$

$$P_p > 3\sigma_H - \sigma_{OB} + T \qquad (117)$$

where,

T is the tensile strength of the rock

w is the width of pore cross-section

h is the height of pore cross-section

Shale formations present anisotropic characteristics in mechanical properties, including the tensile strength due to their layering and pre-existing natural fractures (Mokhtari et al., 2014). For example, Eagle Ford shale samples have varied tensile strength values from 49 up to 593 psi (Mokhtari et al., 2014). However, in this analysis, I consider that the shale formation has isotropic characteristics. The tensile strength of 0 and 145 psi was used to show the lowest and fair pore pressure requirement at the corresponding mean stress. Fig. 67 and Fig. 68 shows lateral and vertical tensile fracturing conditions for tensile strength 0 and 145 psi for varied pore geometry. These plots show the magnitude of pore pressure required for lateral or vertical tensile fracturing to occur at the corresponding mean stress. When the ratio of width to height of the pore cross-section is equal to 1.0, the tensile fracturing condition, i.e. the pore pressure is the highest.

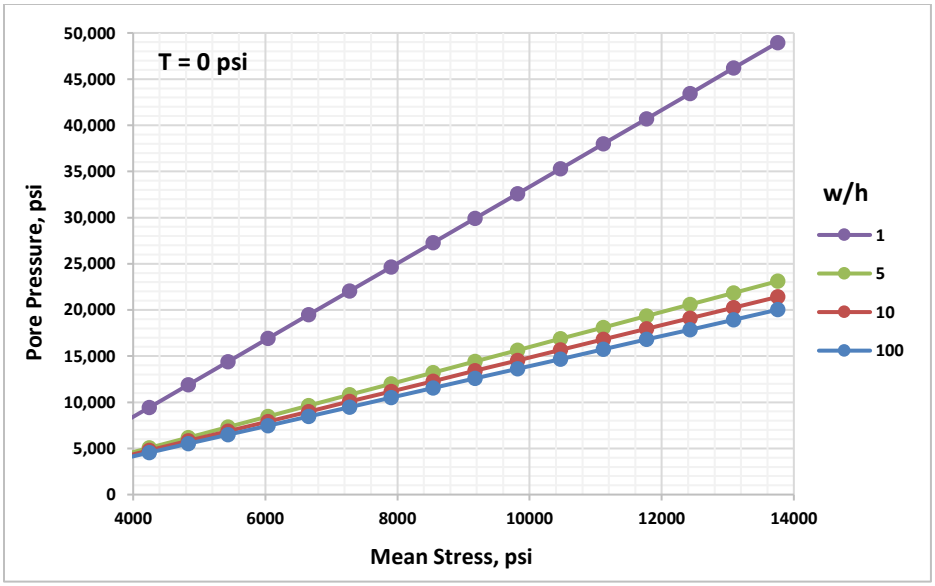

(a)

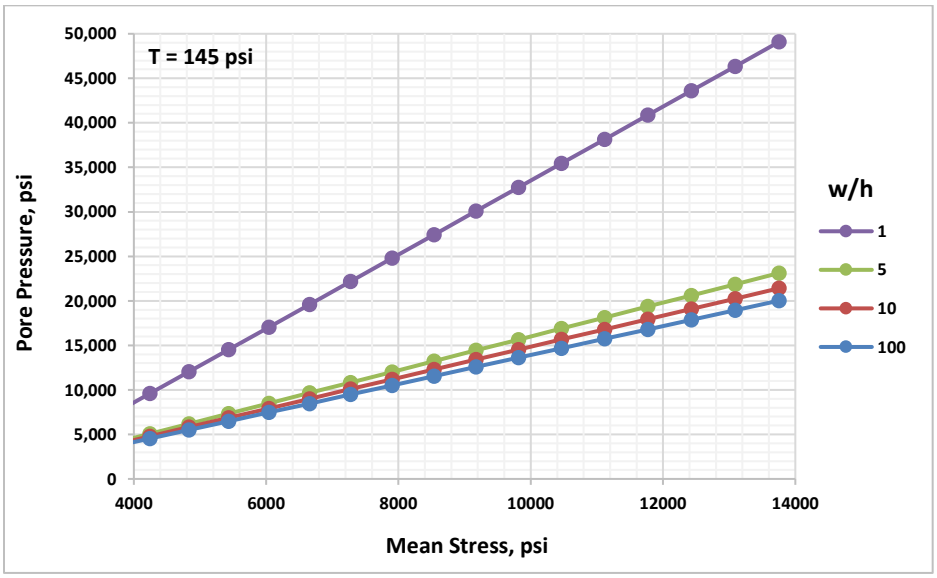

(b)

Fig. 67 - Lateral tensile fracturing conditions at the corresponding mean stress: (a) pore pressure required for tensile strength of 0 psi; (b) pore pressure required for tensile strength of 145 psi.

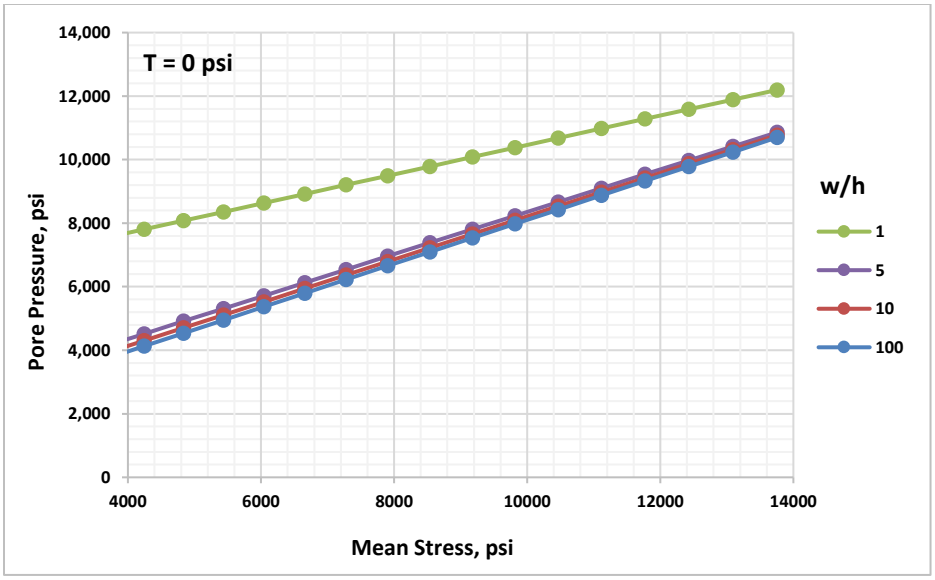

(a)

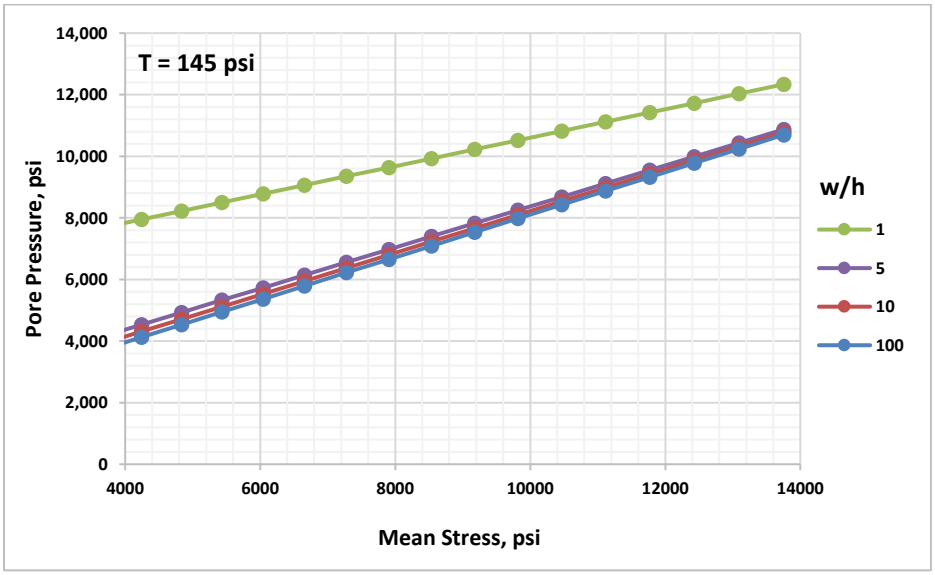

(b)

Fig. 68 - Vertical tensile fracturing conditions at the corresponding mean stress: (a) pore pressure required for tensile strength of 0 psi; (b) pore pressure required for tensile strength of 145 psi.

I analyzed the possibility of tensile fracturing for the case of CEC of 80 meq/100g at depth 8,000 ft. where the overburden, horizontal and mean stress values are approximately 7422, 5352 and 6000 psi, respectively. The pore pressure required for lateral tensile fracturing to occur at that depth is 7,470 psi, assuming shale tensile strength of 0 psi and the ratio of width to height of the pore cross-section of 100 (Fig. 67). Therefore, lateral tensile fracturing does not occur for the case with initial mean stress of 6,000 psi and CEC of 80 meq/100g after shut-in of 30 days (Fig. 69). The pore pressure required for vertical tensile fracturing to occur at that depth is 5,369 psi, assuming shale tensile strength of 0 psi and the ratio of height to width of the pore cross-section of 100 (Fig. 68). Therefore, vertical tensile fracturing does not occur for the case with initial mean stress of 6,000 psi and CEC of 80 meq/100g after shut-in of 30 days (Fig. 70). For this case, given a lower clay-pore pressure at higher overburden stress, the tensile fracturing does not to occur at depth higher than 8,000 ft during shut-in time. Over-pressured formations, however, could overcome the threshold for micro-fracture development.

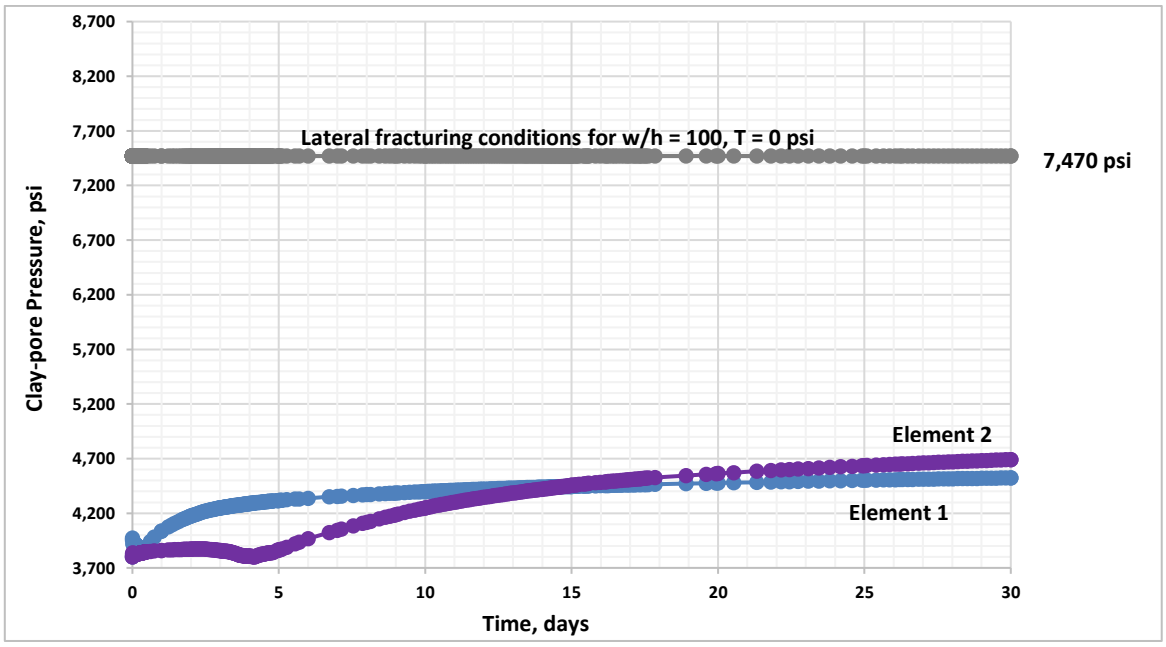

Fig. 69 - Clay-pore pressure evolution during shut-in of 30 days for element 1 (blue curve) and 2 (purple curve), 2 and 4 cm from fracture element. Here, the maximum clay-pore pressure is 4,700 psi at element 2 after shut-in of 30 days, which is lower than the lateral fracturing criteria of 7,470 psi (gray curve).

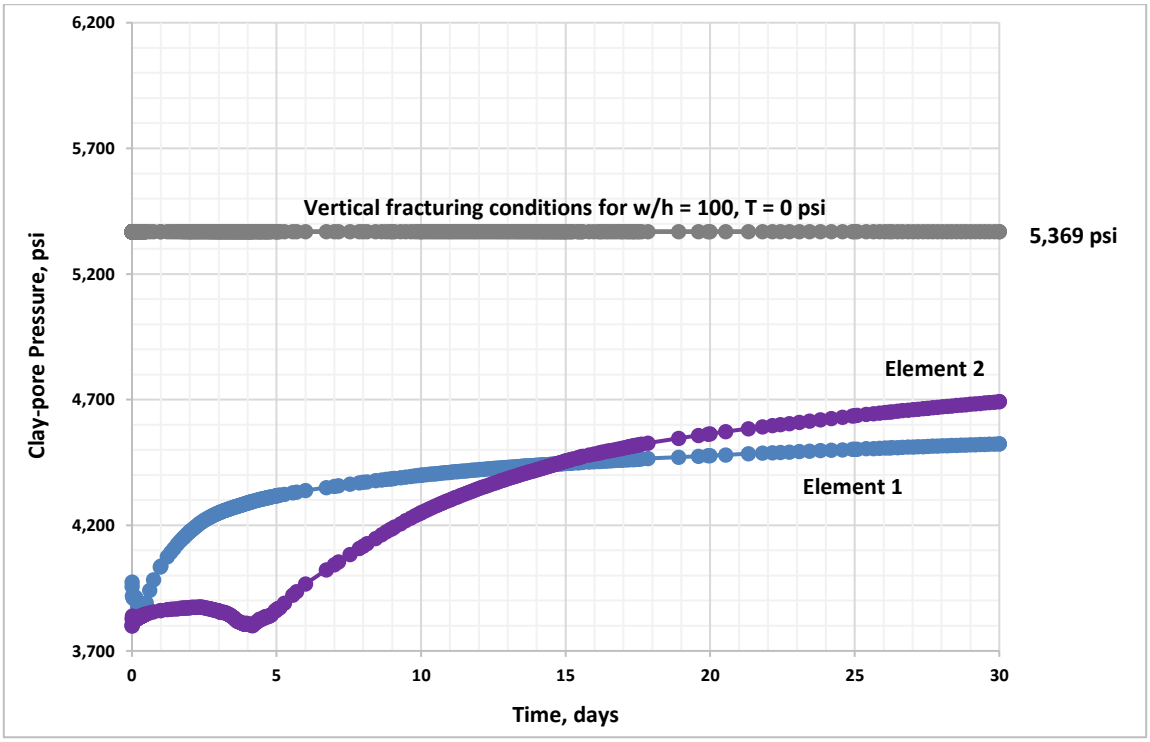

Fig. 70 - Clay-pore pressure evolution during shut-in of 30 days for element 1 (blue curve) and 2 (purple curve), 2 and 4 cm from fracture element. Here, the maximum clay-pore pressure is 4,700 psi at element 2 after shut-in of 30 days, which is lower than the vertical fracturing criteria of 5,369 psi (gray curve).

5.5.8. Effect of Gridblock Size

In this subsection, the effect of gridblock size was investigated. Here, the simulation domain was 0.251 x 0.25 x 0.2 m divided equally into 251 x 1 x 1 in x, y, and z directions. Therefore, each gridblock has the size of 0.001 x 0.25 x 0.2 m. The smaller total length of shale matrix in the x direction, which is 0.25 m, in the case of finer gridblock size, compare to 6 m in the case of coarser gridblock size is to save simulation time. Other simulation parameters were kept the same.

Simulation results show that finer gridblock size results lower slit-pore pressure by fracture-face (Fig. 71). These differences are because of water influx from fracture results higher water saturation when the element volume is lower (Fig. 72). This, in turn, causes lower capillary pressure and lower slit-pore pressure in the case of finer gridblock size. Initially, slit-pore pressure by fracture face is dissipating faster due to lower element volume in the case of finer gridblock size (Fig. 71b). However, slit-pore pressure propagation in the case of coarser gridlock size is faster that it reaches approximately 20 cm from fracture-face at nearly similar time for both gridblock size cases (Fig. 71c).

Initially, clay-pore pressure by fracture-face is higher in the case of coarser grid block size mostly because of higher influx from slit-pore to clay-pore due to higher slit-pore pressure (Fig. 73a). Clay-pore pressure by fracture-face is dissipating earlier in the case of finer gridblock size (Fig. 73b). Sequentially, higher pressure occurs in clay-pore due to higher osmotic flux into clay-pore caused by lower salt mass fraction in the case of finer gridblock size (Fig. 73c). However, as shut-in time is increasing, the clay-pore pressure is higher in the case of coarser gridblock size due to higher influx from slit-pore to clay-pore, notice that the shape factor in both cases are the same (Fig. 73e and Fig. 73f). Shape factor affect the magnitude of mass transfer between slit-pore and clay-pore, hence the clay-pore pressure magnitude. Since the same value of shape factor is used in both cases, lower mass transfer occurs in the case of finer gridblock size.

It can be concluded that although the trend of the increase of the clay-pore pressure is similar, the appropriate gridblock size and shape factor is required to get the exact values of clay-pore pressure increase with shut-in time. This shows that experimental or field investigation are needed to adjust parameters used in simulation.

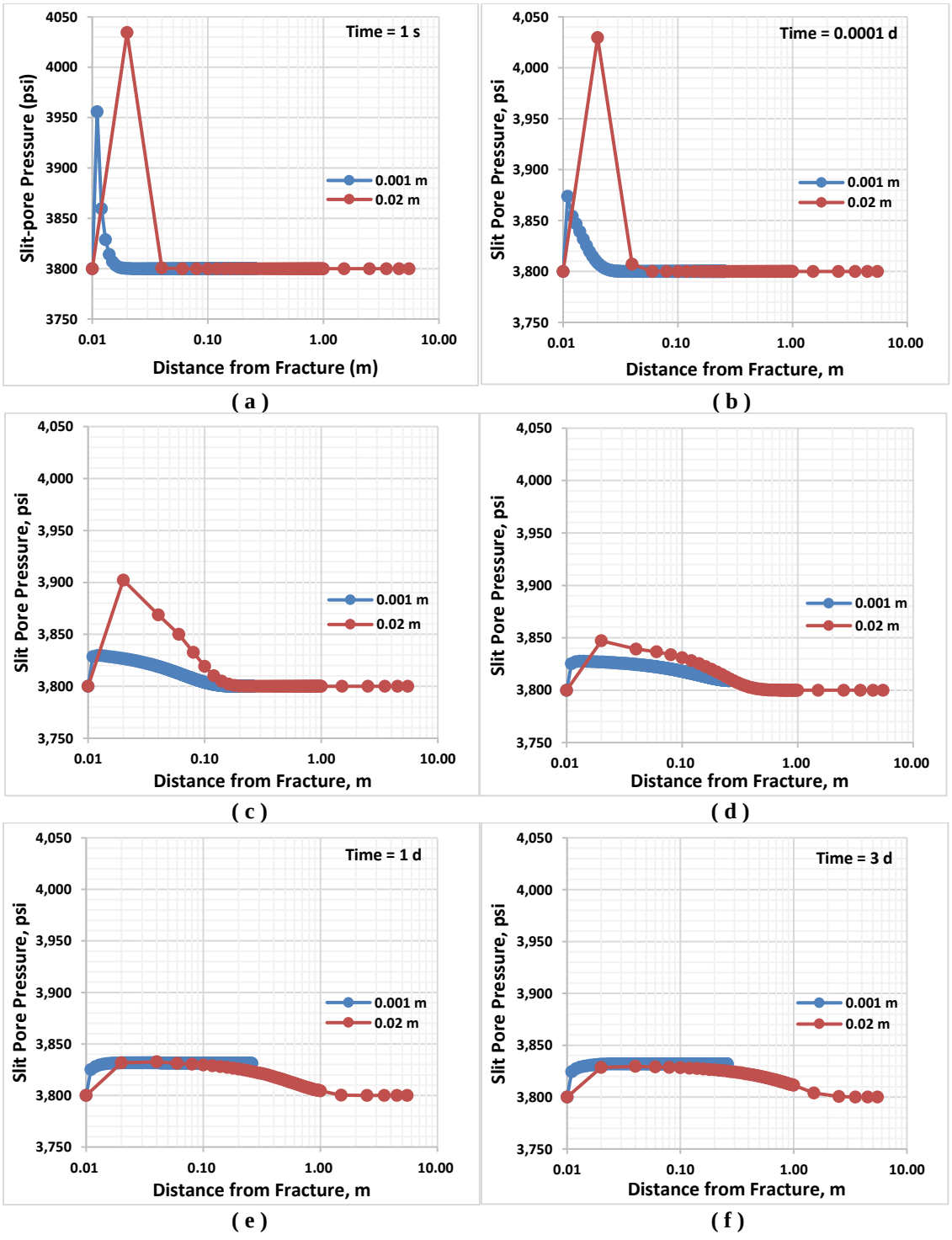

Fig. 71 - Comparison of slit pore pressure using different gridblock size, Δx of 0.001 m and 0.02 m at different shut-in time: (a) 1 s; (b) 0.0001 day; (c) 0.01 day; (d) 0.1 day; (e) 1 day and (f) 3 day.

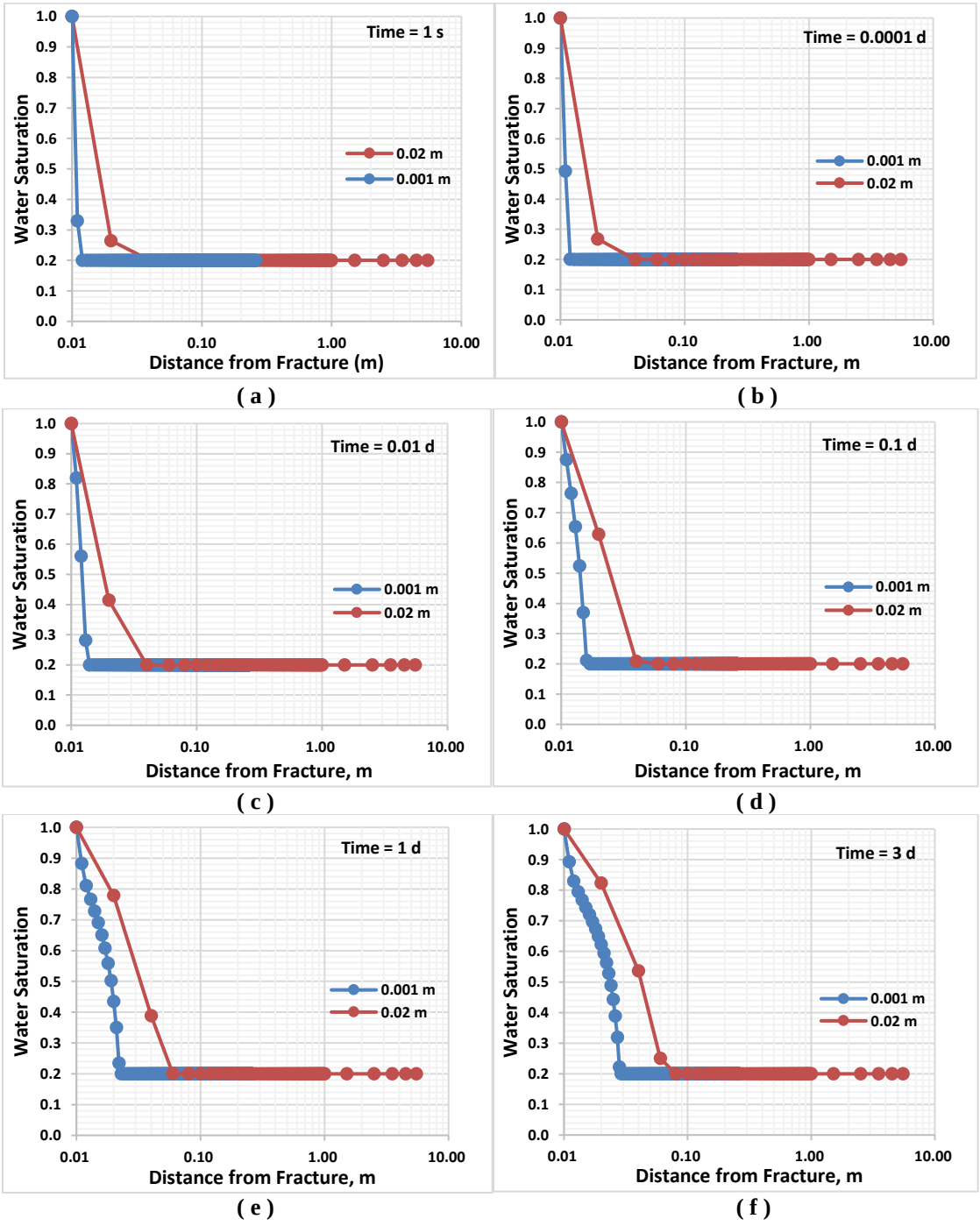

Fig. 72 - Comparison of water saturation using different gridblock size, Δx of 0.001 m and 0.02 m, at different shut-in time: (a) 1 s; (b) 0.0001 day; (c) 0.01 day; (d) 0.1 day; (e) 1 day and (f) 3 day.

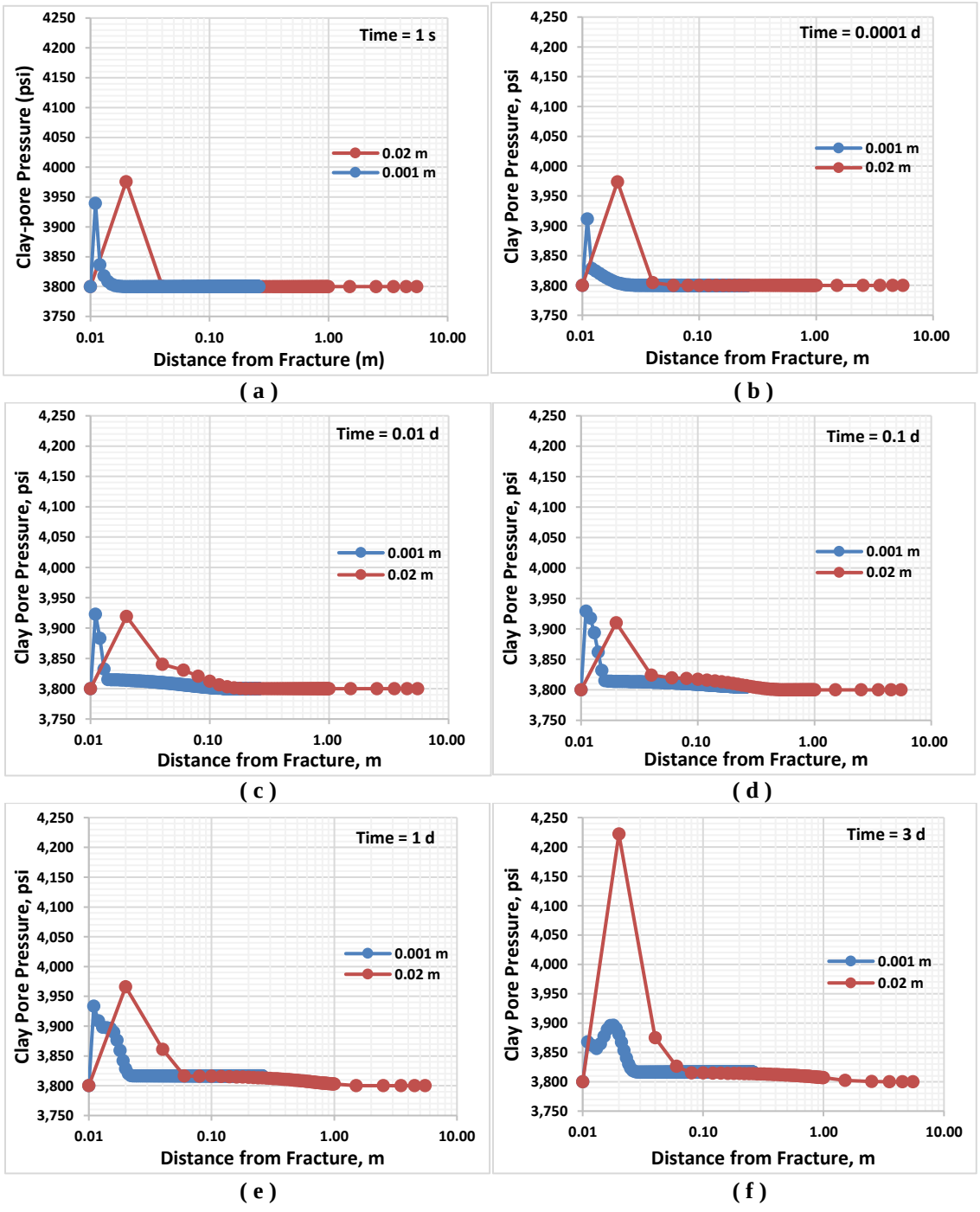

Fig. 73 - Comparison of clay pore pressure using different gridblock size, Δx of 0.001 m and 0.02 m at different shut-in time: (a) 1 s; (b) 0.0001 day; (c) 0.01 day; (d) 0.1 day; (e) 1 day and (f) 3 day.

6. CONCLUSIONS AND RECOMMENDATIONS

A conceptual petrophysical model of shale matrix had been developed to investigate the effects of water imbibition, osmosis and clay swelling to shale permeability during shut-in time and production following hydraulic fracturing a gas shale formation. A new reservoir flow simulator which dynamically accounts for the impact of these mechanisms on the permeability was developed. A new geomechanically fully-coupled reservoir flow simulator was also developed to investigate the impact of these mechanisms on the permeability under stress.

This chapter summarizes main conclusions and observations in this study. Finally, recommendations for future improvements are discussed.

6.1. Conclusions

Simulation study of shut-in periods indicates that due to clay content in shale matrix, shale-water interaction, and salinity difference between the hydraulic-fracturing fluid and the shale matrix water, clay swelling occurs and causes a reduction in shale matrix permeability. More severe damage can occur if fresh water is used as the fracturing fluid. Using 2% KCl in fracturing water does not prevent permeability reduction when the clay-bound water in the shale matrix has high salinity. Continuing shale-water interaction can expand the damage zone further. Simulation results with triple-porosity shale matrix system with varied initial water saturation in slit-shaped pores or microcracks shows, when the shale matrix is at sub-irreducible water saturation levels, the reduction in permeability is more pronounced compared to those at the irreducible water saturation or higher. Simulation of production after shut-in shows that when permeability damage after shut-in is irreversible. This leads to much lower well production performance when compared to the reversible permeability damage case.

Clay-membrane efficiency magnitude is function of CEC value of the clay, mean salt concentration, clay porosity and the existing stress field. The efficiency is higher with higher CEC and mean stress values. On the other hand, it is lower with higher mean salt concentration and higher clay-porosity. Simulation results show that the clay-membrane efficiency increases during the shut-in with the increase in the mean stress and the decrease in the mean salt concentration.

During the shut-in period the clay-pore pressure increases and the associated permeability reduction is affected by the magnitude of clay-membrane efficiency. Hence, they are functions of CEC value of clay, mean salt concentration, clay porosity and stress field. Higher CEC causes higher clay-pore pressure and higher permeability reduction under similar stress field. Lower clay porosity values results in higher clay pore pressure and therefore higher permeability reduction compare to those with higher clay porosity values. On the other hand, salt concentration and mean stress affect the clay pore pressure and the associated permeability reduction in two ways: firstly, by affecting the magnitude of clay-membrane efficiency and, secondly, through the coupled flow and geomechanics. Clearly, higher salt concentration difference between the fracturing water and the formation water results in higher clay-pore pressure and the associated permeability reduction. Higher mean stress can suppress the increase in clay pore pressure.

The permeability of the shale matrix varies with the formation depth due to two mechanisms. First, the permeability decreases with the increase in the effective stress, which is a function of formation depth, i.e. the overburden stress and the pore pressure. Second, the permeability decreases due to additional stress by osmosis and clay-pore pressure buildup, which varies with the overburden stress.

Clay pore pressure increase during shut-in period causes the increase in the existing tensile stresses in the shale matrix. However, it is predicted that the increased stress is insufficient to cause micro-fracturing.

The newly-developed simulator includes additional mechanisms that will allow practicing engineers and earth scientists to gain information on the nature of permeability damage that may occur near fractures faces during shut-in period after hydraulic fracturing. The simulator can give insights for the design of fracturing fluid during the field operations to avoid significant formation damage.

6.2. Recommendations

Experimental work using shale samples currently need to be conducted to measure the clay swelling effect on the formation permeability reduction under stress during shut-in time in order to validate the simulator. One could consider conducting experiments using shale samples with CEC, salt type, salt concentration, under different stress levels, measuring permeability, water saturation, salt concentration, pore pressure and strain at different shut-in time. One then can optimize the simulation parameters based on the experimental data to obtain accurate permeability alteration prediction.

REFERENCES

Aksu, I., E. Bazilevskaya, Z. T. Karpyn. 2015. Swelling of clay minerals in unconsolidated porous media and its impact on permeability. *GeoResJ* **7**: 1-13.

Arthur, J. D., B. Bohm, B. J. Coughlin et al. 2008. Hydraulic fracturing considerations for natural gas wells of the Fayetteville Shale. *ALL Consulting*.

Asef, M., M. Farrokhrouz. 2013. *Shale engineering: Mechanics and mechanisms*, CRC Press (Reprint).

Bader, S., H. Kooi. 2005. Modelling of solute and water transport in semi-permeable clay membranes: comparison with experiments. *Advances in water resources* **28** (3): 203-214.

Bertoncello, A., J. Wallace, C. Blyton et al. 2014. Imbibition and Water Blockage In Unconventional Reservoirs: Well-Management Implications During Flowback and Early Production. *SPE Reservoir Evaluation and Engineering* **17** (04): 497 - 506. SPE-167698-PA.

Bostrom, N., M. Chertov, M. Pagels et al. 2014. The Time-Dependent Permeability Damage Caused by Fracture Fluid. Presented at the SPE International Symposium and Exhibition on Formation Damage Control, 26-28 February 2014, Lafayette, Louisiana, USA.

Chakraborty, N., Z. Karpyn, S. Liu et al. 2017. Permeability evolution of shale during spontaneous imbibition. *Journal of Natural Gas Science and Engineering*.

Chalmers, G. R., R. M. Bustin, I. M. Power. 2012. Characterization of gas shale pore systems by porosimetry, pycnometry, surface area, and field emission scanning electron microscopy/transmission electron microscopy image analyses: Examples from the Barnett, Woodford, Haynesville, Marcellus, and Doig units. *AAPG bulletin* **96** (6): 1099-1119.

Chenevert, M. E. 1970. Shale alteration by water adsorption. *Journal of petroleum technology* **22** (09): 1141-1148. SPE-2401-PA.

Chenevert, M. E., A. K. Sharma. 1993. Permeability and Effective Pore Pressure of Shales. *SPE Drilling & Completion* **8** (01): 28 - 34. SPE-21918-PA.

Constant, D. W., A. Bourgoyne Jr. 1988. Fracture-gradient prediction for offshore wells. *SPE drilling engineering* **3** (02): 136-140.

Corey, A. T. 1954. The interrelation between gas and oil relative permeabilities. *Producers monthly* **19** (1): 38-41.

Curtis, J. B. 2002. Fractured shale-gas systems. *AAPG bulletin* **86** (11): 1921-1938.

Darley, H. C., G. R. Gray. 1988. *Composition and properties of drilling and completion fluids*, Gulf Professional Publishing (Reprint).

Dean, R. H., X. Gai, C. M. Stone et al. 2006. A comparison of techniques for coupling porous flow and geomechanics. *Spe Journal* **11** (01): 132-140.

Dehghanpour, H., Q. Lan, Y. Saeed et al. 2013. Spontaneous Imbibition of Brine and Oil in Gas Shales: Effect of Water Adsorption and Resulting Microfractures. *Energy & Fuels* **27** (6): 3039-3049.

Ehlig-Economides, C. A., M. J. Economides. Water as proppant. Society of Petroleum Engineers.

Engelder, T., L. M. Cathles, L. T. Bryndzia. 2014. The fate of residual treatment water in gas shale. *Journal of Unconventional Oil and Gas Resources* **7**: 33-48.

Fakcharoenphol, P., B. Kurtoglu, H. Kazemi et al. 2014. The Effect of Osmotic Pressure on Improve Oil Recovery from Fractured Shale Formations. Presented at the SPE Unconventional Resources Conference, 1-3 April, The Woodlands, Texas, USA.

Fakcharoenphol, P., Y. Xiong, L. Hu et al. 2013. User's Guide of TOUGH2-EGS. A Coupled Geomechanical and Reactive Geochemical Simulator for Fluid and Heat Flow in Enhanced Geothermal Systems Version 1.0, Colorado School of Mines, Golden, CO (United States).

Fan, L., J. W. Thompson, J. R. Robinson. 2010. Understanding Gas Production Mechanism and Effectiveness of Well Stimulation in the Haynesville Shale Through Reservoir Simulation. Presented at the Canadian Unconventional Resources and International Petroleum Conference, Calgary, 19-21 October 2010. SPE-136696-MS.

Fisher, M. K., C. A. Wright, B. M. Davidson et al. 2005. Integrating Fracture Mapping Technologies To Improve Stimulations in the Barnett Shale. *SPE Production & Facilities* **20** (02): 85-93.

Fjar, E., R. M. Holt, A. Raaen et al. 2008. *Petroleum related rock mechanics*, Vol. 53, Elsevier (Reprint).

Gangi, A. F. Variation of whole and fractured porous rock permeability with confining pressure. Vol. 15, 249-257: Elsevier.

Gdanski, R. D., D. D. Fulton, C. Shen. 2009. Fracture-Face-Skin Evolution During Cleanup. *SPE Production & Operations* **24** (01).

Grim, R. E. 1968. *Clay mineralogy*, McGraw-Hill (Reprint).

Heller, R., J. Vermylen, M. Zoback. 2014. Experimental investigation of matrix permeability of gas shales. *AAPG bulletin* **98** (5): 975-995.

Jaeger, J., N. Cook, R. Zimmermann. 2007. Fundamentals of rock mechanics, edited by Chapman and Hall. *New York, United States of America*: 1-593.

Keijzer, T. J. S. 2000. Chemical osmosis in natural clayey materials. 196 Ph.D. Dissertation, Utrecht University.

Lal, M. 1999. Shale stability: drilling fluid interaction and shale strength. Presented at the SPE Asia Pacific Oil and Gas Conference and Exhibition, 20-22 April, Jakarta, Indonesia.

Leverett, M. 1941. Capillary behavior in porous solids. *Transactions of the AIME* **142** (01): 152-169.

Li, K., R. N. Horne. 2006. Comparison of methods to calculate relative permeability from capillary pressure in consolidated water-wet porous media. *Water resources research* **42** (6).

Madsen, F. T., M. Müller-Vonmoos. 1989. The swelling behaviour of clays. *Applied Clay Science* **4** (2): 143-156.

Marine, I. W., S. J. Fritz. 1981. Osmotic model to explain anomalous hydraulic heads. *Water Resources Research* **17** (1): 73-82.

Mayerhofer, M. J., E. Lolon, N. R. Warpinski et al. 2010. What is stimulated reservoir volume? *SPE Production & Operations* **25** (01): 89-98.

Medved, I., R. Černý. 2013. Osmosis in porous media: A review of recent studies. *Microporous and Mesoporous Materials* **170**: 299-317.

Mokhtari, M., B. T. Bui, A. N. Tutuncu. 2014. Tensile Failure of Shales: Impacts of Layering and Natural Fractures. Presented at the SPE Western North American and Rocky Mountain Joint Meeting, 17-18 April, Denver, Colorado.

Moridis, G. 2014. User's Manual of the TOUGH+ Core Code v1. 5: A General-Purpose Simulator of Non-Isothermal Flow and Transport through Porous and Fractured Media. Report No. LBNL-6871E, Ernest Orlando Lawrence Berkeley National Laboratory, Berkeley, CA (US).

Moridis, G. J., C. M. Freeman. 2014. The RealGas and RealGasH2O options of the TOUGH+ code for the simulation of coupled fluid and heat flow in tight/shale gas systems. *Computers & Geosciences* **65**: 56-71.

Narasimhan, T., P. Witherspoon. 1976. An integrated finite difference method for analyzing fluid flow. *Water Resources Research* **12**: 57-64.

Özkaya, I. 1988. A simple analysis of oil-induced fracturing in sedimentary rocks. *Marine and Petroleum Geology* **5** (3): 293-297.

Pagels, M., J. J. Hinkel, D. M. Willberg. Measuring capillary pressure tells more than pretty pictures. Society of Petroleum Engineers.

Palisch, T. T., M. Vincent, P. J. Handren. 2010. Slickwater fracturing: food for thought. *SPE Production & Operations* **25** (03): 327-344.

Potter, P. E., J. B. Maynard, W. A. Pryor. 1980. *Sedimentology of shale.*, Softcover reprint of the hardcover 1st edition 1980 edition. New York, Springer-Verlag (Reprint).

Pruess, K., C. Oldenburg, G. Moridis. 1999. TOUGH2 user's guide version 2. *Lawrence Berkeley National Laboratory*.

Rahman, M. M., Z. Chen, S. S. Rahman. 2005. Experimental Investigation of Shale Membrane Behavior Under Tri-Axial Condition. *Petroleum Science and Technology* **23** (9-10): 1265-1282.

Rice, J. 1998. Elasticity of fluid-infiltrated porous solids (poroelasticity). *Stress* **2** (2).

Rutqvist, J., C.-F. Tsang. 2002. A study of caprock hydromechanical changes associated with CO 2-injection into a brine formation. *Environmental Geology* **42** (2): 296-305.

Sun, X., K. Mohanty. Simulation of methane hydrate reservoirs, SPE 93015. Vol. 31.

van Oort, E. 2003. On the physical and chemical stability of shales. *Journal of Petroleum Science and Engineering* **38** (3–4): 213-235.

Wagner, W., J. Cooper, A. Dittmann et al. 2000. The IAPWS industrial formulation 1997 for the thermodynamic properties of water and steam. *Journal of engineering for gas turbines and power* **122** (1): 150-184.

Wang, M., J. Y. Leung. 2016. Numerical Investigation of Coupling Multiphase Flow and Geomechanical Effects on Water Loss During Hydraulic-Fracturing Flowback Operation. *SPE Reservoir Evaluation & Engineering*. SPE-178618-PA.

Warpinski, N. R., M. J. Mayerhofer, M. C. Vincent et al. 2009. Stimulating unconventional reservoirs: maximizing network growth while optimizing fracture conductivity. *Journal of Canadian Petroleum Technology* **48** (10): 39-51.

Wasaki, A., I. Y. Akkutlu. 2015. Permeability of Organic-Rich Shale. *SPE Journal* **20** (06): 1384 - 1396. SPE-170830-PA.

Watson, D., T. Brittenham, P. L. Moore. 2003. *Advanced well control*, Vol. 10, Society of Petroleum Engineers (Reprint).

Winterfeld, P. H., Y.-S. Wu. 2016. Simulation of Coupled Thermal/Hydrological/Mechanical Phenomena in Porous Media. *SPE Journal* **21** (03): 1,041 - 1,049. SPE-173210-PA.

Yan, Q., C. Lemanski, Z. T. Karpyn et al. 2015. Experimental investigation of shale gas production impairment due to fracturing fluid migration during shut-in time. *Journal of Natural Gas Science and Engineering* **24**: 99-105.

APPENDIX A

This appendix details the derivation of the geomechanics equation used in the coupled flow and geomechanics formulation. First, we describe the derivation of the constitutive geomechanics equation based on the poroelasticity theory derived by Jaeger et al, 2007 and then extend to thermoporoelastic behavior. Second, we describe the derivation of the governing geomechanical (Fakcharoenphol et al., 2013).

A.1 Derivation of the thermoporoelastic constitutive equation relating stress and strain

In this part, first, we describe the derivation of the poroelastic equation by Jaeger et al, 2007. The poroelastic behavior of rocks can be constructed by a conceptual model of a rock as a connected mineral phase permeated with voids which may be interconnected, or may exist as isolated vugs (Jaeger et al., 2007). The isolated vugs are ignored in this model because they do not contribute to fluid flow process. Here, the macroscopic bulk volume of the rock (V_b) is the summation of the volume occupied by the solid mineral (V_m) and the volume occupied by the pore space (V_p), as illustrated in Fig. 74a. The solid mineral phase of the rock is often referred to as the matrix.

$$V_b = V_m + V_p \qquad (\text{A.1})$$

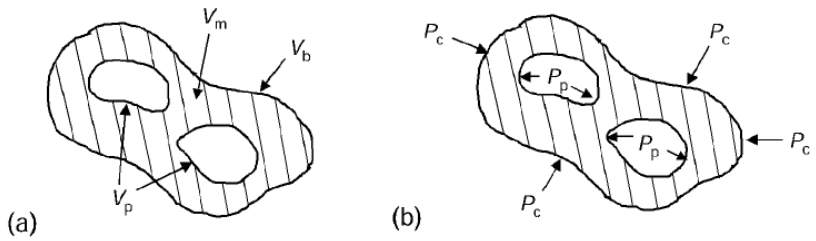

Fig. 74 - Porous rock, showing (a) the bulk volume (V_b), pore volume (V_p) and mineral/matrix volume (V_m); (b) the pore pressure (P_p) and confining pressure (P_c). Reprinted from Jaeger et al. (2007).

If the porous rock is externally subjected to a normal traction of magnitude P_c where subscript *c* denotes confining pressure, and the internal pore walls are subjected to a pore pressure of magnitude P_p, exerted by pore fluid (Fig. 74b), then there are two independent pressure act on the rock and two independent volumes, which are V_b and V_p. The bulk and pore strain increments can be expressed in terms of the four porous rock compressibility (C_{bc}, C_{bp}, C_{pc} and C_{pp}) as follows:

$$d\varepsilon_b = \frac{-dV_b}{V_b^i} = C_{bc}dP_c - C_{bp}dP_p \qquad (\text{A.2})$$

$$d\varepsilon_p = \frac{-dV_p}{V_p^i} = C_{pc}dP_c - C_{pp}dP_p \qquad (\text{A.3})$$

Where,

$$C_{bc} = -\frac{1}{V_b^i}\left(\frac{\partial V_b}{\partial P_c}\right)_{P_p} \qquad (\text{A.4})$$

$$C_{bp} = \frac{1}{V_b^i}\left(\frac{\partial V_b}{\partial P_p}\right)_{P_c} \qquad (\text{A.5})$$

$$C_{pc} = -\frac{1}{V_p^i}\left(\frac{\partial V_p}{\partial P_c}\right)_{P_p} \qquad (\text{A.6})$$

$$C_{pp} = \frac{1}{V_p^i}\left(\frac{\partial V_p}{\partial P_p}\right)_{P_c} \qquad (\text{A.7})$$

Where, the superscript *i* denotes the initial, unstressed state. Here, a decrease in volume is taken as a positive strain or compression is signed as positive.

Here, the applied pressures and their resulting strains will be incremental changes superimposed on an existing stress and strain. The loading state consisting of a uniform

stress of magnitude dP_c subjected to the entire outer surface of the porous rock and a uniform pressure of magnitude dP_p subjected to the interior pore surface, will be denoted as $\{dP_c, dP_p\}$.

If a stress increment $\{dP,dP\}$ that $dP_c = dP_p = dP$ is subjected to the surface of a body, the resulting incremental stress in the rock is a uniform stress of magnitude dP throughout matrix. This stress state leads to a uniform isotropic dilatation of magnitude:

$$d\varepsilon_m = dP/K_m = C_m dP \qquad (\text{A.8})$$

Where C_m and K_m are the matrix (rock solid) compressibility and bulk modulus.

This stress and strain within the matrix is exactly the same as that which would occur if the pores are filled up with matrix material and the boundary conditions on the outer surface are unchanged. In this latter case, the total bulk strain is equal to:

$$d\varepsilon_b = C_m dP \qquad (\text{A.9})$$

So, the bulk volume change is given by:

$$dV_b = -C_m V_b^i dP \qquad (\text{A.10})$$

Now consider $\{dP,0\}$, the stress increment which corresponds to a change only in the confining pressure. This will give rise to a change in the bulk volume given by:

$$dV_b = -C_{bc} V_b^i dP \qquad (\text{A.11})$$

While the stress increment $\{0,dP\}$ will give rise to a change in the bulk volume:

$$dV_b = C_{bp} V_b^i dP \qquad (\text{A.12})$$

For infinitesimal condition, the superposition principle can be considered as valid that the stress increment of $\{0,dP\}$ can be stated as the difference between $\{dP,dP\}$ and $\{dP,0\}$ as illustrated in Fig. 75. The strains resulting from the stress increment of $\{0,dP\}$ will be equal to the difference between the strains resulting from the stress increments $\{dP,dP\}$ and $\{dP,0\}$. Using the notation $dV_b(dP_c,dP_p)$ to refer to the bulk volume change resulting from the stress increment $\{dP_c,dP_p\}$ can be written as follows:

$$dV_b(0,dP) = dV_b(dP,dP) - dV_b(dP,0) \qquad (\text{A.13})$$

$$C_{bp} V_b^i dP = -C_m V_b^i dP + C_{bc} V_b^i dP \qquad (\text{A.14})$$

Therefore:

$$C_{bp} = C_{bc} - C_m \qquad (\text{A.15})$$

Similarly, it can be derived:

$$C_{pp} = C_{pc} - C_m \qquad (\text{A.16})$$

In terms of C_{bc}, C_m and ϕ^i:

$$C_{pp} = \frac{\left[C_{bc} - \left(1+\phi^i\right)C_m\right]}{\phi^i} \qquad (\text{A.17})$$

$$C_{pc} = \frac{(C_{bc} - C_m)}{\phi^i} \qquad (\text{A.18})$$

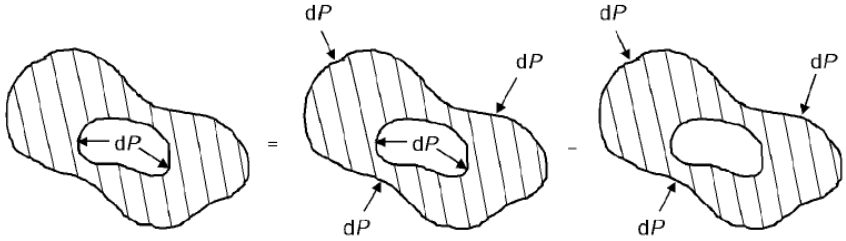

Fig. 75 - Illustration of the superposition concept. Reprinted from Jaeger et al. (2007).

The derivation of a linearized, non-hydrostatic poroelastic theory can be started from the stress strain relations of a nonporous material expressed in terms of the elastic shear modulus or rigidity (G) and Poisson ratio (v) (Jaeger et al., 2007):

$$\varepsilon_{xx} = \frac{1}{2G}\left[\sigma_{xx} - \frac{v}{(1+v)}\left(\sigma_{xx} + \sigma_{yy} + \sigma_{zz}\right)\right] \quad (\text{A.19})$$

$$\varepsilon_{yy} = \frac{1}{2G}\left[\sigma_{yy} - \frac{v}{(1+v)}\left(\sigma_{xx} + \sigma_{yy} + \sigma_{zz}\right)\right] \quad (\text{A.20})$$

$$\varepsilon_{zz} = \frac{1}{2G}\left[\sigma_{zz} - \frac{v}{(1+v)}\left(\sigma_{xx} + \sigma_{yy} + \sigma_{zz}\right)\right] \quad (\text{A.21})$$

$$\varepsilon_{xy} = \frac{\tau_{xy}}{2G} \quad (\text{A.22})$$

$$\varepsilon_{xz} = \frac{\tau_{xz}}{2G} \quad (\text{A.23})$$

$$\varepsilon_{yz} = \frac{\tau_{yz}}{2G} \quad (\text{A.24})$$

In matrix form:

$$\boldsymbol{\varepsilon} = \frac{\boldsymbol{\sigma}}{2G} - \frac{v}{2G(1+v)} tr(\boldsymbol{\sigma})\mathbf{I} \qquad (\text{A.25})$$

Here, it is assuming infinitesimal condition.

If the porous rock is macroscopically isotropic, a pore pressure increment will lead to equal extensions along each of three mutually orthogonal directions. Since the total bulk volumetric strain resulting from an applied pore pressure is $-C_{bp}P_p$ (Eq.A.2), the coefficient that relates each macroscopic longitudinal strain to the pore pressure is $-\frac{C_{bp}}{3}$. Therefore, a term $-\frac{C_{bp}P_p}{3}$ must be added to each longitudinal strain, resulting stress-strain relation as follows:

$$\boldsymbol{\varepsilon} = \frac{\boldsymbol{\sigma}}{2G} - \frac{v}{2G(1+v)} tr(\boldsymbol{\sigma})\mathbf{I} - \frac{C_{bp}}{3} P_p\mathbf{I} \qquad (\text{A.26})$$

Substituting C_{bp} (Eq. A.15) into the previous equation:

$$\boldsymbol{\varepsilon} = \frac{\boldsymbol{\sigma}}{2G} - \frac{v}{2G(1+v)} tr(\boldsymbol{\sigma})\mathbf{I} - \frac{C_{bc} - C_m}{3} P_p\mathbf{I} \qquad (\text{A.27})$$

Biot coefficient (α) is defined as:

$$\alpha = 1 - \frac{K_{bc}}{K_m} = 1 - \frac{K}{K_m} = 1 - \frac{C_m}{C_{bc}} = \frac{C_{bc} - C_m}{C_{bc}} \qquad (\text{A.28})$$

Substituting the Biot coefficient definition result:

$$\boldsymbol{\varepsilon} = \frac{\boldsymbol{\sigma}}{2G} - \frac{v}{2G(1+v)} tr(\boldsymbol{\sigma})\mathbf{I} - \frac{\alpha C_{bc}}{3} P_p\mathbf{I} \qquad (\text{A.29})$$

Since $C_{bc} = \frac{1}{K_{bc}} = \frac{1}{K}$ (where K is the macroscopic bulk modulus) then:

$$\boldsymbol{\varepsilon} = \frac{\boldsymbol{\sigma}}{2G} - \frac{v}{2G(1+v)} tr(\boldsymbol{\sigma})\mathbf{I} - \frac{\alpha}{3K} P_p \mathbf{I} \qquad (\text{A.30})$$

Taking the trace of both sides and rearrange:

$$tr(\boldsymbol{\varepsilon}) = \frac{(1-2v)}{2G(1+v)} tr(\boldsymbol{\sigma}) - \frac{\alpha}{K} P_p \qquad (\text{A.31})$$

It can be written as:

$$tr(\boldsymbol{\sigma}) = \frac{2G(1+v)}{(1-2v)} tr(\boldsymbol{\varepsilon}) + 3\alpha P_p \qquad (\text{A.32})$$

The elastic modulus of rigidity or shear modulus (G) is defined as:

$$2G(1+v) = 3K(1-2v) \qquad (\text{A.33})$$

Eq. A.30 can be written as follows:

$$\boldsymbol{\sigma} = 2G\boldsymbol{\varepsilon} + \frac{v}{(1+v)} tr(\boldsymbol{\sigma})\mathbf{I} + \frac{2G}{3K} \alpha P_p \mathbf{I} \qquad (\text{A.34})$$

Substitute Eq. A.32 into Eq. A.34 to get:

$$\boldsymbol{\sigma} = 2G\boldsymbol{\varepsilon} + \frac{2Gv}{(1-2v)} tr(\boldsymbol{\varepsilon})\mathbf{I} + \frac{3v}{(1+v)} \alpha P_p \mathbf{I} + \frac{2G}{3K} \alpha P_p \mathbf{I} \qquad (\text{A.35})$$

After substituting and rearranging, finally we get:

$$\boldsymbol{\sigma} = 2G\boldsymbol{\varepsilon} + \lambda tr(\boldsymbol{\varepsilon})\mathbf{I} + \frac{3v}{(1+v)} \alpha P_p \mathbf{I} + \frac{(1-2v)}{(1+v)} \alpha P_p \mathbf{I} \qquad (\text{A.36})$$

Here, λ is lame parameter, an elastic modulus, defined in term of the bulk modulus (K):

$$K = \lambda + \frac{2}{3}G \qquad (\text{A.37})$$

Rearrange, we get the poroelastic constitutive equation relating stress and strain, Hooke's law for porous medium, in term of the effective stress (Biot, 1941):

$$\boldsymbol{\sigma} - \alpha P_p \mathbf{I} = 2G\boldsymbol{\varepsilon} + \lambda tr(\boldsymbol{\varepsilon})\mathbf{I} \qquad (\text{A.38})$$

Where,

$$tr(\boldsymbol{\varepsilon}) = \varepsilon_{vol} = \varepsilon_b = \varepsilon_{xx} + \varepsilon_{yy} + \varepsilon_{zz} \qquad (\text{A.39})$$

Recall Eq. A.31:

$$tr(\boldsymbol{\varepsilon}) = \frac{(1-2v)}{2G(1+v)} tr(\boldsymbol{\sigma}) - \frac{\alpha}{K} P_p \qquad (\text{A.40})$$

$$tr(\boldsymbol{\sigma}) = 3\bar{\sigma} = \sigma_{xx} + \sigma_{yy} + \sigma_{zz} \qquad (\text{A.41})$$

Where,

$\bar{\sigma}$ is the mean normal stress, [Pa; psia]

After substituting:

$$tr(\boldsymbol{\varepsilon}) = \varepsilon_{vol} = \frac{(1-2v)}{3K(1-2v)} 3\bar{\sigma} - \frac{\alpha}{K} P_p \qquad (\text{A.42})$$

Finally, the poroelastic constitutive equation relating stress and strain, in term of normal mean stress and volumetric strain:

$$\bar{\sigma} - \alpha P_p = \left(\lambda + \frac{2}{3}G\right)\varepsilon_{vol} \qquad (\text{A.43})$$

For thermo-poroelastic medium, that a porous medium subject to changes in both temperature and stress, a temperature term is added to Eq. A.43 (Winterfeld and Wu, 2016), resulting:

$$\bar{\sigma} - \alpha P_p - 3\beta_t K(T - T_{ref}) = \left(\lambda + \frac{2}{3}G\right)\varepsilon_{vol} \qquad (\text{A.44})$$

Where K is the bulk modulus, β_t is the linear thermal expansion coefficient and T_{ref} is the reference temperature for a thermally unstrained state.

Eq. A.44 can be written as:

$$\sigma_{kk} - \left[\alpha P_p + 3\beta_t K\left(T - T_{ref}\right)\right] = 2G\varepsilon_{kk} + \lambda\left(\varepsilon_{xx} + \varepsilon_{yy} + \varepsilon_{zz}\right) \qquad (\text{A.45})$$

Where $k = x, y, z$.

A.2 Derivation of the governing geomechanical equation

The governing geomechanical equation adopted in this work is based on work by Fakcharoenphol et al, 2013. The derivation of the equation is described here.

Under static equilibrium conditions:

$$\nabla . \boldsymbol{\sigma} + \mathbf{F_b} = 0 \qquad (\text{A.46})$$

$\mathbf{F_b}$ is the body force vector and $\boldsymbol{\sigma}$ is a stress tensor.

Substituting Eq. A.45 into Eq. A.46 and using P instead of P_p yield:

$$\alpha\frac{\partial P}{\partial x}+3\beta_t K\frac{\partial T}{\partial x}+2\mathrm{G}\frac{\partial \varepsilon_{xx}}{\partial x}+2\mathrm{G}\frac{\partial \varepsilon_{yx}}{\partial y}+2\mathrm{G}\frac{\partial \varepsilon_{zx}}{\partial z}+\lambda\frac{\partial}{\partial x}\left(\varepsilon_{xx}+\varepsilon_{yy}+\varepsilon_{zz}\right)+F_x=0 \qquad (\text{A.47})$$

$$\alpha\frac{\partial P}{\partial y}+3\beta_t K\frac{\partial T}{\partial y}+2\mathrm{G}\frac{\partial \varepsilon_{yy}}{\partial y}+2\mathrm{G}\frac{\partial \varepsilon_{xy}}{\partial x}+2\mathrm{G}\frac{\partial \varepsilon_{zy}}{\partial z}+\lambda\frac{\partial}{\partial y}\left(\varepsilon_{xx}+\varepsilon_{yy}+\varepsilon_{zz}\right)+F_y=0 \qquad (\text{A.48})$$

$$\alpha\frac{\partial P}{\partial z}+3\beta_t K\frac{\partial T}{\partial z}+2\mathrm{G}\frac{\partial \varepsilon_{zz}}{\partial z}+2\mathrm{G}\frac{\partial \varepsilon_{xz}}{\partial x}+2\mathrm{G}\frac{\partial \varepsilon_{yz}}{\partial y}+\lambda\frac{\partial}{\partial z}\left(\varepsilon_{xx}+\varepsilon_{yy}+\varepsilon_{zz}\right)+F_z=0 \qquad (\text{A.49})$$

After rearranging, Eq. A.47, A.48 and A.49 in term of displacement vector can be written as:

$$\alpha\frac{\partial P}{\partial x}+3\beta_t K\frac{\partial T}{\partial x}+(G+\lambda)\left\{\frac{\partial^2 u_x}{\partial x^2}+\frac{\partial^2 u_y}{\partial y\partial x}+\frac{\partial^2 u_z}{\partial z\partial x}\right\}+G\left\{\frac{\partial^2 u_x}{\partial y^2}+\frac{\partial^2 u_x}{\partial x^2}+\frac{\partial^2 u_x}{\partial z^2}\right\}+F_x=0 \qquad (\text{A.50})$$

$$\alpha\frac{\partial P}{\partial y}+3\beta_t K\frac{\partial T}{\partial y}+(G+\lambda)\left\{\frac{\partial^2 u_y}{\partial y^2}+\frac{\partial^2 u_x}{\partial x\partial y}+\frac{\partial^2 u_z}{\partial z\partial y}\right\}+G\left\{\frac{\partial^2 u_y}{\partial x^2}+\frac{\partial^2 u_y}{\partial y^2}+\frac{\partial^2 u_y}{\partial z^2}\right\}+F_y=0 \qquad (\text{A.51})$$

$$\alpha\frac{\partial P}{\partial z}+3\beta_t K\frac{\partial T}{\partial z}+(G+\lambda)\left\{\frac{\partial^2 u_z}{\partial z^2}+\frac{\partial^2 u_x}{\partial z\partial x}+\frac{\partial^2 u_y}{\partial z\partial y}\right\}+G\left\{\frac{\partial^2 u_z}{\partial x^2}+\frac{\partial^2 u_z}{\partial y^2}+\frac{\partial^2 u_z}{\partial z^2}\right\}+F_z=0 \qquad (\text{A.52})$$

In condensed form Eq. A.50 to Eq. A.52 can be written as follows, which is the equilibrium equation:

$$\alpha\nabla P+3\beta_t K\nabla T+(G+\lambda)\nabla(\nabla.\mathbf{u})+G\nabla^2\mathbf{u}+\mathbf{F}=0 \qquad (\text{A.53})$$

Taking divergence of Eq. A.50 to Eq. A.52 resulting:

$$\alpha\frac{\partial^2 P}{\partial x^2}+3\beta_t K\frac{\partial^2 T}{\partial x^2}+(G+\lambda)\frac{\partial}{\partial x}\left\{\frac{\partial^2 u_x}{\partial x^2}+\frac{\partial^2 u_y}{\partial y\partial x}+\frac{\partial^2 u_z}{\partial z\partial x}\right\} + G\frac{\partial}{\partial x}\left\{\frac{\partial^2 u_x}{\partial y^2}+\frac{\partial^2 u_x}{\partial x^2}+\frac{\partial^2 u_x}{\partial z^2}\right\}+\frac{\partial F_x}{\partial x}=0 \quad (A.54)$$

$$\alpha\frac{\partial^2 P}{\partial y^2}+3\beta_t K\frac{\partial^2 T}{\partial y^2}+(G+\lambda)\frac{\partial}{\partial y}\left\{\frac{\partial^2 u_y}{\partial y^2}+\frac{\partial^2 u_x}{\partial x\partial y}+\frac{\partial^2 u_z}{\partial z\partial y}\right\} + G\frac{\partial}{\partial y}\left\{\frac{\partial^2 u_y}{\partial x^2}+\frac{\partial^2 u_y}{\partial y^2}+\frac{\partial^2 u_y}{\partial z^2}\right\}+\frac{\partial F_y}{\partial y}=0 \quad (A.55)$$

$$\alpha\frac{\partial^2 P}{\partial z^2}+3\beta_t K\frac{\partial^2 T}{\partial z^2}+(G+\lambda)\frac{\partial}{\partial z}\left\{\frac{\partial^2 u_z}{\partial z^2}+\frac{\partial^2 u_x}{\partial z\partial x}+\frac{\partial^2 u_y}{\partial z\partial y}\right\} + G\frac{\partial}{\partial z}\left\{\frac{\partial^2 u_z}{\partial x^2}+\frac{\partial^2 u_z}{\partial y^2}+\frac{\partial^2 u_z}{\partial z^2}\right\}+\frac{\partial F_z}{\partial z}=0 \quad (A.56)$$

Adding Eq. A.54 to Eq. A.56 and rearranging, resulting:

$$\begin{aligned}\alpha\left\{\frac{\partial^2 P}{\partial x^2}+\frac{\partial^2 P}{\partial y^2}+\frac{\partial^2 P}{\partial z^2}\right\}+3\beta_t K\left\{\frac{\partial^2 T}{\partial x^2}+\frac{\partial^2 T}{\partial y^2}+\frac{\partial^2 T}{\partial z^2}\right\}+\frac{\partial F_x}{\partial x}+\frac{\partial F_y}{\partial y}+\frac{\partial F_z}{\partial z}\\ +(G+\lambda)\frac{\partial^2}{\partial x^2}\left\{\frac{\partial u_x}{\partial x}+\frac{\partial u_y}{\partial y}+\frac{\partial u_z}{\partial z}\right\}+G\frac{\partial u_x}{\partial x}\left\{\frac{\partial^2}{\partial y^2}+\frac{\partial^2}{\partial x^2}+\frac{\partial^2}{\partial z^2}\right\}\\ +(G+\lambda)\frac{\partial^2}{\partial y^2}\left\{\frac{\partial u_x}{\partial x}+\frac{\partial u_y}{\partial y}+\frac{\partial u_z}{\partial z}\right\}+G\frac{\partial u_y}{\partial y}\left\{\frac{\partial^2}{\partial y^2}+\frac{\partial^2}{\partial x^2}+\frac{\partial^2}{\partial z^2}\right\}\\ +(G+\lambda)\frac{\partial^2}{\partial z^2}\left\{\frac{\partial u_x}{\partial x}+\frac{\partial u_y}{\partial y}+\frac{\partial u_z}{\partial z}\right\}+G\frac{\partial u_z}{\partial z}\left\{\frac{\partial^2}{\partial y^2}+\frac{\partial^2}{\partial x^2}+\frac{\partial^2}{\partial z^2}\right\}=0\end{aligned} \quad (A.57)$$

Which can be written as:

$$\alpha\nabla^2 P+3\beta_t K\nabla^2 T+(\lambda+2G)\nabla^2\{\nabla.\mathbf{u}\}+\nabla\cdot\mathbf{F}=0 \quad (A.58)$$

The divergence of the displacement vector is the volumetric strain:

$$\nabla.\mathbf{u} = \frac{\partial u_x}{\partial x} + \frac{\partial u_y}{\partial y} + \frac{\partial u_z}{\partial z} = \varepsilon_{xx} + \varepsilon_{yy} + \varepsilon_{zz} = \varepsilon_{vol} \qquad (\text{A.59})$$

Substituting the volumetric strain taken from Eq. A.44 into Eq. A.58 resulting:

$$\alpha\nabla^2 P + 3\beta_t K\nabla^2 T + (\lambda + 2G)\nabla^2 \left\{ \frac{\bar{\sigma} - \alpha P_p - 3\beta_t K(T - T_{ref})}{\left(\lambda + \frac{2}{3}G\right)} \right\} + \nabla \cdot \mathbf{F} = 0 \qquad (\text{A.60})$$

After substituting the elastic modulus relations and rearranging, we get the governing geomechanical equation:

$$\frac{3(1-v)}{1+v}\nabla^2\bar{\sigma} - \frac{2(1-2v)}{1+v}\{\alpha\nabla^2 P + 3\beta_t K\nabla^2 T\} + \nabla \cdot \mathbf{F} = 0 \qquad (\text{A.61})$$

For multiporosity:

$$\frac{3(1-v)}{1+v}\nabla^2\bar{\sigma} - \frac{2(1-2v)}{1+v}\left[\sum_j \{\alpha_j\nabla^2 P_j + 3\beta_t K\omega_j\nabla^2 T_j\}\right] + \nabla \cdot \mathbf{F} = 0 \qquad (\text{A.62})$$

Where subscript *j* refers to multi-porosity continua.